Alma Mater Studiorum
Università di Bologna

SCHOOL OF ENGINEERING AND
ARCHITECTURE
Forlí campus

Master's degree in
AEROSPACE ENGINEERING
class LM-20

GRADUATION THESIS
in Simulation and Modelling in Fluid Dynamics

NUMERICAL EXPERIMENTS ON TURBULENT ENTRAINMENT

Candidate
Gabriele Boga

Supervisor
Prof. Elisabetta De Angelis

Co-supervisor
Prof. Andrea Cimarelli

Academic Year 2018/2019

Abstract

The aim of this thesis work is the study of the turbulent entrainment phenomenon in jets through numerical experiments. More specifically, an attempt to study the effect of engulfment (large-scales ingestion of external fluid) and nibbling (outward growth caused by the small-scales fluctuations near the interface) mechanisms separately was made. The flow chosen for the numerical experiments is the temporal planar jet. The idea behind these experiments is to study the spreading and the mixing of a passive scalar under the effect of two modified velocity fields. The first is a large-scale velocity field obtained through a filtering operation, while the second is a small-scale velocity field obtained subtracting the large-scale velocity field from the total one and then adding the mean velocity field.

Initially, the post-processing of a spatially developing planar jet, performed by Doctor Andrea Fregni and Professor Andrea Cimarelli, has been carried out in order to analyse the main features of spatially evolving jets compared with the temporal ones. A co-flow and a passive scalar are present in this simulation. The Reynolds number is set to $Re = 3000$ and the Schmidt number is $Sc = 1$. After performing the post-processing of the abovementioned simulation, a benchmark DNS of a temporal planar jet with $Re = 3000$ and $Sc = 1$ has been performed in order to evaluate the main differences with respect to the spatially evolving jet. Once the settings were validated, the numerical experiments with large and small scale velocity fields to study entrainment have been performed. The filter used in all the experiments is the box filter. The results of two different filter lengths are presented, the first is

$\Delta = 1.5\lambda_{cl}$ and the second is $\Delta = 3\lambda_{cl}$. Since λ_{cl} is function of time, the two filter lengths are themselves varying in time. The results of the experiments were then compared with those of the unfiltered solution. The passive scalar spread approximatively the same amount under the effect of the large-scale velocity fields and under the effect of the unfiltered velocity. On the other hand, the small-scale fluctuations have been proved to be important in the mixing process.

Contents

List of Figures

List of Tables

Chapter 1

Introduction

Turbulent flows surround us in our everyday life. The buoyant plume rising from a lit cigarette, a volcanic plume or the smoke exiting from a chimney are examples of buoyancy and/or momentum driven turbulent flows. The abovementioned momentum/buoyancy driven flows spreads and mix with the external fluid through the entrainment process. This process is of great interest in many industrial applications. The control of fuel mixing in combustion chambers, the prediction of the transport of a contaminant or the exploitation of the exhausts in order to increase the aerodynamic performances of a race car, all require a deep understanding of the entrainment process.

The spreading of a turbulent jet feeds on two different contributes usually classified as engulfment and nibbling. The first is an inviscid mechanism that contribute to the jet growth through the large-scale ingestion of external fluid. The second one consists in a partially viscous process that leads to the outward growth of the interface caused by irregular small-scales eddy motions near it [1].The answer on how to discriminate between these two processes in order to understand which is dominant on the turbulent entrainment is still open. This thesis work is placed in this context and is an attempt to increase the current understanding of this phenomenon.

The whole study is conducted through Direct Numerical Simulations

(DNS). The choice of this approach is determined by the fact that, in this way, it is possible to perform experiments that would be otherwise impossible with an experimental approach. In fact, in simulations, it is possible to change the physics of the problem studied. The idea behind this thesis work is to separately study the effect of large and small scales structures on the entrainment process, trying to discriminate between engulfment and nibbling. This has been performed by studying the spreading and mixing of a passive scalar under the effect of two different velocity fields obtained through a filtering operation. The first modified velocity field is composed only of large scales, while the second one consists of the mean flow plus the small scales fluctuations. More details are available in Chapter 6.

The present work is organized as follows: after some hints on turbulence and on the numerical method used, the post-processing of a spatially developing planar jet DNS (Chapter 4), previously performed by Doctor Andrea Fregni and Professor Andrea Cimarelli, is carried out. The study of this simulation has allowed to evaluate the main differences between spatially evolving jets and temporal ones. Subsequently, in Chapter 5, a DNS of a temporal planar jet is presented and analysed. This flow typology has been chosen due to the lower computational cost required with respect to the spatially developing jet. This DNS has been used as a benchmark simulation to validate the settings used in the subsequent numerical experiments. Finally, in Chapter 6, the core of the present work is presented. In this chapter the numerical experiments are presented, and the passive scalar evolution is studied under the effect of large and small scales separately. The path that led to the choice of the filter lengths and of the final approach is briefly exposed in the Appendix A.

Chapter 2

Theoretical Background

2.1 Governing Equations

In this chapter, the governing equations and some other important concepts are presented.

Under the continuum hypothesis, for a Newtonian and incompressible fluid, the incompressible Navier-Stokes equations can be derived. This set of equations, including a continuity equation (scalar equation) and a momentum balance equation (vectorial equation), is reported below in its dimensionless form:

$$\frac{\partial u_i^*}{\partial x_i^*} = 0 \tag{2.1}$$

$$\frac{\partial u_i^*}{\partial t^*} + \frac{\partial u_i^* u_j^*}{\partial x_j^*} = -\frac{\partial p^*}{\partial x_i^*} + \frac{1}{Re}\frac{\partial^2 u_i^*}{\partial x_j^* \partial x_j^*} \tag{2.2}$$

The symbol * indicates dimensionless quantities. The term u_i^* indicates the component of the velocity in the x_i^* direction and p^* indicates the pressure. The term Re stands for the Reynolds number defined as:

$$Re = \frac{UL}{\upsilon} \tag{2.3}$$

Where U and L are respectively the characteristics velocity and length of the problem. The term υ stands for the kinematic viscosity.

In all the simulations presented in this work, a passive scalar is present. The governing equation of this additional quantity is reported below in its dimensionless form:

$$\frac{\partial \phi^*}{\partial t^*} + \frac{\partial \phi^* u_i^*}{\partial x_i^*} = \frac{1}{ReSc} \frac{\partial^2 \phi^*}{\partial x_i^* \partial x_i^*} \tag{2.4}$$

Where ϕ is the passive scalar and Sc is the Schmidt number, defined as the ratio between the viscous diffusion rate and the molecular one. The scalar is passive because it does not influence the material properties of the flow. The scalar ϕ can represent various physical properties. It can be a small excess in temperature sufficiently small that its effect on material properties is negligible. In this case, the analogous parameter to the Sc is the Prandtl number, Pr. Alternatively, ϕ can be the concentration of a trace species [2].

The scalar is a bounded variable, it can take only a bounded interval of values. In particular, the considered range of the scalar in this work is [01]. The value 1 corresponds to a 100% concentration of the scalar, while the value 0 corresponds to the absence of the scalar.

2.2 Turbulence

In a turbulent flow, the pressure and the velocity fields are characterized by chaotic changes. Turbulence is characterized by the following peculiarities:

- **Irregularity**
- **Increased diffusivity**
- **Dissipation**
- **Multi-scale-phenomenon**

Because of its irregularity and because of the presence of a wide range of scales, the use of statistical tools is necessary. In the following subsections, some hints of one-point and two-point statistics are reported.

2.2.1 One-Point Statistics

The simplest statistics that can be computed are the single point statistics. Among these the one-point, one-time joint Cumulative Distribution Function (CDF) of the velocity is defined as follows:

$$F\left(\mathbf{V};\mathbf{x},t\right)=P\left\{u_i\left(\mathbf{x},t\right)\leqslant V_i,\ i=1,2,3\right\} \tag{2.5}$$

The above expression is used to indicate the probability that the velocity component u_i is smaller or equal to the random variable V_i.

Subsequently, the joint Probability Density Function (PDF) is defined as:

$$f\left(\mathbf{V};\mathbf{x},t\right)=\frac{\partial^3 F\left(\mathbf{V};\mathbf{x},t\right)}{\partial V_1\partial V_2\partial V_3} \tag{2.6}$$

Once defined these two statistics, it is possible to define the mean velocity field:

$$\left\langle\mathbf{u}\left(\mathbf{x},t\right)\right\rangle=\mathbf{U}\left(\mathbf{x},t\right)=\iiint_{-\infty}^{+\infty}f\left(\mathbf{V};\mathbf{x},t\right)dV_1dV_2dV_3 \tag{2.7}$$

The fluctuating velocity field can be defined as:

$$\mathbf{u'}\left(\mathbf{x},t\right)=\mathbf{u}\left(\mathbf{x},t\right)-\mathbf{U}\left(\mathbf{x},t\right) \tag{2.8}$$

Analogously, the one-point and one-time covariance of the velocity is defined as $\left\langle u_i'\left(\mathbf{x},t\right)u_j'\left(\mathbf{x},t\right)\right\rangle$. The latter are also called Reynolds Stresses. These terms can be interpreted as stresses since they contribute to the momentum transfer through the fluctuating velocity field (differently from the viscous stresses that act at a molecular level).

The Reynolds stresses are the components of a second order tensor. The diagonal components of this tensor $\left\langle u_i'u_i'\right\rangle$ are normal stresses and the off-diagonal components are shear stresses. This tensor is symmetric by construction.

The turbulent kinetic energy $k\left(\mathbf{x},t\right)$ is defined as half of the trace of the Reynolds stress tensor:

$$k\left(\mathbf{x},t\right)=\frac{1}{2}\left\langle\mathbf{u'}\cdot\mathbf{u'}\right\rangle \tag{2.9}$$

It follows that the RMS velocity can be expressed as:

$$u_{RMS} = \sqrt{\frac{2k}{3}} \tag{2.10}$$

2.2.2 Two-Point Statistics

In order to obtain some information on the spatial structures present in a turbulent flow, the two-point and one-time autocovariance can be useful. This function, also called two-point correlation, is defined as:

$$R_{ij}\left(\mathbf{r}, \mathbf{x}, t\right) = \left\langle u_i'\left(\mathbf{x}, t\right) u_j'\left(\mathbf{x} + \mathbf{r}, t\right)\right\rangle \tag{2.11}$$

From this function, it is possible to obtain different integral lengthscales:

$$L_{ii}\left(\mathbf{x}, t\right) = \frac{1}{R_{ii}\left(0, \mathbf{x}, t\right)} \int_0^{+\infty} R_{ii}\left(e_i\mathbf{r}, \mathbf{x}, t\right) dr \tag{2.12}$$

Where e_i is the unit vector in the x_i -coordinate direction.

For homogeneous turbulence, the two-point correlation function $R_{ij}(\mathbf{r}, t)$ is independent of $\mathbf{x}$. In this case, by computing the Fourier transform of R_{ij}, the information contained in it are re-expressed in terms of the velocity spectrum tensor:

$$E_{u_i u_j}\left(\mathbf{k}, t\right) = \frac{1}{\left(2\pi\right)^3} \iiint_{-\infty}^{+\infty} e^{-i\mathbf{k}\cdot\mathbf{r}} R_{ij}\left(\mathbf{r}, t\right) d\mathbf{r} \tag{2.13}$$

Where k is the wavenumber defined as:

$$k_k = \frac{2\pi}{\lambda_k} \tag{2.14}$$

With λ_k representing the wavelength in the x_k-direction.

2.2.3 Energy Cascade and Kolmogorov Hypotheses

Turbulence can be considered as composed by eddies of different sizes l and different related velocities $u\left(l\right)$. The larger eddies are structures with size

l_0 comparable to the flow scale and with a velocity u_0 of the order of u_{RMS}, which is comparable with the characteristic velocity of the flow. In Richardsonś perspective, these large eddies break up transferring their kinetic energy to smaller eddies and so on. Through this mechanism, the energy cascade take place. This process goes on until the Reynolds number associated to the considered eddy is sufficiently small to keep its motion stable. At these lengthscales, viscosity plays an important role and dissipates the kinetic energy. In order to better understand the features of these different scales, the following Kolmogorov hypotheses (approximately stated) can help us:

– **Kolmogorov's hypothesis of local isotropy**: At sufficiently high Reynolds number,the small-scale turbulent motions ($l \ll l_0$) are statistically isotropic.

From this first hypothesis, it can be deduced that, in the process of the energy cascade, the directional information contained in the large anisotropic scales (depending on the type of flow and on the boundary conditions), are gradually lost.

– **Kolmogorov's first similarity hypothesis**: In every turbulent flow at sufficiently high Reynolds number, the statistics of the small-scale motions ($l \ll l_0$) have a universal form that is uniquely determined by υ and ε.

Where ε is the dissipation of turbulent kinetic energy and is defined as:

$$\varepsilon = \upsilon \langle \frac{\partial u_i'}{\partial x_k} \frac{\partial u_i'}{\partial x_k} \rangle \tag{2.15}$$

This range of scales is referred to as the universal equilibrium range. In this range the timescales $l/u(l)$ are small compared with l_0/u_0, so that the small eddies can adapt quickly to maintain a dynamic equilibrium with the energy transfer rate imposed by the large eddies. From υ and ε the Kolmogorov scales can be derived:

$$\eta = \left(\frac{\upsilon^3}{\varepsilon} \right)^{\frac{1}{4}} \tag{2.16}$$

$$u_\eta = (\varepsilon \upsilon)^{\frac{1}{4}} \tag{2.17}$$

$$\tau_\eta = \left(\frac{\upsilon}{\varepsilon}\right)^{\frac{1}{2}} \tag{2.18}$$

– **Kolmogorov's second similarity hypothesis**: In every turbulent flow at sufficiently high Reynolds number, the statistics of the motions of scale l in the range $l_0 \gg l \gg \eta$ have a universal form that is uniquely determined by ε and independent of υ.

In this third hypothesis, the concept of inertial subrange. In particular, a lengthscale l_{DI} can be defined so that the universal equilibrium range ($l \ll l_0$) is divided in two subranges: the inertial subrange ($l_0 \gg l > l_{DI}$) and the dissipation range ($l < l_{DI}$). In the inertial subrange, the inertial effects are predominant, and the viscous effects are negligible. On the other hand, in the dissipation range, the viscous effects are not negligible. In the latter range, dissipation takes place. The sketches presented in Figure 2.1. schematically represent the energy cascade mechanism through the various lengthscales.

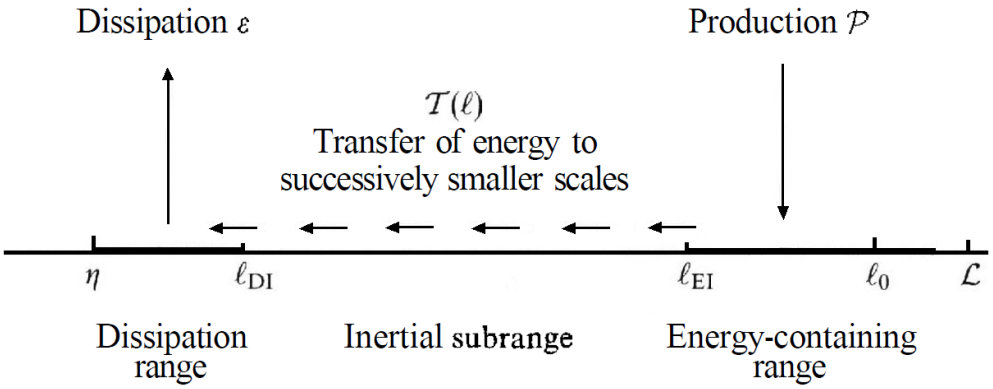

Figure 2.1: Energy cascade process

Another used lengthscale is the Taylor micro-scale. It falls in the inertial subrange and an approximation of its value can be computed as follows:

$$\lambda \simeq \left(\frac{10\upsilon k}{\varepsilon}\right)^{\frac{1}{2}} \tag{2.19}$$

From this quantity, the Taylor-scale Reynolds number can be defined:

$$Re_\lambda = \frac{u_{RMS}\lambda}{\upsilon} \tag{2.20}$$

2.3 Turbulent Jets

Turbulent jets are some of the most studied turbulent free shear flows [2] and are of great interest for a lot of applications. A jet is a free shear flow driven by momentum. The name f̈reeïndicates that these kinds of flows are remote from walls and turbulence arises because of mean-velocity differences. Different types of jet exist, like spatially developing round and planar jets, temporal round and planar jets, jets with a co-flow, jets with a crossflow, coaxial jets and many others. The present work is focused on spatially developing planar jet (Chapter 4) and temporal planar jets (Chapter 5 and 6).

2.3.1 Spatially Developing Planar Jets

The ideal spatially developing planar jet is statistically two-dimensional. The dominant direction of mean flow is x, the cross-stream coordinate is y and statistics are independent on the spanwise coordinate, z and on time. There is statistical symmetry about the plane $y = 0$. An instantaneous field of a spatially developing planar jet is shown in 2.2.

Because of the chaotic nature of this flow, it can be useful to reason in terms of mean quantities. The jet spreads going downstream and increase its mass flow rate by entraining quiescent fluid from the outside (2.3).

Some useful quantities are defined below.

The centreline velocity U_c, the half-width of the jet $y_{1/2}$ and the interface y_{int} are defined as:

$$U_c\left(x\right) = \left\langle u\left(x, 0, 0\right)\right\rangle \tag{2.21}$$

$$\frac{1}{2}U_c\left(x\right) = \left\langle u\left(x, y_{1/2}, 0\right)\right\rangle \tag{2.22}$$

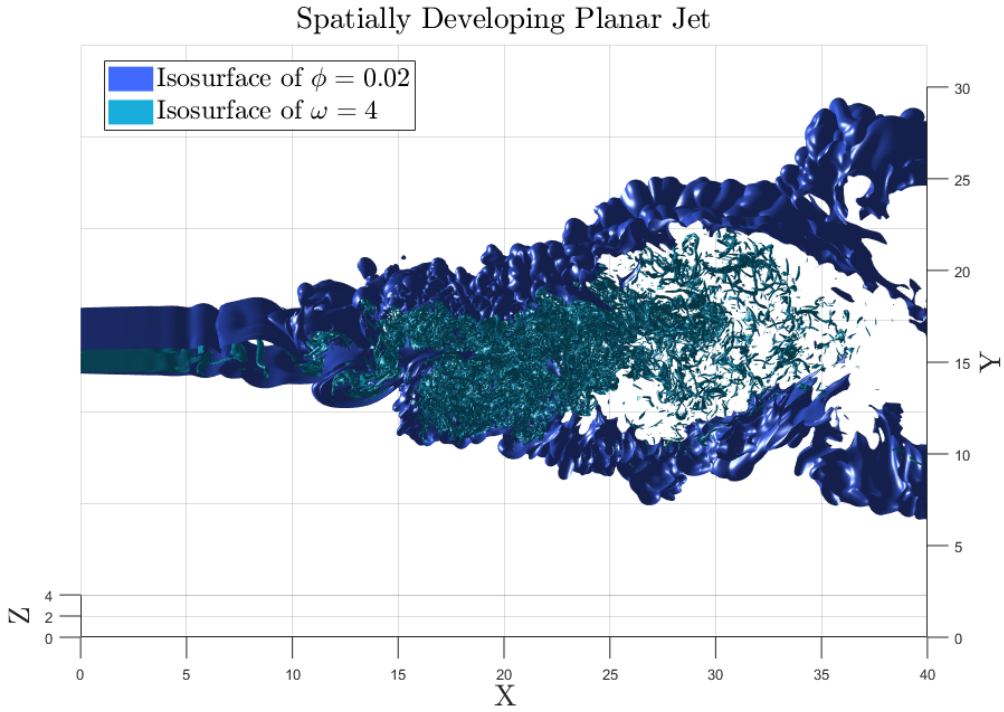

Figure 2.2: Spatially developying planar jet, isosurfaces of the vorticity module and of the scalar, present work (DNS from Doctor Andrea Fregni in collaboration with Professor Andrea Cimarelli)

$$0.02U_c\left(x\right) = \left\langle u\left(x, y_{int}, 0\right)\right\rangle \tag{2.23}$$

Analogously, in case of the presence of a scalar quantity ϕ:

$$\Phi_c\left(x\right) = \left\langle \phi\left(x, 0, 0\right)\right\rangle \tag{2.24}$$

$$\frac{1}{2}\Phi_c\left(x\right) = \left\langle \phi\left(x, y_{\phi\,1/2}, 0\right)\right\rangle \tag{2.25}$$

$$0.02\Phi_c\left(x\right) = \left\langle \phi\left(x, y_{\phi\,int}, 0\right)\right\rangle \tag{2.26}$$

In the first part of the jet, a core region can be identified. Immediately after this region, Kelvin-Helmholtz instability is developed, causing the roll-up of vortices that subsequently break up generating a turbulent flow.

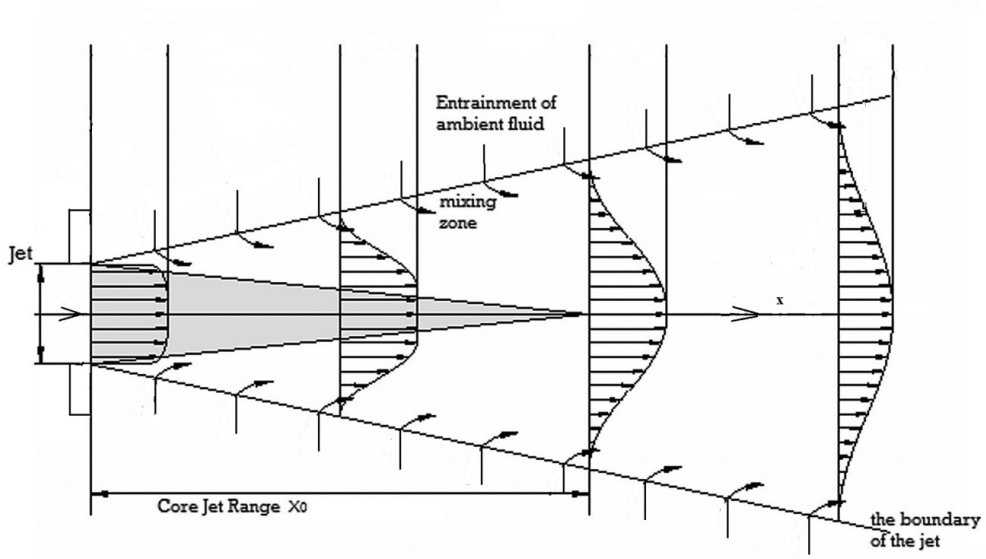

Figure 2.3: Entrainment mechanism

After the initial developing region, a self-similar condition is reached. The latter condition consists in the fact that, even if the mean velocity profiles change, their shape does not. After the initial developing region, the profiles of $U/U_c\,(x)$ plotted against $y/y_{1/2}\,(x)$ collapse onto a single curve. The variation of $y_{1/2}\,(x)$ is found to be linear (with a rate of spreading $S = \frac{dy_{1/2}}{dx} \approx 0.10$, [2]) and $U_c\,(x)$ is found to vary as $x^{-1/2}$ (the same holds for the scalar quantity). Other quantities show a self-similar behaviour, for examples, the mean crossflow velocity $V/U_c\,(x)$ (that presents a mean velocity directed outward in the central region, due the slowing down of $U_c\,(x)$ and directed inward in the external part due to the entrainment of external fluid), the Reynolds stresses $\frac{\langle u_i' u_i' \rangle}{U_c^2(x)}$ and $\frac{\langle u' v' \rangle}{U_c^2(x)}$, the mean scalar $\frac{\Phi}{\Phi_c(x)}$ and the scalar variance $\frac{\langle \phi' \phi' \rangle}{\Phi_c^2(x)}$.

2.3.2 Temporal Planar Jets

Differently from spatially developing jets, temporal jets develop in time and are statistically homogeneous in the streamwise direction, x and in the spanwise coordinate, z. This kind of flow presents a statistical symmetry about the plane $y = 0$ as the spatially developing jet. In Figure 2.4, a sketch

comparing the two kind on jets is shown.

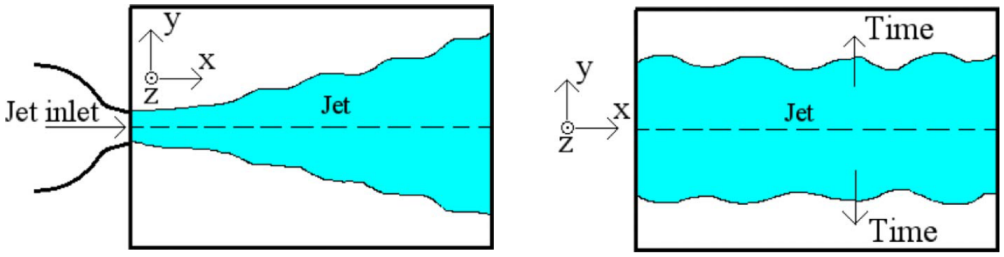

(a) (b)

Figure 2.4: (a) Sketch of a spatially developying jet, (b) sketch of a temporal jet, taken from [3]

An instantaneous field of a temporal planar jet is shown in Figure 2.5.

The previous general considerations on self-similarity and on the development are valid with the difference that the development progresses in time instead of the streamwise direction. Furthermore, the mean crossflow velocity is zero due to the homogeneity in the x direction. The quantities $y_{1/2}(t)$, $y_{int}(t)$, $y_{\phi\,1/2}(t)$ and $y_{\phi\,int}(t)$ are found to be proportional to $t^{1/2}$, while $U_c(t)$ and $\Phi_c(t)$ vary in time as $t^{-1/2}$.

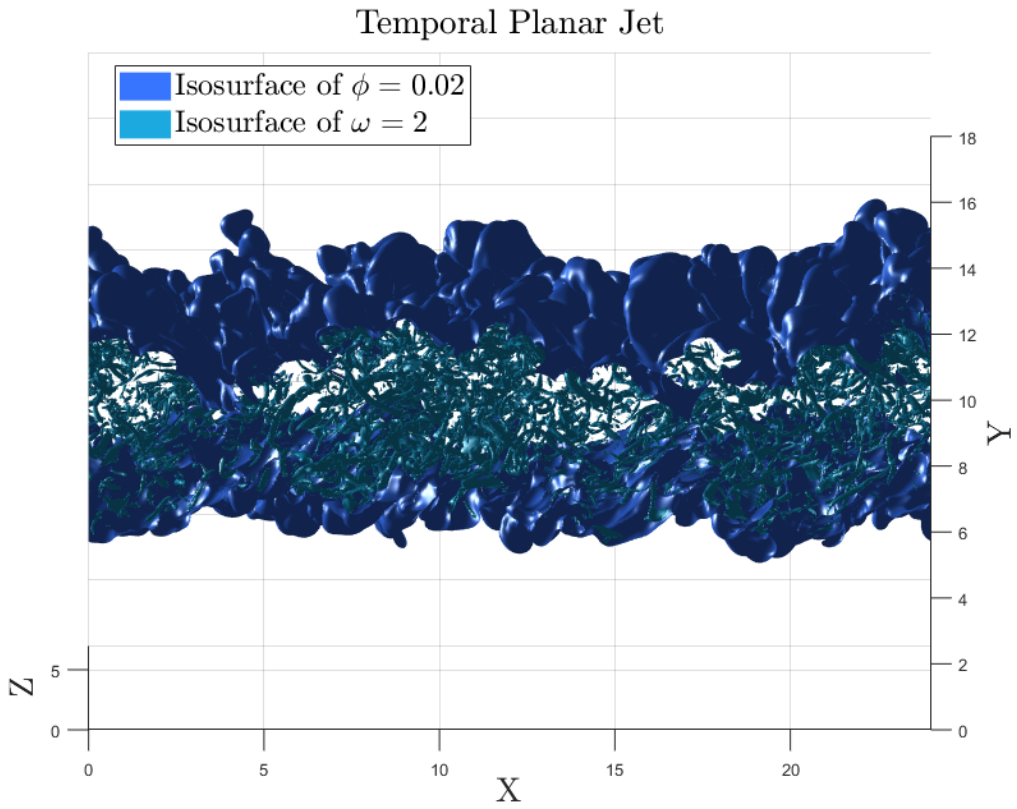

Figure 2.5: Temporal planar jet, isosurfaces of the vorticity module and of the scalar, present work

2.3.3 Entrainment

The mechanism through which the jets spread and mix with the external fluid is called entrainment. In order to better understand this process, some definitions and concepts are given below.

Firstly, the interface layer is defined as a thin region with a finite thickness δ that separates either turbulent and (external) irrotational flow regions, or, more in general, regions of different turbulent intensity. As the turbulent flow evolves, the average position of the interface moves outward with a boundary velocity E_b. In some flows, there is also a significant entrainment velocity $E_v\,(=-V)$ toward the interface. The boundary and entrainment velocities are linked through the critical process that occur at the interface. The out-

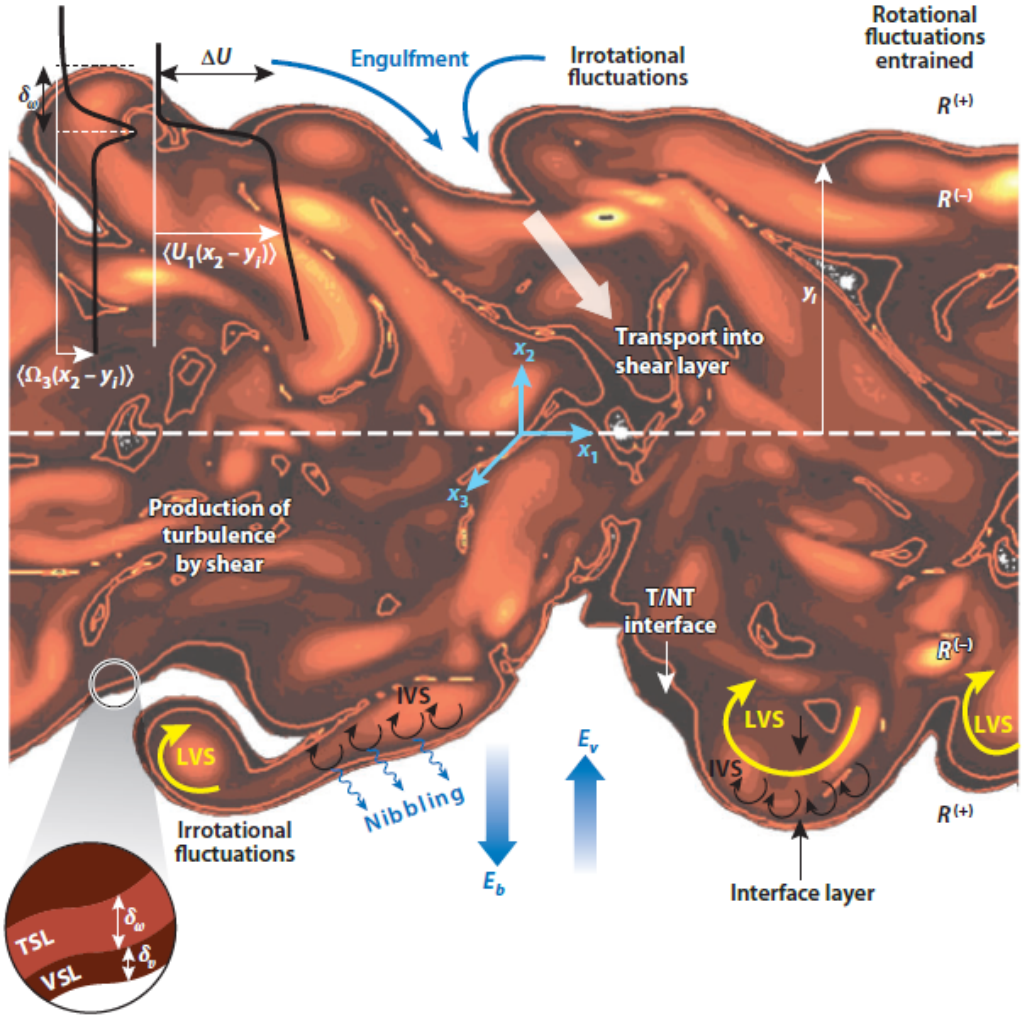

Figure 2.6: Schematic showing the several regions, length scales, and main physical processes that take place inside a free shear layer. Included are intense vorticity structures (IVS; worms, red); large-scale vortices (LVS; yellow); the thickness of the viscous superlayer, δv; and the thickness of the turbulent sublayer (or vorticity interface),$\delta\omega$. The turbulent/nonturbulent (T/NT) interface with coordinate Y_i(direction inwards and normal to the layer) is defined by the line separating these two sublayers. E_b is the outward velocity of the interfacial layer, and E_v is the mean velocity of the flow in the direction of the layer. ΔU is the velocity jump near the T/NT interface. Events of engulfing and nibbling are also represented. This figure is taken from [1]

ward movement of the interface is generally classified using the analogies of engulfment and nibbling, with engulfment referring to the inviscid component of the outward growth, caused large-scale ingestion of external fluid, and nibbling referring to a partially viscous process that leads to the outward growth of the interface caused by irregular small-scale eddy motions near it.

Fluid elements outside the interface, which are initially irrotational, may acquire vorticity in one of two ways (Figure 2.6): either locally at selected zones, in which there are large-scale fluctuations of the interface with negative curvature pointing inward (engulfment), or along the entire interface by a viscous diffusion process (nibbling). Which mechanism dominates is the subject of some debate. Part of the challenge in answering this still open question is how to objectively discriminate between the engulfment and nibbling mechanism [1].

In the lower left part of Figure 2.6, the interface layer is schematically shown, and it consists of two adjacent layers bridging the irrotational and turbulent regions. The first layer is the viscous superlayer (VSL) with thickness δ_υ. This layer exists because the only way an initially irrotational fluid element can acquire vorticity is by diffusion [4]. The second one is the turbulent sublayer (TSL) with thickness δ_ω. In this layer, the vorticity magnitude is subject to a rapid growth and it links the vorticity level in the VSL to the vorticity level in the turbulent region.

The VSL controls the process by which vorticity diffuses from the turbulent region to the irrotational one. This process is therefore controlled by υ. The associated length-scale is η [5, 6, 7, 8]. In contrast, the thickness of the turbulent sublayer δ_ω is comparable to the Taylor micro-scale λ.

In the case of a turbulent jet with a passive scalar with Schmidt $Sc = 0.7$, the thickness of the scalar variation across the layer δ_ϕ is of the order of λ [9].

Chapter 3

Numerical Method

All the following simulations have been performed using the Incompact3d free source software. This software is based on a Cartesian mesh. The use of this simple mesh offers the opportunity to implement high-order schemes for the spatial discretization [10]. The main originality of the solver is that the Poisson equation (to ensure incompressibility) is fully solved in the spectral space. The pressure mesh is staggered from the velocity one by half a mesh to avoid spurious pressure oscillations. The pressure projection method is used to solve the incompressible Navier-Stokes equations. The organization of the time loop (contained in the main file) is shown in Figure 3.1.

The software offers the possibility to set 3 different boundary conditions: periodic, Neumann and Dirichlet. A non-uniform grid-point spacing can be used in one direction. A passive scalar can be added to the simulation.

The skew-symmetric formulation has been used in this work for the convective terms of the Navier-Stokes equation:

$$H_i = \frac{1}{2}\left(\frac{\partial u_i u_j}{\partial x_j} + u_j \frac{\partial u_i}{\partial x_j}\right) \tag{3.1}$$

This formulation is recommended for a better modelisation of the small scales and less aliasing [10].

The spatial derivatives are approximated in the following way (compact

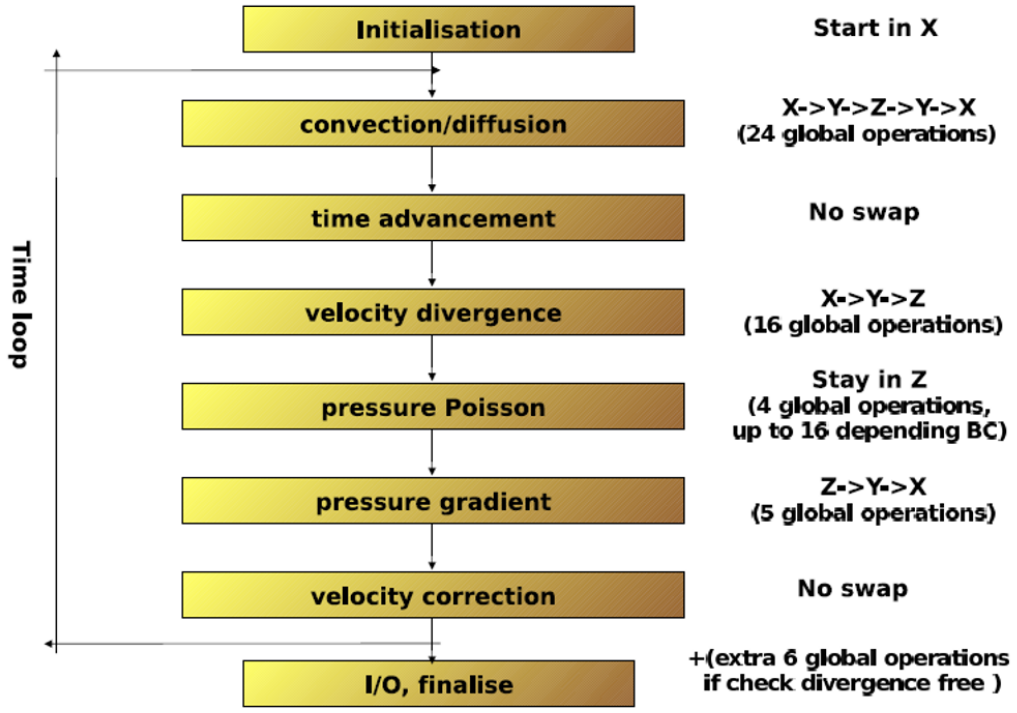

Figure 3.1: Structure of Incompact3d

finite differences sixth-order accurate):

$$\alpha f'_{i-1} + f'_i + \alpha f'_{i+1} = a\frac{f_{i+1} - f_{i-1}}{2\Delta x} + b\frac{f_{i+2} - f_{i-2}}{4\Delta x} \tag{3.2}$$

$$\alpha f''_{i-1} + f''_i + \alpha f''_{i+1} = a\frac{f_{i+1} - 2f_i + f_{i-1}}{\Delta x^2} + b\frac{f_{i+2} - 2f_i + f_{i-2}}{4\Delta x^2} + c\frac{f_{i+3} - 2f_i + f_{i-3}}{9\Delta x^2} \tag{3.3}$$

Choosing $\alpha = 2/11$, $a = 12/11$, $b = 3/11$ and $c = 0$, this scheme is sixth-order accurate [11].

The previous relations can be written in a matrix formulation as follows:

$$A_x f' = \frac{1}{\Delta x} B_x f \tag{3.4}$$

$$A'_x f'' = \frac{1}{\Delta x^2} B'_x f \tag{3.5}$$

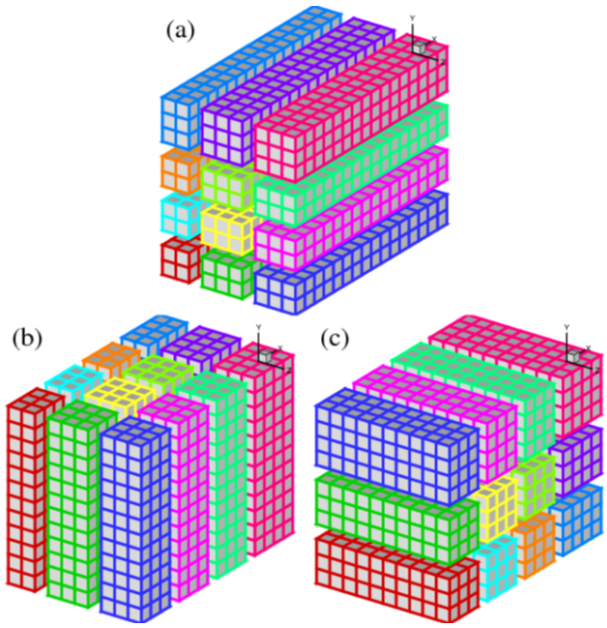

Figure 3.2: 2D domain decomposition using a 4 by 3 processor grid

Incompact3d offers the possibility to use different methods for the time advancement. In particular, Runge-Kutta 3 and 4 and Adam-Bashforth 2 and 3. The RK3 method is used in all the simulations presented in this thesis.

Incompact3d offers the possibility to split the simulation on parallel computational cores in order to minimize the computational time. The domain is divided as many times as many processors are used. In particular, a 2D decomposition is possible by dividing the domain as shown in Figure 3.2 [12].

The three different subdivisions are respectively representing decompositions in x-pencils, y-pencils and z-pencils. The transformation that allows to go from one to another is called transposition. Transpositions are necessary because the derivation can be performed only in the direction in which the domain portions are aligned. For example, before deriving in the z direction it is necessary to express the involved variable in z-pencils.

Chapter 4

Spatially Developing Planar Jet

The present simulation of a spatially developing planar jet has been previously carried out by Doctor Andrea Fregni in collaboration with Professor Andrea Cimarelli. The aim of this work regarding this simulation is to evaluate the main differences between this kind of flow and the temporal jet chosen for the numerical experiments presented in Chapter 6.

The simulation presents a coflow. The Reynolds number is set to $Re = 3000$. A passive scalar with a Schmidt number $Sc = 1$ is used in the simulation.

4.1 DNS Settings

4.1.1 Domain

The computational domain on which the simulation has been performed is characterized by dimensions $40h \times 30h \times 4h$ ($L_x \times L_y \times L_z$). Where h is set to be 1, in dimensionless units. The simulation has been performed at CINECA on 1088 physical processors. The domain has been decomposed with a 2D decomposition of dimensions 32×34 processors in order to make the parallelization possible.

4.1.2 Mesh and Time-step

The mesh used is a Cartesian and uniform one. The spatial discretization of the domain is defined by $(N_x \times N_y \times N_z)$ $1025 \times 768 \times 128$ points, resulting in 100761600 elements. The obtained grid spacings are: $\Delta x \approx \Delta y \approx 0.039$ and $\Delta z \approx 0.031$.

The time-step selected is 0.001 time units resulting in a Courant number of 0.03. Runge-Kutta 3 method has been used for the advancement in time.

4.1.3 Boundary Conditions and Initial Condition

In y (cross-stream) and z (spanwise) directions, periodic boundary conditions are used. By imposing a periodic boundary condition in the cross-stream direction, the confinement effect on the jet is reduced (with respect to the impermeability boundary condition). In the x (streamwise) direction, an inflow and an outflow are used. As inflow condition (Dirichlet boundary condition), the velocity profile in inlet is defined as:

$$u\left(x=0,y,z,t\right)=\frac{U_1+U_2}{2}+\frac{U_1+U_2}{2}\left(\tanh\left(15\left(0.5-\mid y\mid\right)\right)\right)\cdot\left(1+noise\right) \tag{4.1}$$

Where U_1 is the velocity in the core of the jet (set to 1.09) and U_2 is the velocity of the coflow (set to 0.09), resulting in a difference in velocity $\Delta U_0 = 1$. With this choice of velocities, the co-flow is small if compared to the velocity difference, in fact $\frac{U_2}{\Delta U_0} = 0.09$. The Reynolds number is defined as $Re = \frac{\Delta U_0 h}{\upsilon} = 3000$.

A white noise with zero mean and amplitude 0.06 velocity units is introduced in the inflow condition as shown in the formula. The noise has been introduced in order to anticipate the transition to turbulence. The resulting averaged inflow condition is shown in Figure 4.1. The other velocity components are set to zero.

The inflow condition used for the passive scalar is:

$$\phi\left(x=0,y,z,t\right)=\frac{\Phi_1+\Phi_2}{2}+\frac{\Phi_1+\Phi_2}{2}\left(\tanh\left(15\left(0.5-\mid y\mid\right)\right)\right) \tag{4.2}$$

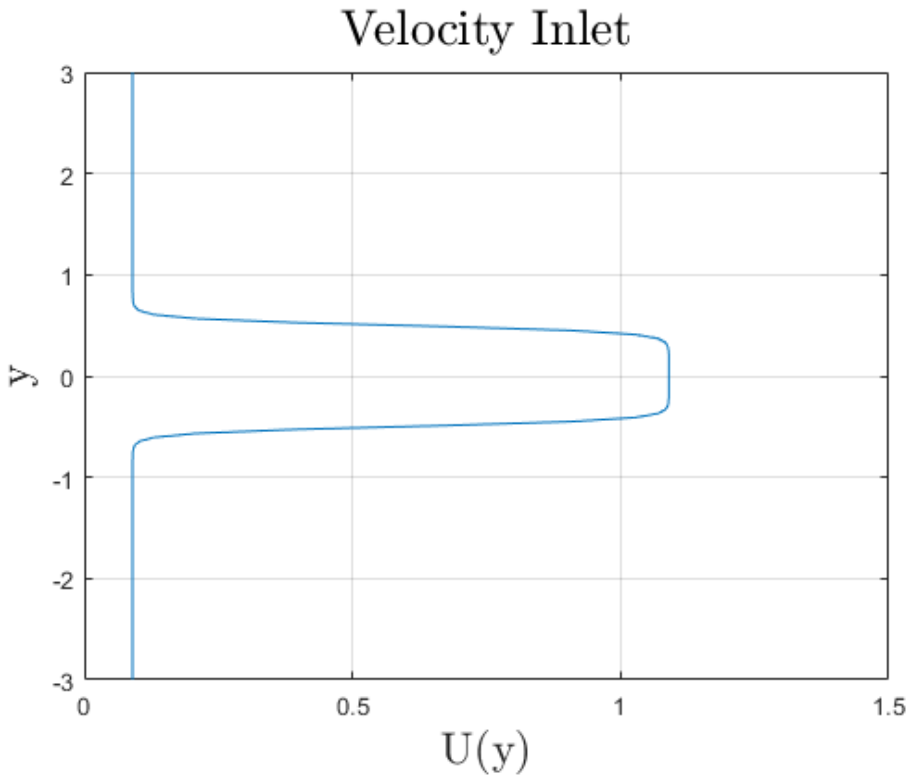

Figure 4.1: Velocity inlet of the spatially developying jet, present DNS

Where Φ_1 is set to 1 and Φ_2 is set to 0.

A convection equation has been used to set the outflow boundary condition for the velocity and for the passive scalar:

$$\frac{\partial u_i}{\partial t} + c_x \frac{\partial u_i}{\partial x} = 0 \tag{4.3}$$

$$\frac{\partial \phi}{\partial t} + c_x \frac{\partial \phi}{\partial x} = 0 \tag{4.4}$$

In particular, the term c_x is the median value of the velocity computed in the y-z plane at the x coordinate $N_x - 1$ at the timestep n. Solving this simple convection equation, it is possible to find the value of the three velocity components and of the scalar at the outlet to be used as boundary

condition at the timestep $n+1$. The initial condition used is:

$$u\left(x,y,z,t=0\right)=\frac{U_1+U_2}{2}+\frac{U_1+U_2}{2}\left(\tanh\left(15\left(0.5-\mid y\mid\right)\right)\right)\cdot\left(1+noise\right) \tag{4.5}$$

Where all the parameters used are the same as those used in the inflow condition.

Analogously, for the scalar, the initial condition used is:

$$\phi\left(x,y,z,t=0\right)=\frac{\Phi_1+\Phi_2}{2}+\frac{\Phi_1+\Phi_2}{2}\left(\tanh\left(15\left(0.5-\mid y\mid\right)\right)\right) \tag{4.6}$$

Again, all the parameters used are the same as those used in the inflow condition.

4.1.4 Statistical Symmetries

Once the flow has reached the statistical convergence, some statistical symmetries hold. In particular, this type of flow is statistically homogeneous in the z direction (spanwise) and in time. Furthermore, the flow presents a symmetry in the y direction (crossflow) around the midplane. For these reasons, the mean values have been calculated by averaging in the z direction, in time and between specular values around the x-z midplane.

In order to find the time unit at which the fully developed state is reached, the mean values of the scalar and of the three velocity components squared have been monitored (averaged over the volume). Their trends are reported in Figure 4.2. The values corresponding to the first 100 time units where not reported for availability of storage space reasons.

From the graphs above it can be seen that the statistical convergence already holds from time unit 100. Consequently, all the averaging operations have been computed only from time unit 100 on.

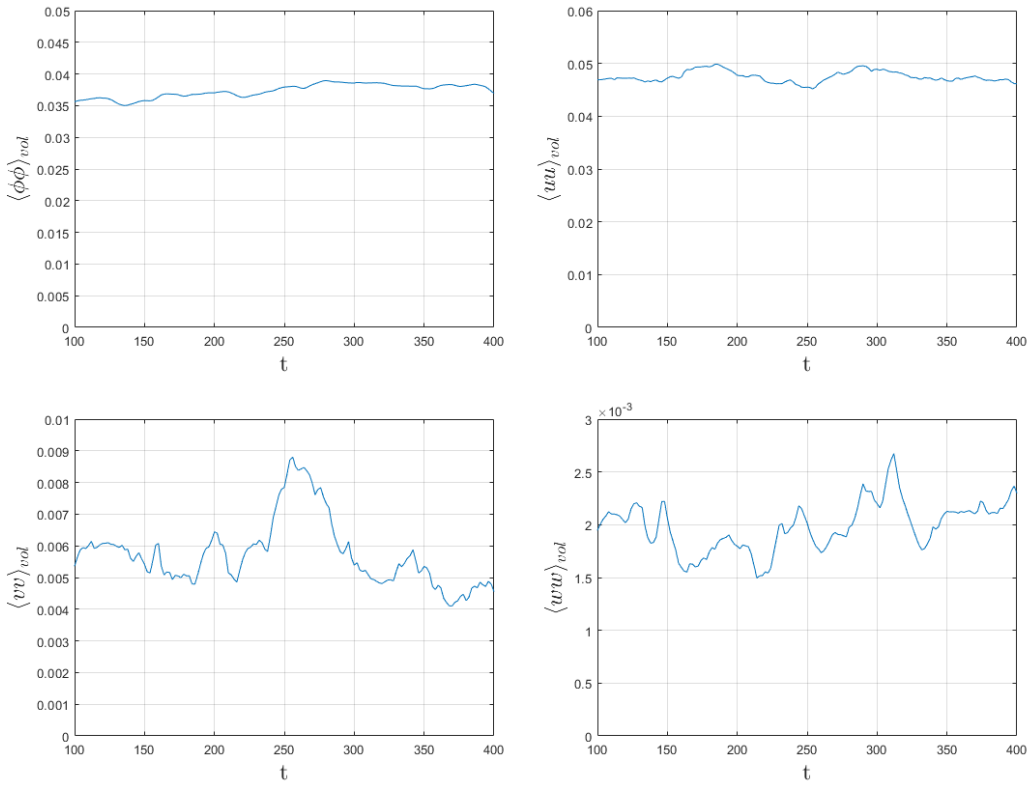

Figure 4.2: Convergence criteria

4.2 Flow Topology

As a first step, the contours of the velocity components, of the passive scalar and of the vorticity at different time units have been analysed. In Figure 4.3, the contours corresponding to time unit 200 and z coordinate corresponding to unit length 2 (x-y midplane) are shown.

From the contours of the x velocity component, it can be noticed that the initial co-flow is not constant along the x direction, but that it is slowing down. Since a periodic boundary condition is used in the y and z directions, the total flow rate along x must remain constant. In fact, with this kind of boundary conditions, the fluid exiting from one boundary of the domain must re-enter from the opposite boundary and vice versa, resulting in a conservation of the total flow rate. On the other hand, the flow rate of the jet is

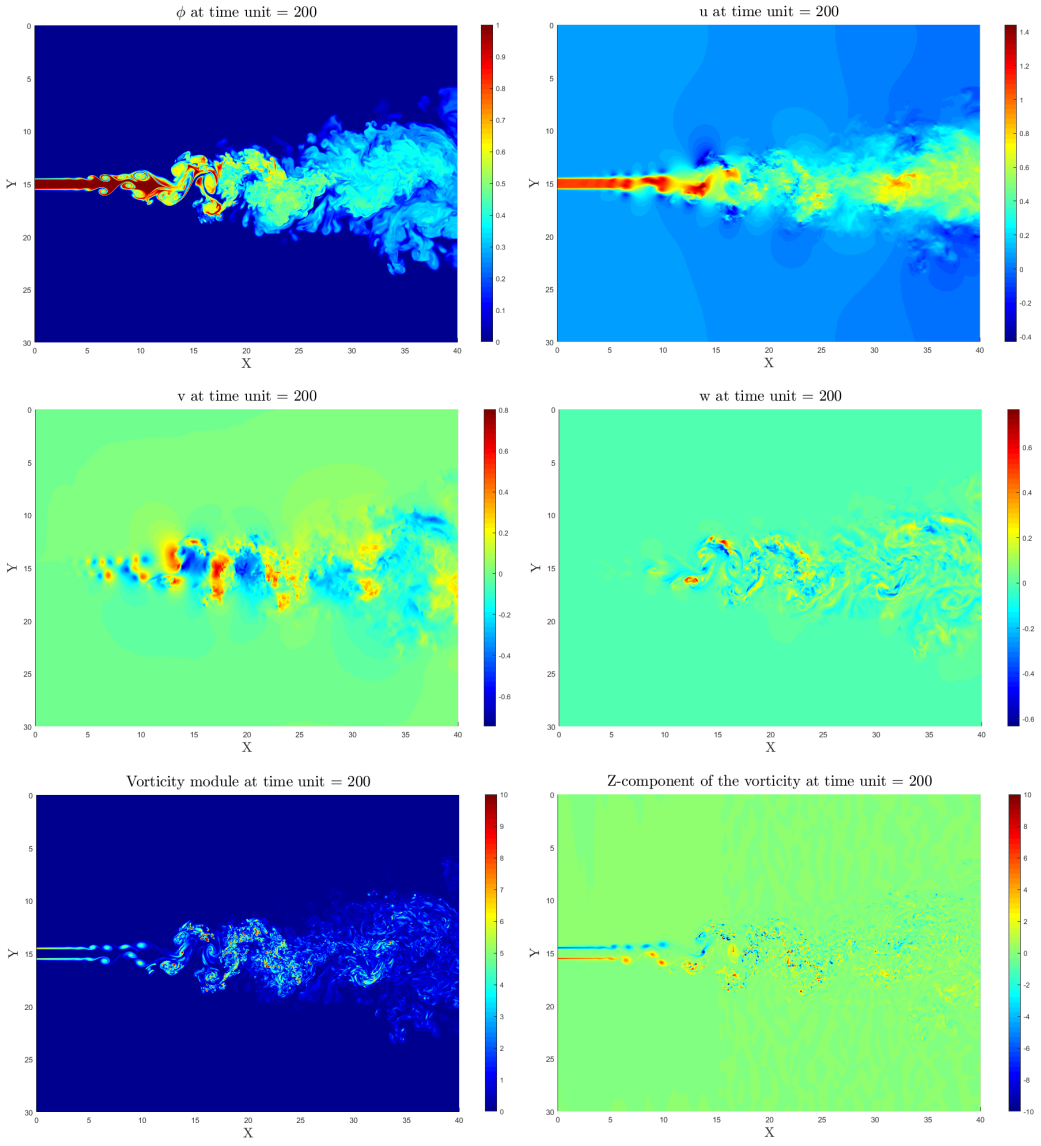

Figure 4.3: Instantaneous contours: passive scalar (top left); streamwise velocity component (top right); cross-stream velocity component (middle left); spanwise velocity component (middle right); vorticity module (bottom left); spanwise component of the vorticity (bottom right)

increasing in the x direction because of the entrainment process. Considering these two facts, the local co-flow must decrease in the x direction in order to satisfy the overall flow rate balance. From the contours of the scalar, it

can be noticed an initial generation of vortices of the Kelvin-Helmholtz type followed by the generation of turbulence that starts decaying downstream. From the contours of the y component of the velocity it can be recognized a pattern in the initial part of alternating crossflow velocities. This is due to the presence of vortices inducing opposed crossflow velocities. These structures are also visible in the vorticity contours.

4.3 Mean Profiles and Self-Similarity

In the following subsection, some statistics are shown and commented. In Figure 4.4 and 4.5 the mean profiles are shown.

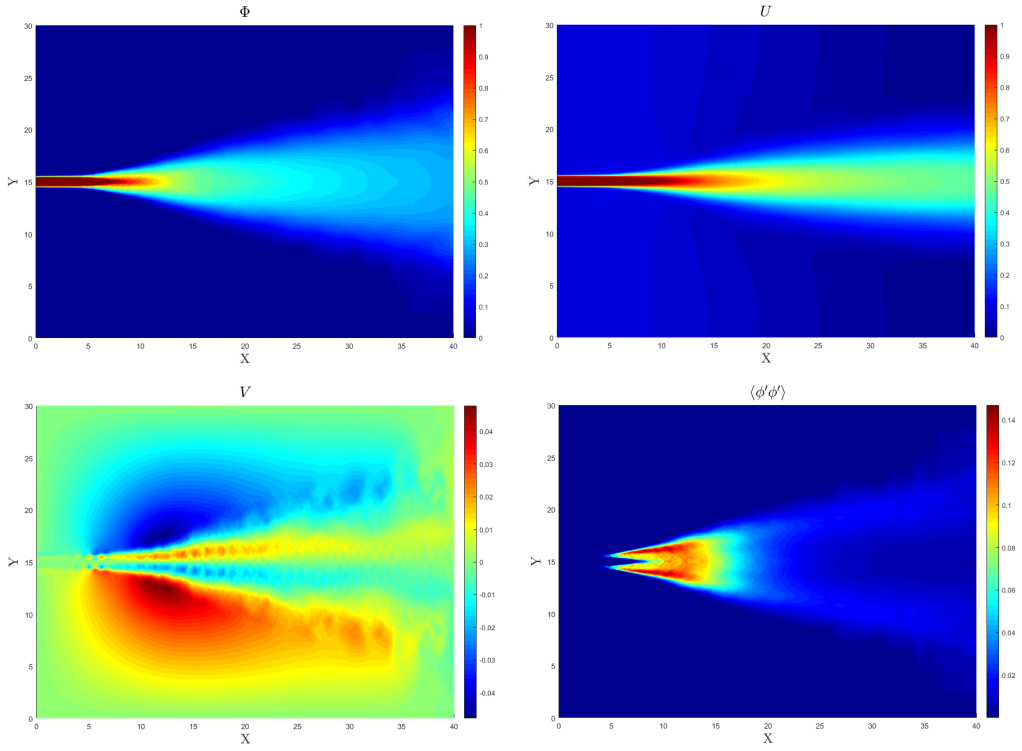

Figure 4.4: Mean profiles: passive scalar (top left); streamwise velocity component (top right); cross-stream velocity component (bottom left); scalar variance (bottom right)

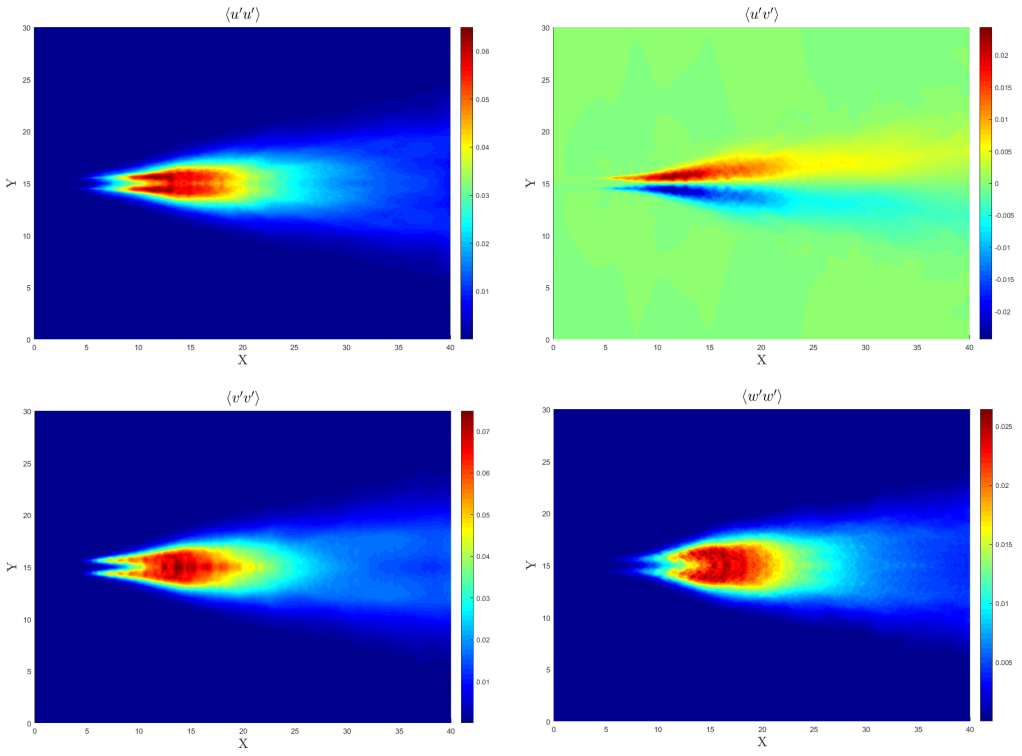

Figure 4.5: Mean profiles: streamwise velocity component variance (top left); u and v covariance (top right); cross-stream velocity component variance (bottom left); spanwise velocity component variance (bottom right)

From the contours of the mean scalar field and of the streamwise component of the velocity the spreading of jet is evident. The countours reported in Figure 4.4 and 4.5 have been obtained by averaging in the z direction, in time and also exploiting the symmetry with respect to the x-z midplane.

From the contours of the y component of the velocity, near the centreline it can be noticed that the mean crossflow velocity is directed outward the core of the jet. This is due to the fact that the mean streamwise component at the centreline is slowing down in the x direction, so in order to satisfy the continuity equation, a flow directed outside is necessary (since the mean velocity in the z direction is zero). On the other hand, the mean y component of the velocity outside the core of the jet is directed inward the jet core. This velocity component is caused by the fact that the jet is entraining fluid from

outside its core. This increase of flow rate in the x direction implies a mean crossflow velocity directed inward.

Looking at the variances of the velocity components and of the scalar, it can be seen that turbulence is generated approximately from unit length 5 and starts decaying between unit length 10 and 15.

In order to identify the self-similarity region, some parameters have been studied. In particular, the trends of some quantities, like U_c, Φ_c, $y_{1/2}$, $y_{\phi\,1/2}$ and others, have been scaled in order to obtain a linear behaviour in the self-similar region (accordingly with the theory). These quantities are shown in Figure 4.6 and 4.7.

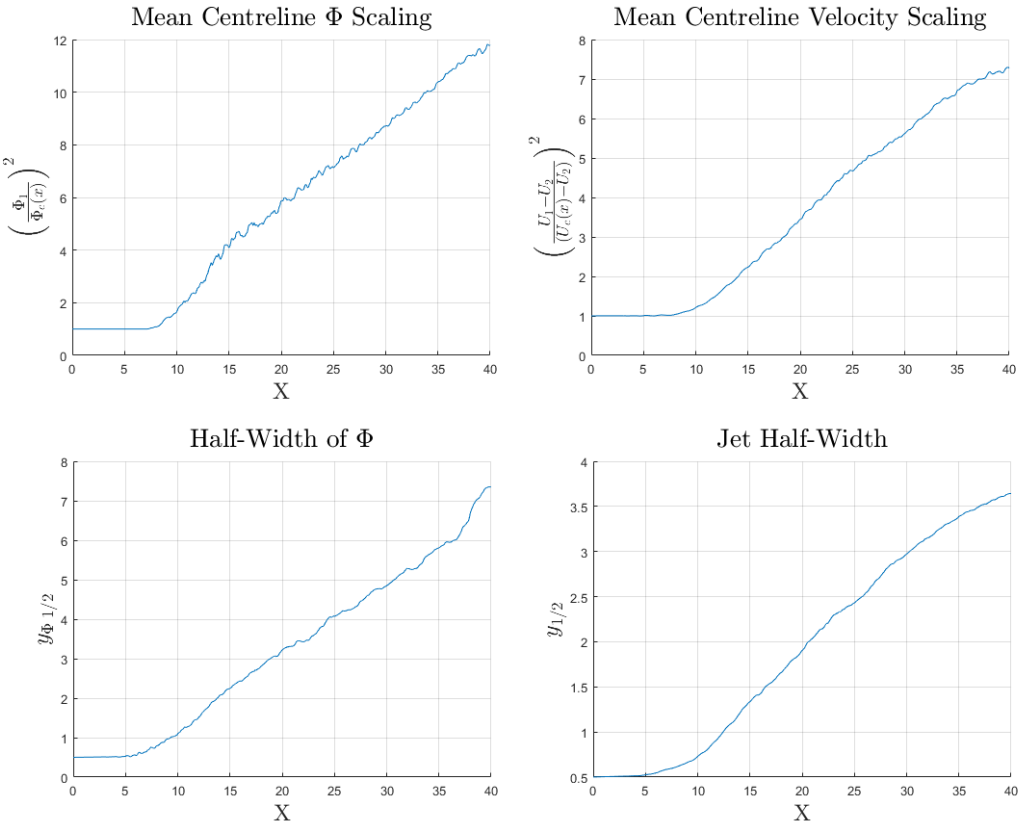

Figure 4.6: Evolution of the mean scalar at the centreline (top left); evolution of the mean velocity at the centreline (top right); evolution of the jet scalar half-width (bottom left); evolution of the jet half-width (bottom right)

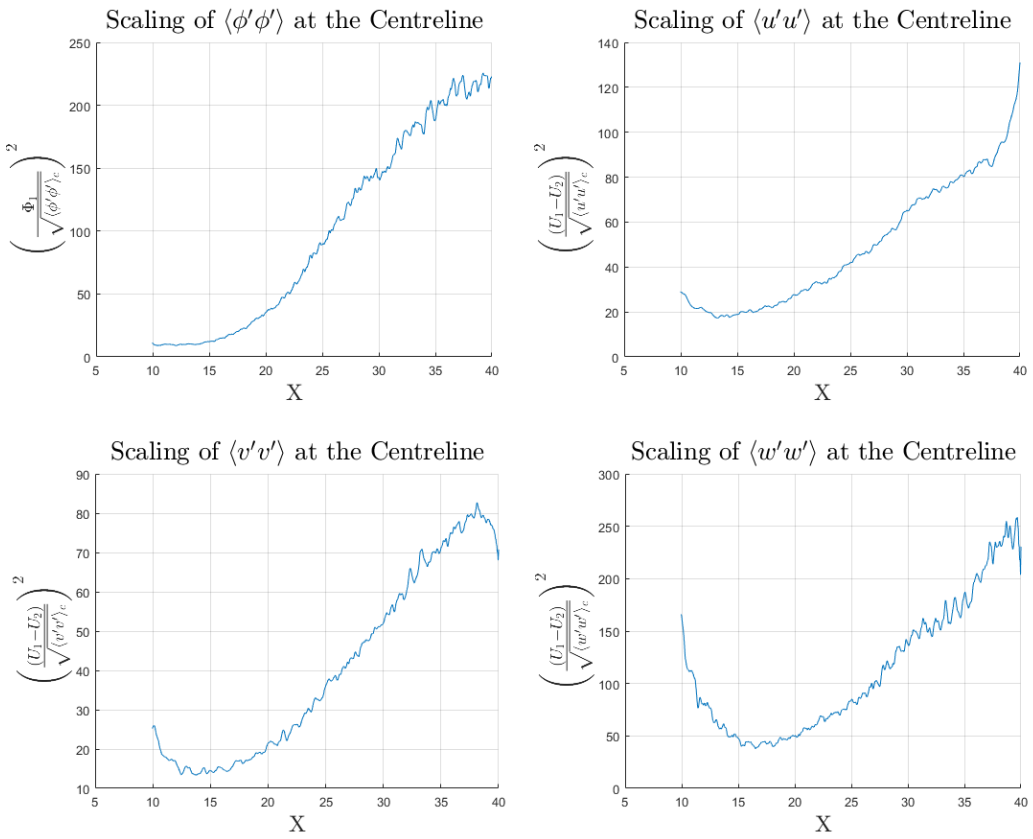

Figure 4.7: Evolution of the scalar variance at the centreline (top left); evolution of the streamwise velocity variance at the centreline (top right); evolution of the cross-stream velocity variance at the centreline (bottom left); evolution of spanwise velocity variance at the centreline (bottom right)

From the graphs in Figure 4.6 and 4.7, it can be found that the self-similarity region extends approximately from unit length 22.5 to 32.5 in the x direction. In this region, the computed rate of spreading is $S = 0.097$ consistently with the theory [2]. In the graphs representing the statistics related to U_c and to $y_{1/2}$, the linearity of the trend is less pronounced than in the other statistics. This is probably due to the presence of the co-flow that is slowing down in the direction of the development of the jet. In the last region of the statistics related to the variances it can be noticed the effect of the outflow condition. For this reason, the last part of the domain is not

considered in the study of the self-similarity.

Coherently with these observations, the self-similarity of different quantities is shown in Figure 4.8 and 4.9.

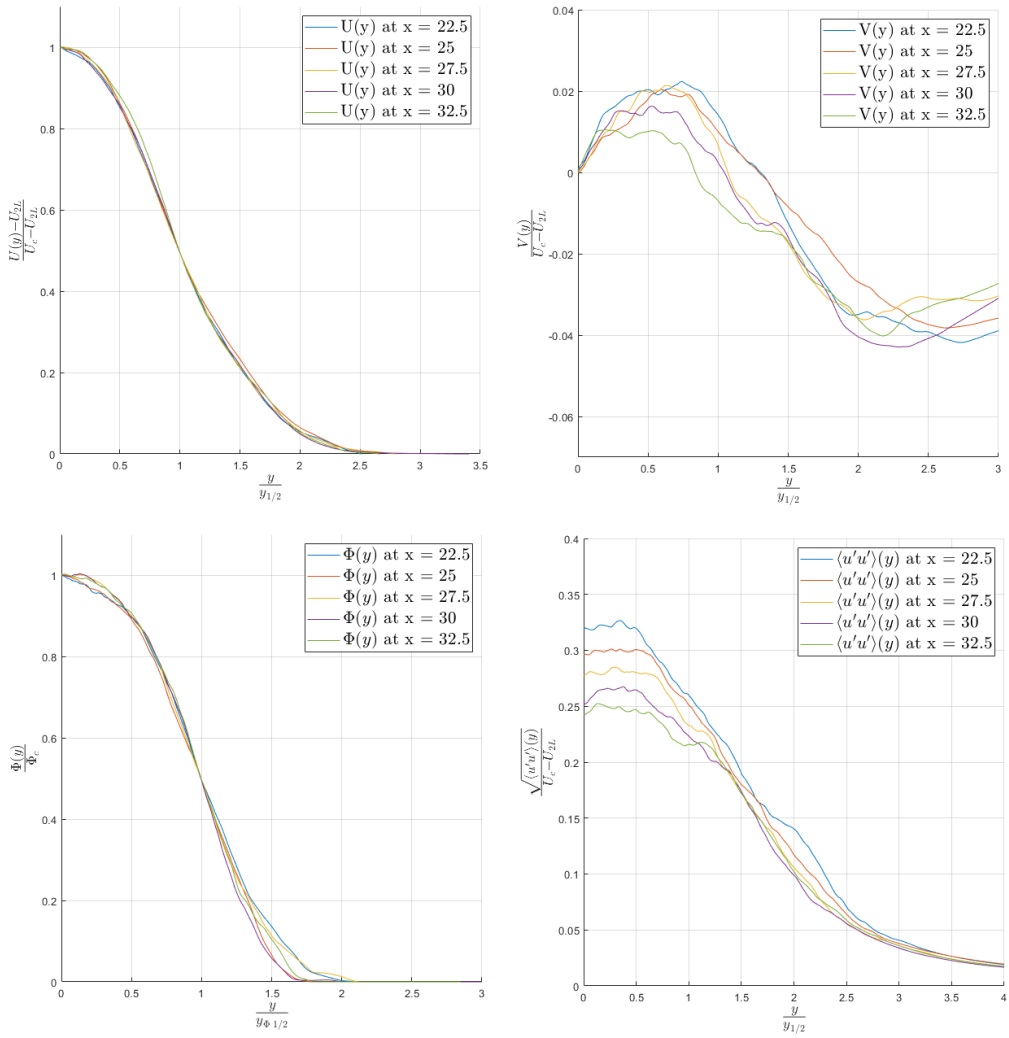

Figure 4.8: Self-similar profiles: streamwise velocity component (top left); cross-stream velocity component (top right); passive scalar (bottom left); streamwise velocity variance (bottom right)

All the profiles related to the velocity components have been normalized with the local centreline velocity difference, hence computed with respect to

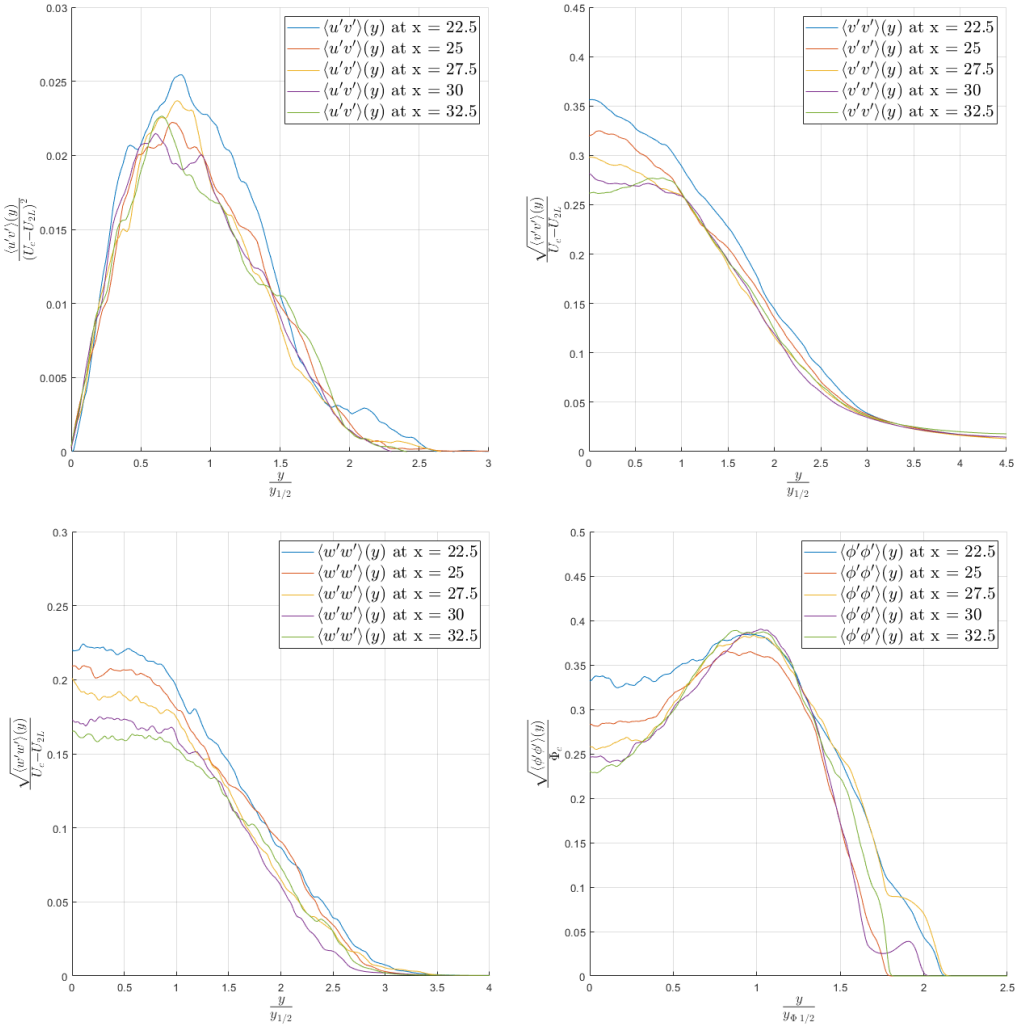

Figure 4.9: Self-similar profiles: u and v covariance (top left); cross-stream velocity variance (top right); spanwise velocity variance (bottom left); scalar variance (bottom right)

the local co-flow U_{2L}.

The self-similar behaviour is well pronounced in the mean profiles of the streamwise velocity component and of the scalar, while it is less evident in the variances. The fact that the latter are less smooth than $U(y)$ and $\Phi(y)$ is expected since they are second order moments.

The profiles of the scalar variance seem to reach the self-similarity regime later than the other quantities. This can be noticed from the difference between the profile corresponding to x unit length equal 22.5 and the other profiles. In accordance with this, also the graph of the scaling of the scalar variance (Figure 4.9) present a linear behaviour in a region further downstream with respect to the other quantities.

4.4 Turbulent Scales

Other interesting statistics have been studied. In particular, the dissipation, the Kolmogorov scale, the Taylor micro-scale and the Re_λ have been computed by averaging in time and in z direction on the jet midplane (x-z plane). These statistics are shown in Figure 4.10.

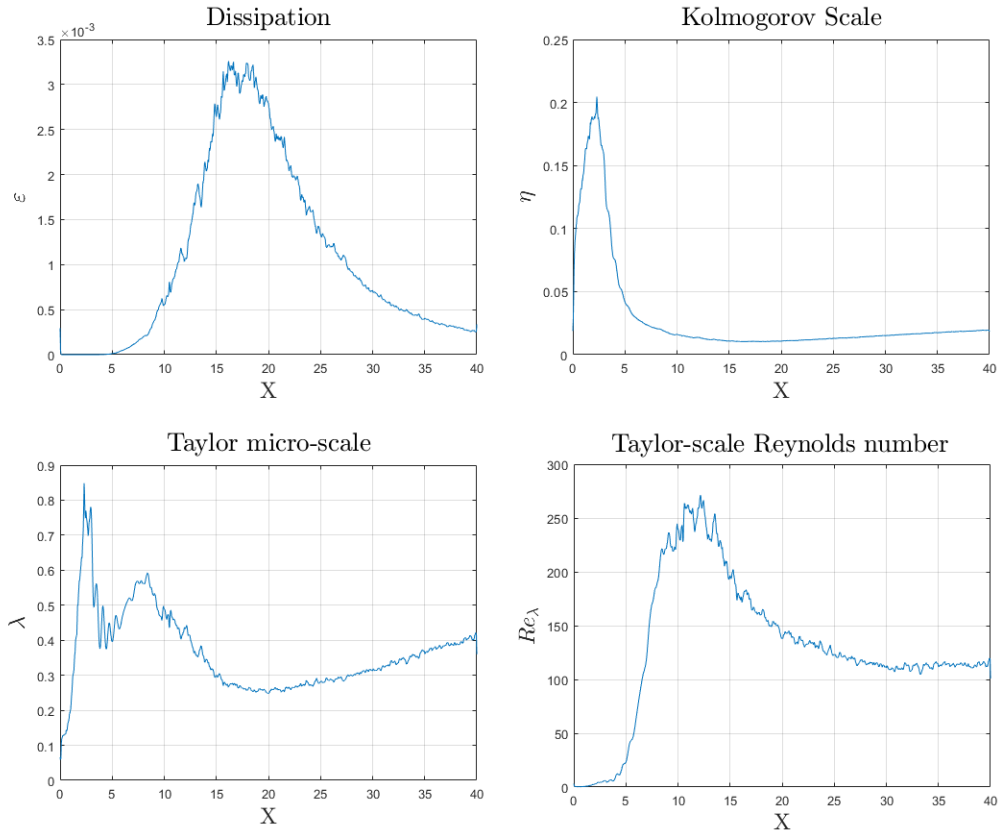

Figure 4.10: Centreline quantities: Turbulent dissipation (top left); Kolmogorov scale (top right); Taylor micro-scale (bottom left); Reynolds lambda (bottom right)

Both the Taylor micro-scale and the Kolmogorov scale show an increasing trend after reaching the minimum value around 15/20 unit lengths. In the final part of the domain, the ratio between the Taylor micro-scale and the Kolmogorov scale remains constant around an approximative value of 21 (Figure 4.11).

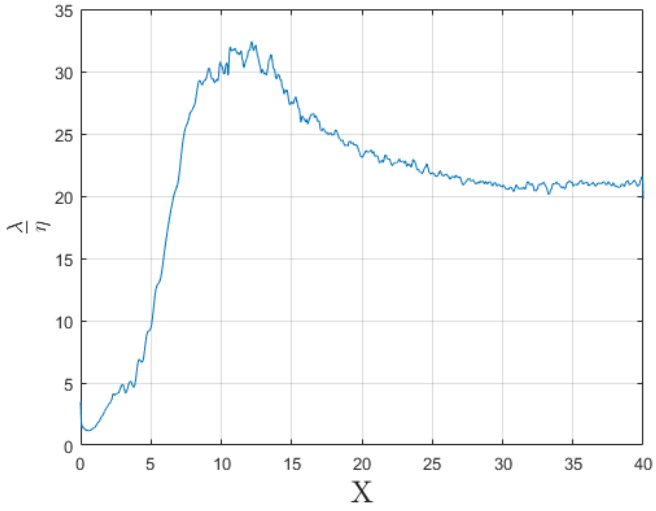

Figure 4.11: Taylor micro-scale over Kolmogorov scale ratio at the centreline

The minimum value of the Kolmogorov scale is around 0.01 unit lengths, leading to a maximum $\frac{\Delta x}{\eta} = 3.8$. The resolution increase going downstream (due to the increase of η) with a final value at the outlet of $\frac{\Delta x}{\eta} = 2.1$.

As expected, the value of the Re_λ stabilizes to a constant value after an initial settling. The mean value of the Re_λ in the final part of the domain at the centreline is around 115.

Chapter 5

Temporal Planar Jet

Before starting with the numerical experiments aimed at the understanding of turbulent entrainment, all settings have been validated through a benchmark DNS simulation. The settings and the results obtained are reported in the following sections.

The experiments presented in Chapter 6 (and so, also for the present validation) are performed on temporal planar jets with the same settings reported below.

This kind of flow has been chosen because it requires a lower computational cost if compared with the spatially developing planar jet (with the same Reynolds number).

5.1 DNS Settings

Before performing the benchmark simulation taken into consideration in the results, a preliminary simulation has been performed in order to define the grid spacing needed (based on the Kolmogorov scale) and the crossflow dimension of the domain L_y. From this preliminary simulation, the time unit at which the self-similarity begins has been identified and the y-direction of the domain has been defined in such a way to obtain the free development of the spreading jet (with negligible confinement effects) for a period of time

long enough to observe the evolution of the desires statistics.

The Reynolds number is set to $Re = 3000$ and the Schmidt number is set to $Sc = 1$.

5.1.1 Domain

The dimensions of the domain on which the preliminary simulation has been performed ($L_x \times L_y \times L_z$) are $24h \times 12h \times 5h$.

From the theory, it is known that the quantities reported in the following graphs (Figure 5.2) are expected to be linearly varying with time. By looking at these graphs it is possible to estimate the time at which the jet begins to be influenced by the confinement effect.

Looking at the Figure 5.1 and 5.2, it can be noticed that the self-similarity starts approximatively from the time unit 40. Confinement effects can be noticed to start approximatively around time unit 70.

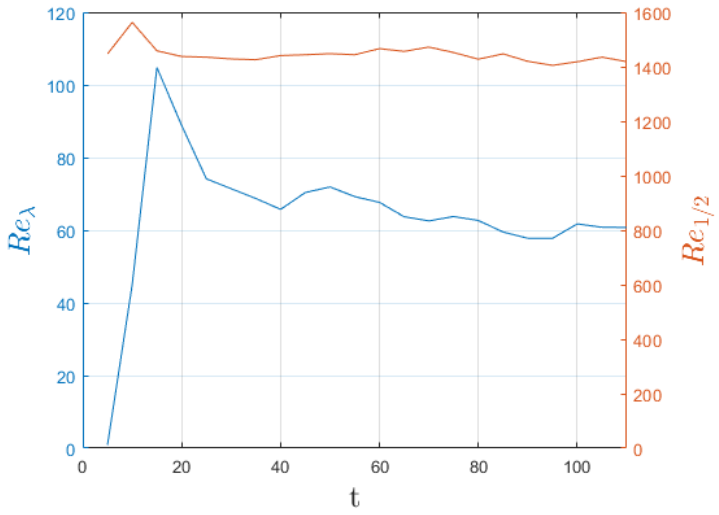

Figure 5.1: Preliminary simulation: Re_λ at the centreline and $Re_{1/2}$

The contours of the scalar at time unit 70 and at $z = 2.5$ is reported in Figure 5.3.

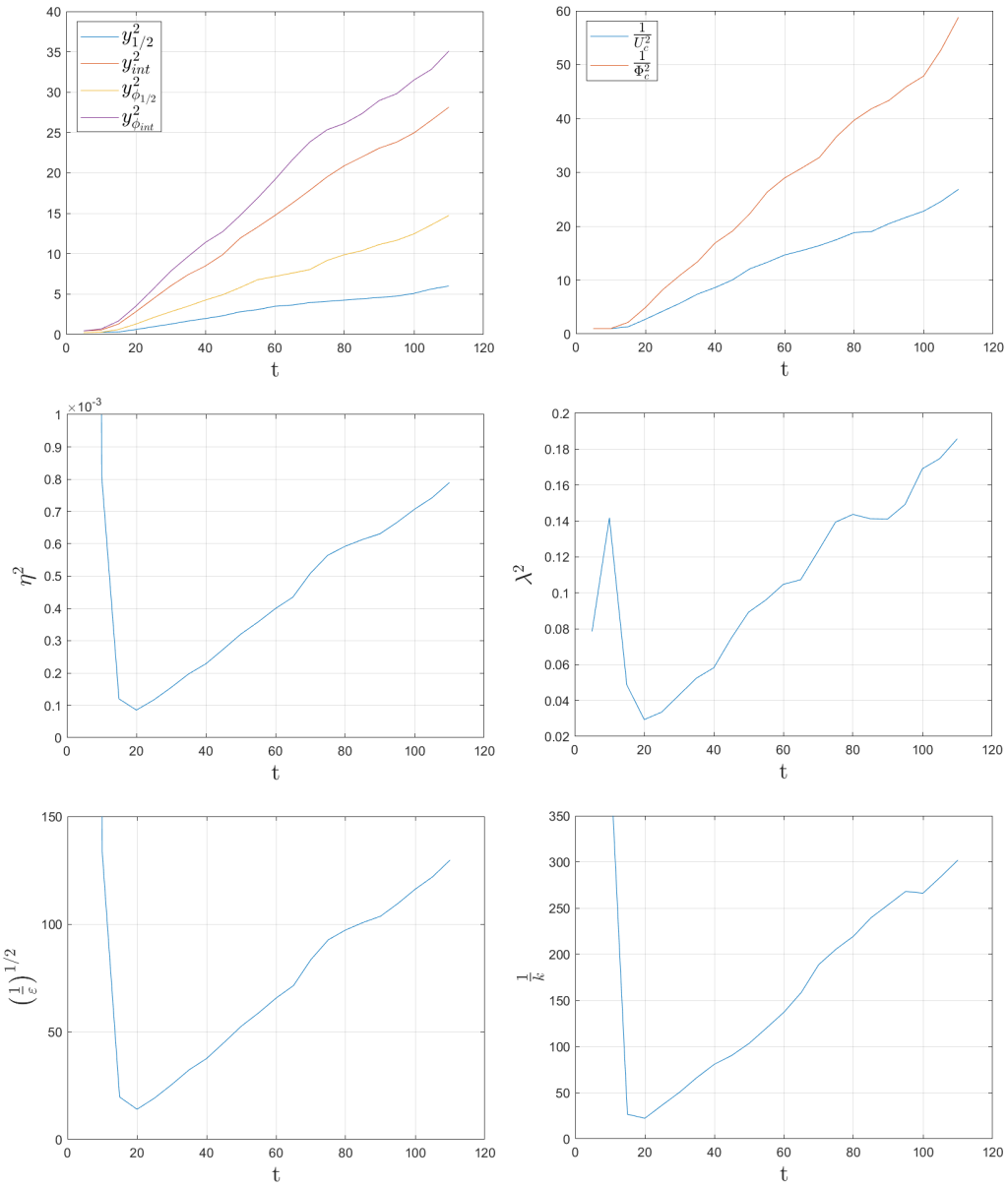

Figure 5.2: Preliminary simulation scalings: jet half-width and jet interface (top left); mean scalar and velocity at the centreline (top rigth); Kolmogorov scale at the centreline (middle left); Taylor micro-scale at the centreline (middle right); turbulent dissipation at the centreline (bottom left); turbulent kinetic energy at the centreline (bottom right)

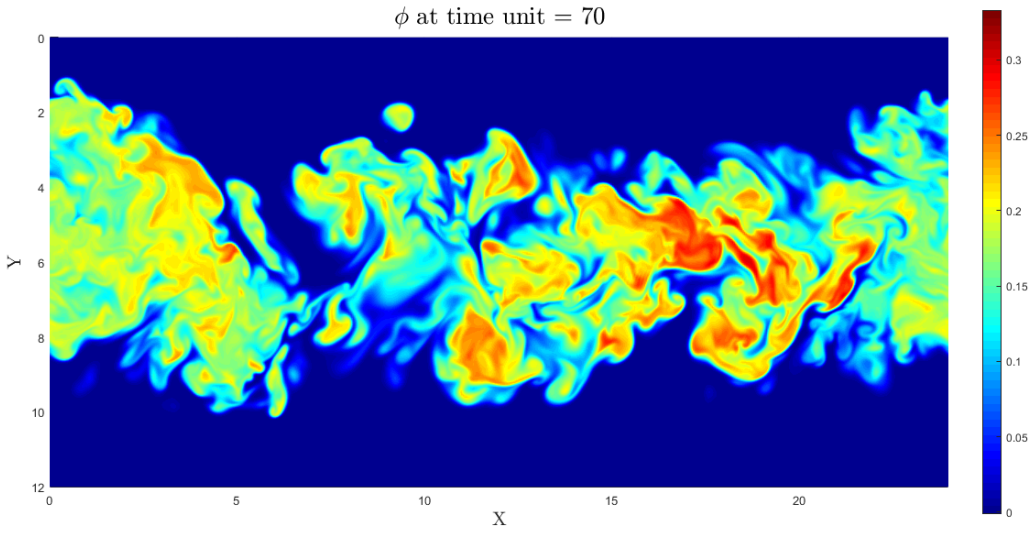

Figure 5.3: Preliminary simulation: scalar contours at $z = 2.5$ and $t = 70$ (beginning of significant confinement effects)

From this image, it can be noticed that the interface of the jet is approaching the boundaries of the domain.

The target for the final validating simulation, in terms of time, has been set to indicatively 140 time-units. Since the width of the jet increases proportionally with the square root of the time, and since $\sqrt{140/70} \approx 1.41$, the y dimension of the domain has been increased from 12 to 18 unit-lengths, in order to extend the self-similarity interval with negligible confinement effects.

Hence, the dimensions of the domain for the final simulations have been set to be $24h \times 18h \times 7h$ ($L_x \times L_y \times L_z$). The increase in the z dimension is a consequence of the decision to reduce the resolution in that direction and will be explained in the following subsection.

5.1.2 Mesh and Time-step

Cartesian and uniform grids have been used in both the preliminary and the final simulations. The spatial discretization of the domain for the preliminary simulation is defined by ($N_x \times N_y \times N_z$) $614 \times 312 \times 128$ points, resulting in 24520704 elements. The obtained grid spacings are: $\Delta x \approx \Delta y \approx \Delta z \approx 0.039$.

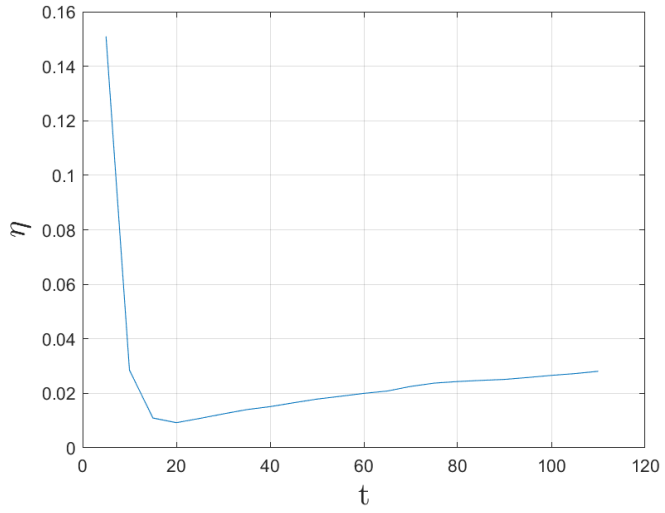

Figure 5.4: Preliminary simulation: Kolmogorov scale at the centreline

Once the preliminary simulation has been performed, the trend of the Kolmogorov scale has been computed in the centreline of the jet (where the Kolmogorov scale is smaller) in order to define more appropriately the grid spacings for the final simulation. The result is shown in Figure 5.4.

Since this study is primarily focused on the self-similarity region interval, it has been decided to size the grid spacing in order to have the desired resolution from time unit 40 on. The value of the Kolmogorov scale at that time unit is $\eta \approx 0.015$. The resolution is chosen to be $\frac{\Delta x}{\eta} = 3.9$, $\frac{\Delta y}{\eta} = 2.5$ and $\frac{\Delta z}{\eta} = 3.6$. The resolution obviously increase as time goes on in the simulation.

These considerations led to a mesh defined by $(N_x \times N_y \times N_z)$ $412 \times 472 \times 128$ (resulting in 24891392 grid points) defined on the new domain $(L_x \times L_y \times L_z)$ $24 \times 18 \times 7$. The resulting grid spacings are $\Delta x \approx 0.058$, $\Delta y \approx 0.038$ and $\Delta z \approx 0.055$.

The same time-step and the same methods for time advancement have been used in both the simulations. The time-step selected is 0.01 time units leading to a Courant number of 0.3, considering the smallest grid spacing and a maximum velocity of 1.2. Runge-Kutta 3 method has been used for

the advancement in time.

5.1.3 Boundary conditions and Initial Condition

Periodic boundary conditions have been used in all the directions both in the preliminary and in the final simulations.

The initial condition for the velocity has been defined (for both simulations) as:

$$u\left(x,y,z,t=0\right)=\frac{U_1}{2}\left(1+\tanh\left(\left(0.5-\mid y\mid\right)\cdot\frac{35}{2}\right)\right)\cdot\left(1+noise\right) \quad (5.1)$$

Where U_1 is the velocity of the jet and is set to 1. The mean initial condition for the x component of the velocity is shown in Figure 5.5.

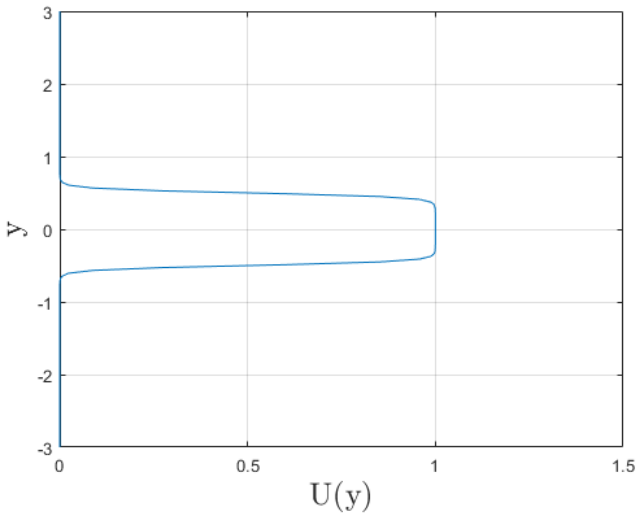

Figure 5.5: Temporal planar jet: initial condition for the streamwise velocity

The simulations have been performed at a Reynold number, defined as $Re=\frac{U_1 h}{\upsilon}=3000$. The noise is set to be a white noise with zero mean and 0.01 amplitude. The noise has been added also to the other velocity components, initialized with a zero-mean value. The role of the noise, as in the spatially developing planar jet, is to anticipate the transition to turbulence. The initial

condition for the passive scalar is the following:

$$\phi\left(x, y, z, t=0\right) = \frac{\Phi_1}{2}\left(1 + \tanh\left((0.5 - \mid y \mid) \cdot \frac{35}{2}\right)\right) \tag{5.2}$$

Where Φ_1 is set to 1.

5.1.4 Statistical Symmetries

The temporal planar jet presents some statistical symmetries. In particular, x and z are statistically homogeneous directions. On the other hand, time and the crossflow direction are not homogeneous. As in the spatially developing planar jet, the flow is statistically symmetrical with respect to the x-z midplane. For these reasons, the average operations have been performed in x, z and between specular values around the x-z midplane.

5.2 Flow Topology

As a first step of the post processing, the contours of the scalar corresponding to different time units have been checked (Figure 5.6). All the slices represented are x-y planes located at z coordinate equals to 3.5. The contours of the other quantities are not reported for the sake of brevity.

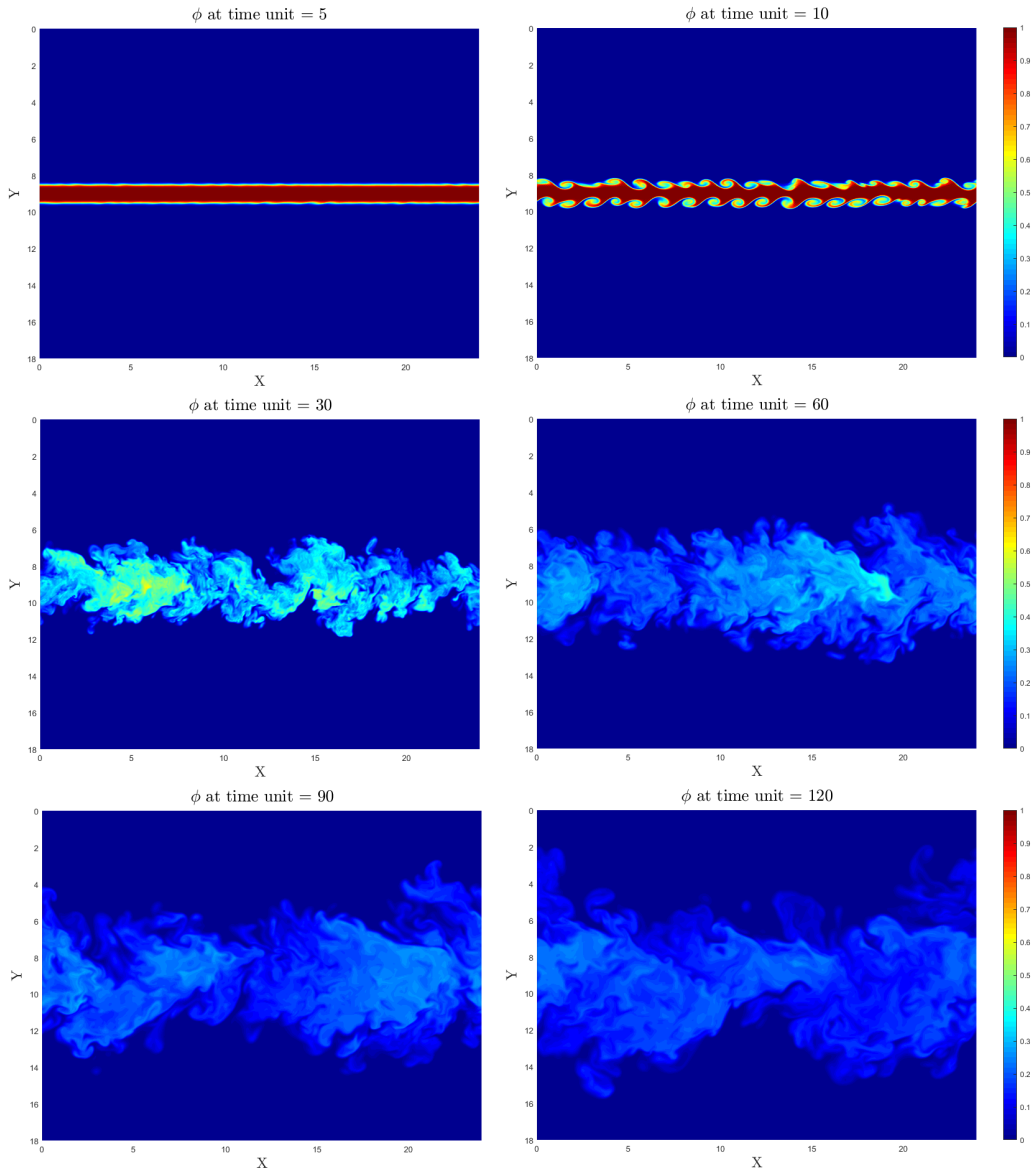

Figure 5.6: Temporal planar jet: passive scalar contours at different time units

The slice corresponding to time unit 5 is very similar to the initial condition. In the slice corresponding to time unit 10, Kelvin-Helmholtz-like structures can be noticed. In the following slices, the development of the jet can be observed.

5.3 Self-Similarity

In order to identify the self-similarity interval, some parameters have been studied. It is known from the theory that, in this kind of flow, U_c and Φ_c evolve as $t^{-1/2}$, while $y_{1/2}$ and $y_{\phi\,1/2}$ evolve as $t^{1/2}$ in the self-similar regime. Consequently, these and other parameters have been scaled in order to obtain a linear behaviour in that interval. Those quantities are shown in Figure 5.8.

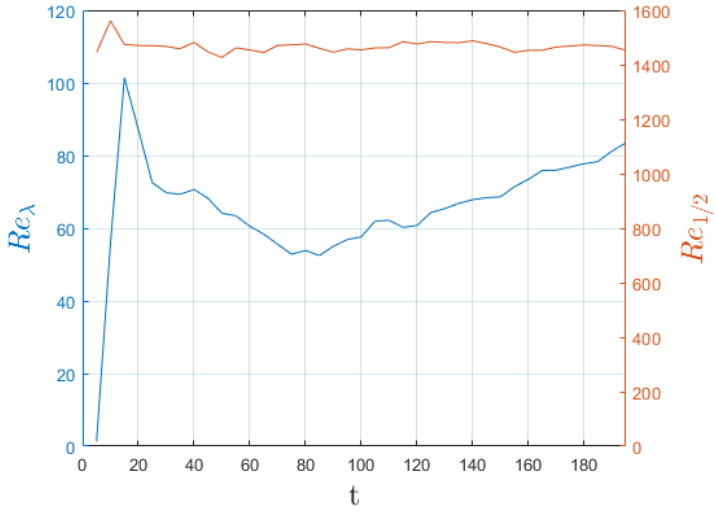

Figure 5.7: Final simulation: Re_λ at the centreline and $Re_{1/2}$

The dissipation, the turbulent kinetic energy, the Kolmogorov scale and the Taylor micro-scale have been computed at the centreline.

From the graphs in Figure 5.8, a linear trend can be identified between time unit 40 and time unit 120. This interval has been chosen in order to study the self-similarity. Some confinement effects can be noticed in all

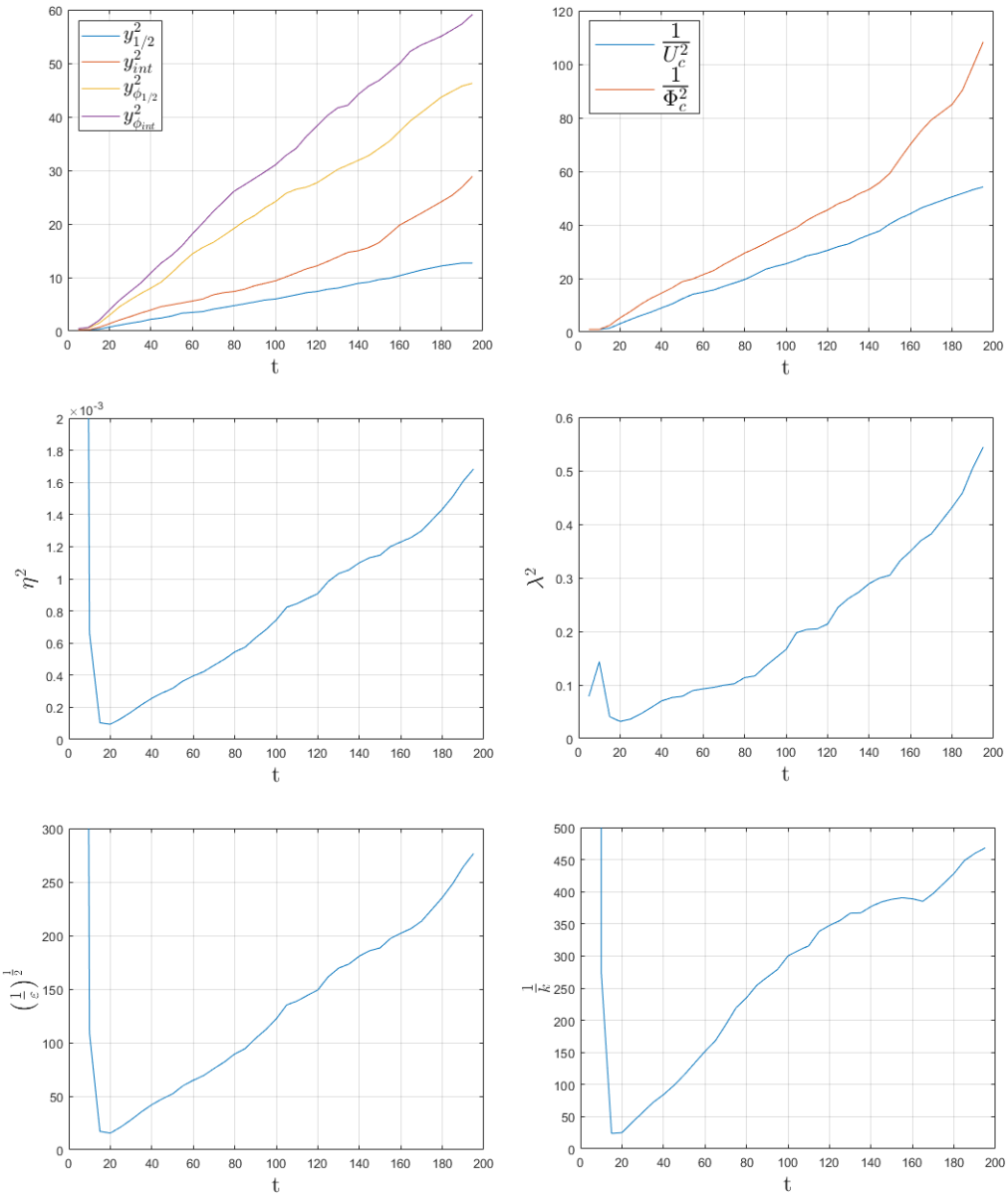

Figure 5.8: Final simulation scalings: jet half-width and jet interface (top left); mean scalar and velocity at the centreline (top rigth); Kolmogorov scale at the centreline (middle left); Taylor micro-scale at the centreline (middle right); turbulent dissipation at the centreline (bottom left); turbulent kinetic energy at the centreline (bottom right)

graphs, in particular, the first quantity to feel the presence of the boundaries seems to be the turbulent kinetic energy. Probably the graph of the Taylor micro-scale does not present a well pronounced linear behaviour for statistical convergence reasons. In fact, another identical simulation has been performed and the linear trend of the Taylor micro-scale is more marked. In Figure 5.7. the graphs of Re_λ and $Re_{1/2}$ are shown.

$Re_{1/2}$ presents a constant trend (around a value of 1500) as expected. Also Re_λ should settle around a constant value once turbulence is fully developed. Obviously, since the square of Taylor micro-scale does not present a marked linear trend, the Re_λ is not constant. Anyway, it can be seen that the value of Re_λ in the region of interest is approximatively around 60. Once identified the self-similarity interval, the profiles of some quantities have been plotted (Figure 5.9 and 5.10).

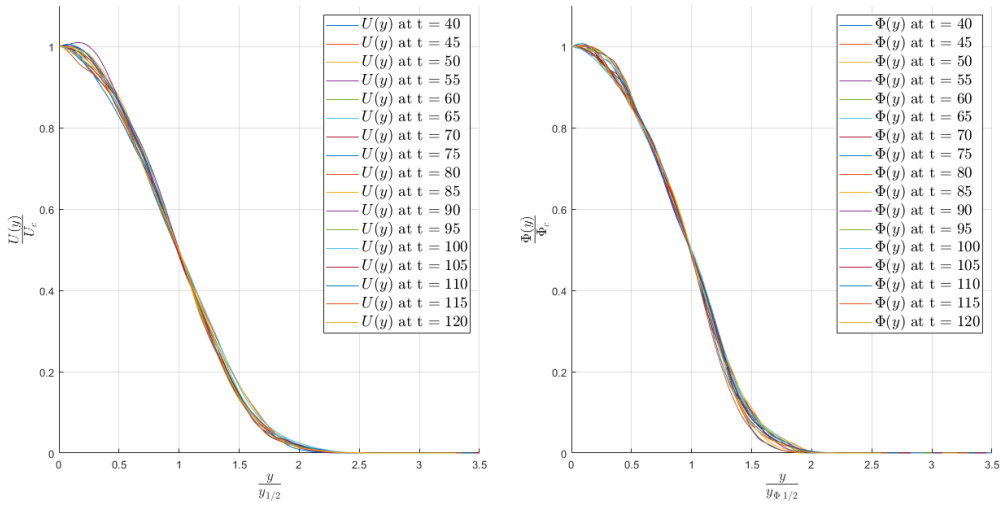

Figure 5.9: Self-similar profiles: streamwise velocity component (left); passive scalar (right)

All the profiles related to the velocity components have been normalized with the centreline velocity and all the profiles related to the scalar have been normalized with the centreline value of the scalar.

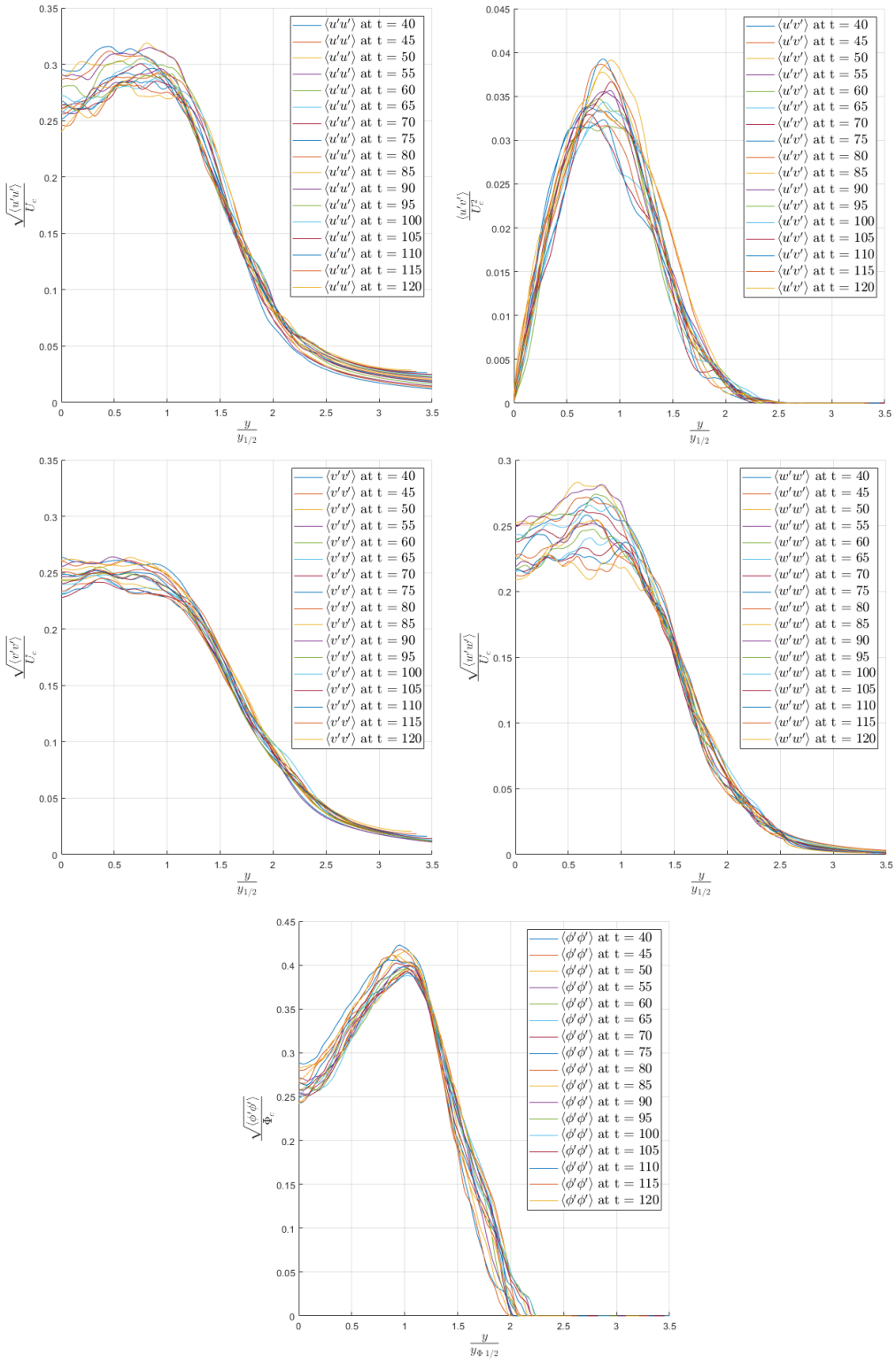

Figure 5.10: Self-similar profiles: streamwise velocity variance (top left); u and v covariance (top right); cross-stream velocity variance (middle left); streamwise velocity variance (middle right); scalar variance (bottom)

All the curves tend to collapse approximatively on the same profile. Probably, the mismatching between curves related to different time units is due to the relatively small number of samples ($2 \times N_x \times N_z = 105472$) on which the averaging operations have been performed (due to the relatively small domain, constrained for computational costsŕeasons). As in the spatially developing planar jet, the second order moments appear to be less smooth than the first order moments.

5.4 Turbulent Scales

In this paragraph, the graphs regarding the turbulent scales are presented. In the following Figure 5.11 k, ε, λ and η are reported.

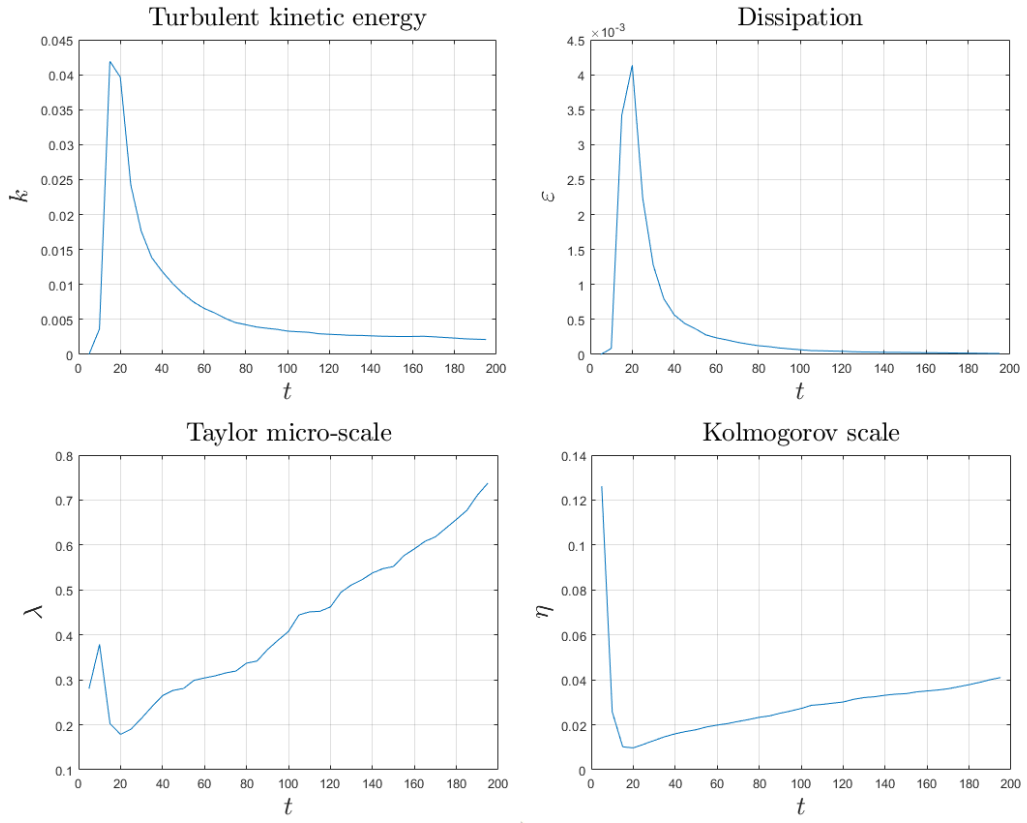

Figure 5.11: Centreline quantities: Turbulent kinetic energy (top left); turbulent dissipation (top right); Taylor scale (bottom left); Kolmogorov scale (bottom right)

As expected, turbulence is developed in the first time units and start decaying from approximatively time unit 30. Both the Taylor and the Kolmogorov scales increase in time. The value of the Kolmogorov scale at time unit 40 is 0.016 and reaches 0.030 at time unit 120. The resulting resolution is $\frac{\Delta x}{\eta} = 3.6$, $\frac{\Delta y}{\eta} = 2.4$ and $\frac{\Delta z}{\eta} = 3.4$ at time unit 40, in line with the desired values decided after the preliminary simulation. At time unit 120 (the end of the interval studied in the following experiments) the resolution improves up to $\frac{\Delta x}{\eta} = 1.9$, $\frac{\Delta y}{\eta} = 1.3$ and $\frac{\Delta z}{\eta} = 1.8$.

5.5 Two-Point Statistics

In order to obtain some information on the spatial turbulent structures, two-point statistics are necessary. In this section, two-point correlations and spectra of the fluctuations of the velocity components and of the scalar will be studied. All the statistics presented in this section have been computed at time unit 100 and at the y-coordinate corresponding to the mean position of the scalar interface. This coordinate has been chosen because, in the following sections, particular attention will be dedicated to the study of the evolution of the interface of the scalar. In Figure 5.12 and 5.13. the two-point correlations are shown.

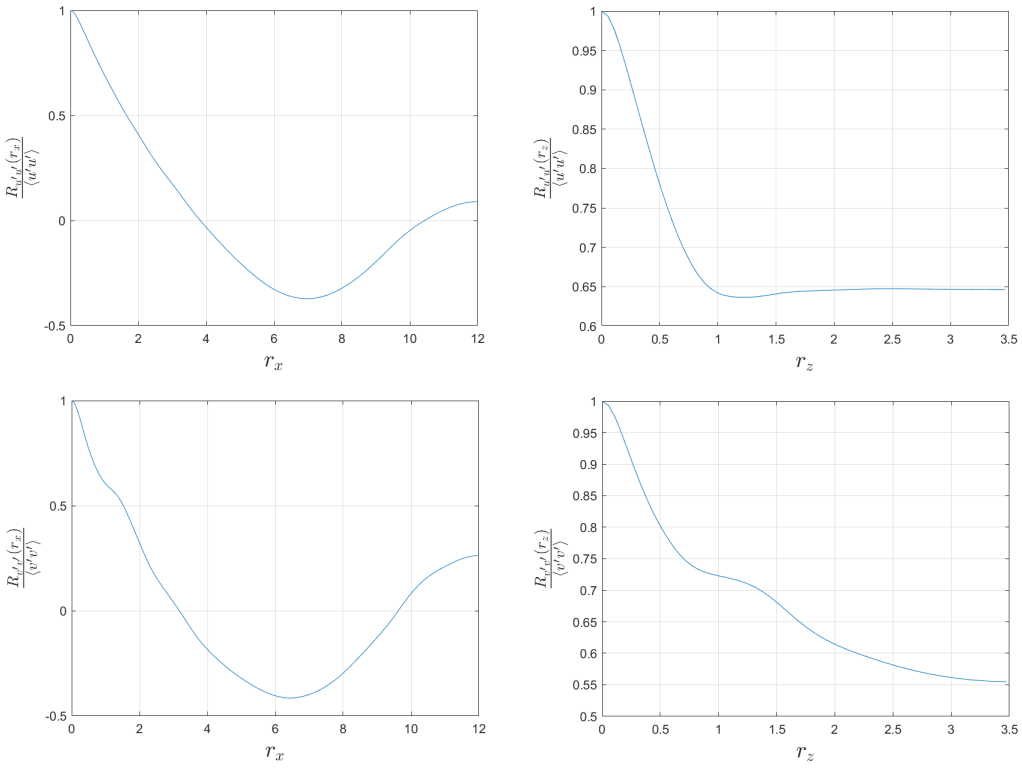

Figure 5.12: Two-point correlations of u' (top) in x (left) and z (right) directions; two-point correlations of v' (bottom) in x (left) and z (right) directions

In the two graphs regarding $R_{u'u'}(r_x)$ and $R_{v'v'}(r_x)$, a anticorrelation

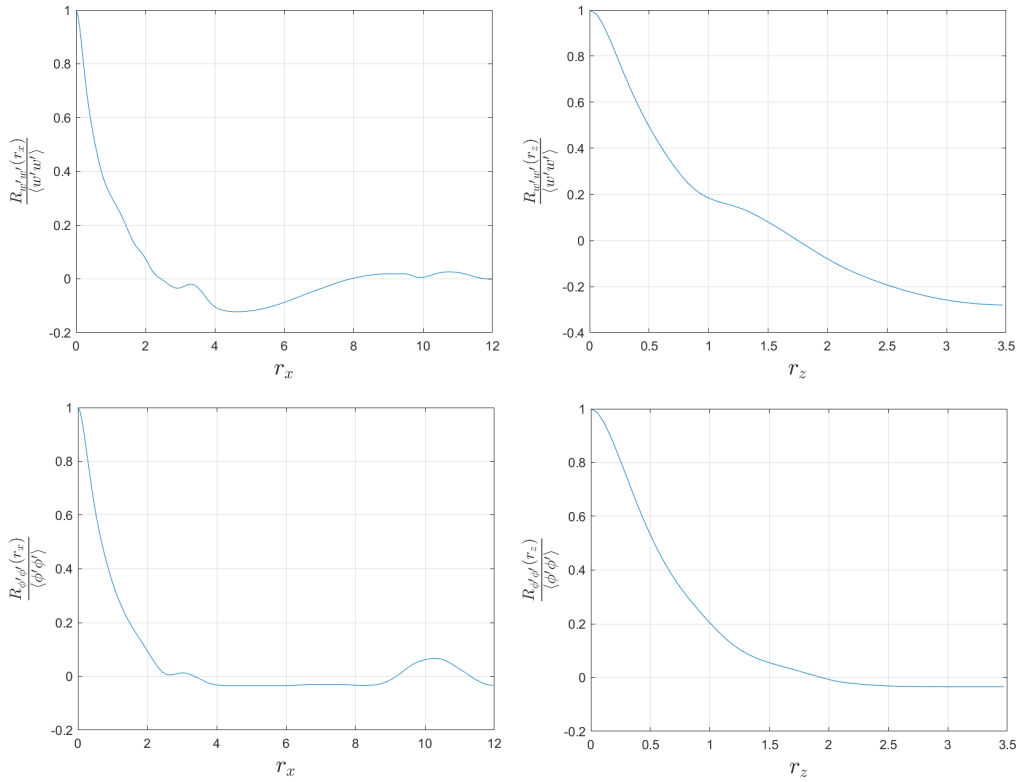

Figure 5.13: Two-point correlations of w' (top) in x (left) and z (right) directions; two-point correlations of ϕ' (bottom) in x (left) and z (right) directions

around values of r_x between 6 and 7 can be noticed. This is probably due to the presence of vortical structures reminiscent of the Kelvin-Helmholtz instability, aligned with the z direction (repeated in x) whose average dimension in x is around 6 and 7 unit lengths (at the considered time unit). These structures induce opposite cross stream velocities, as it can be deduced from the graph of $R_{v'v'}(r_x)$. Through this mechanism, fast moving fluid is transported from the core toward the outside of the jet and vice versa on the opposite side of the vortical structure.

It can be noticed that, in the graphs regarding $R_{u'u'}(r_z)$ and $R_{v'v'}(r_z)$, the correlations do not go to zero. This is probably due to the fact that the abovementioned structures are elongated in the z direction, and so, u' and v' do not vary to much in the z direction. This effect is enlarged by the fact

that the domain is small in the y direction.

By computing the Fourier transform of the two-point correlations, the spectra are obtained. These spectra are shown in Figure 5.14 and 5.15.

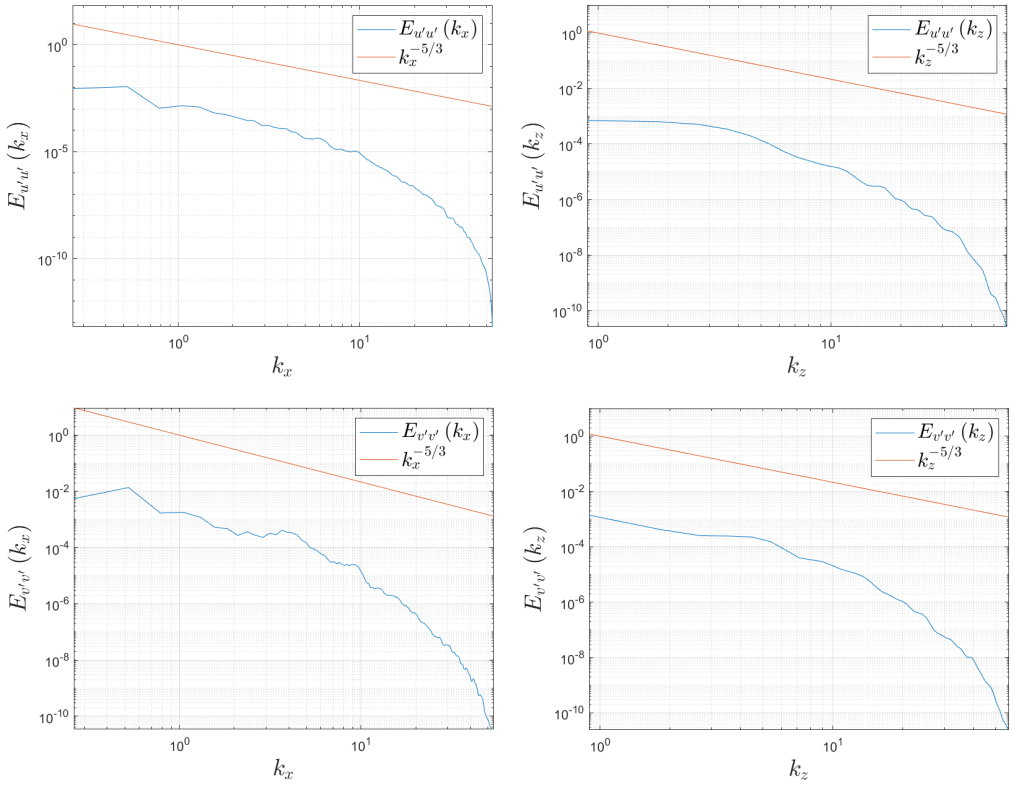

Figure 5.14: Energy spectra of u' in k_x (top left) and in k_z (top right); Energy spectra of v' in k_x (bottom left) and in k_z (bottom right);

All the spectra have been computed on the x-z plane corresponding to the mean position of the interface. The plots regarding the velocity components show how the energy of the fluctuations is distributed between the scales. These graphs have been useful for the choice of the filter length for the following experiments.

As a reference, the trend of $k_{x_i}^{-5/3}$ is reported. The inertial subrange is not well marked because of the relatively small Reynolds number.

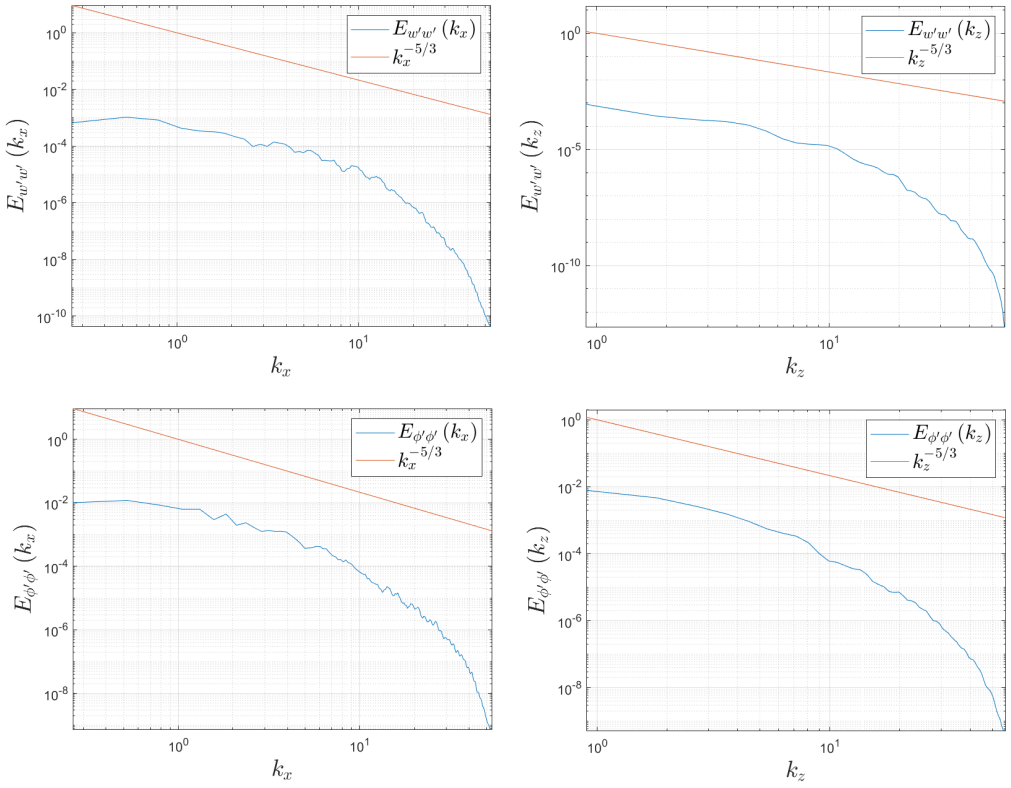

Figure 5.15: Energy spectra of w' in k_x (top left) and in k_z (top right); Energy spectra of ϕ' in k_x (bottom left) and in k_z (bottom right);

Chapter 6

Numerical Experiments on Temporal Jets

In this chapter, some numerical experiments aimed to investigate the role of engulfment and nibbling in the turbulent entrainment are presented. In particular, the experiments have been conducted on temporal planar jets. Before starting with the experiments, all the settings have been validated through a benchmark DNS simulation, presented in Chapter 5.

The idea behind these experiments is the following: since engulfment is a large-scale phenomenon, and nibbling is a small-scale one, some information on the role of these two mechanisms could be obtained by studying the spreading of a passive scalar under the effect of filtered velocity fields. For each experiment, two simulations have been carried out, respectively aimed to study the effects of the large and of the small scales. For the first type simulations, a filtered velocity has been used (defined in Equation 6.1):

$$\tilde{\mathbf{u}}\left(\mathbf{x},t\right)=\int G\left(\mathbf{r},\mathbf{x}\right)\mathbf{u}\left(\mathbf{x}-\mathbf{r},t\right)d\mathbf{r} \tag{6.1}$$

Where $\mathbf{G}\left(\mathbf{x},\mathbf{r}\right)$ is the kernel and for the box filter is defined as follows (Equation 6.2):

$$G\left(x-r\right)=\begin{cases}\frac{1}{\Delta},\ if\mid x-r\mid\leqslant\frac{\Delta}{2},\\ 0,\ otherwise\end{cases} \tag{6.2}$$

Where Δ is the filter length. In terms of physical meaning, the application of this filter is equivalent to the replacement of the value of the velocity in one point with the mean value computed on the parallelepiped with the considered point as a centroid and with the three filter lengths as dimensions (the equivalent in two dimensions is obtained considering a rectangle).

For the second type of simulations, the real velocity, minus the filtered one, plus the average velocity field has been used (Equation 6.6). This choice comes from the fact that, by subtracting the filtered velocity from the real one, also the average is cancelled out, causing the scalar to remain in its initial position and gradually diffuse under the effect of the small scales passing through (Appendix). In order to let the scalar be convected downstream, the average velocity field (computed averaging in the homogeneous directions x and z at each time-step in real time in the simulation) has been added.

The resulting complete set of equations is presented below (Equations 6.3, 6.4, 6.5 and 6.6):

$$\frac{\partial u_i}{\partial x_i} = 0 \tag{6.3}$$

$$\frac{\partial u_i}{\partial t} + \frac{\partial u_i u_j}{\partial x_j} = -\frac{\partial p}{\partial x_i} + \frac{1}{Re}\frac{\partial^2 u_i}{\partial x_j \partial x_j} \tag{6.4}$$

$$\frac{\partial \phi_l}{\partial t} + \tilde{u}_i \frac{\partial \phi_l}{\partial x_i} = D\frac{\partial^2 \phi_l}{\partial x_i \partial x_i} \tag{6.5}$$

$$\frac{\partial \phi_s}{\partial t} + (u_i - \tilde{u}_i + U_i)\frac{\partial \phi_s}{\partial x_i} = D\frac{\partial^2 \phi_s}{\partial x_i \partial x_i} \tag{6.6}$$

Where ϕ_l is the passive scalar transported by the large-scale velocity field, ϕ_s is the passive scalar transported by the small-scale velocity field, $\tilde{u}_i$ is the filtered velocity and U_i is the mean velocity field (note that it is different from zero only for the streamwise component).

Since all the statistics are function of time and also of the y direction, the filtering operation has been only performed in the two homogeneous directions (x and z).

Different filter lengths Δ have been tried. For each choice Δ, two approaches (so, four simulations) have been tested. These two approaches differ in terms of time unit of activation of the filter. In the first case, the filter is activated from time unit zero. In the second case, the diffusion of the scalar is studied by activating the filter from time unit 40 (when the self-similar regime begins). The reason behind this approach is that, in the small scales simulations with the filter activated from the time unit zero, the initial Kelvin-Helmholtz vortices are cancelled out by subtracting the filtered velocity to the real one. In this way, the scalar remains almost in its initial position because the small scales are produced after some time from the beginning, since turbulence is still developing. This fact results in a mismatching between the scalar interface and the vorticity one, where nibbling happens. By activating the filter after turbulence has developed, this problem is avoided. Obviously, the interfaces of the scalar and of the velocity will match only for few time units after the activation of the filter, but since the aim of this work is the study of the diffusion under the separate effects of two different mechanisms, this difference is expected.

As a first try, the filter lengths have been set to $\Delta_x \approx 0.23$ and $\Delta_z \approx 0.22$. This choice comes from the fact that the Taylor micro-scale in the centreline, at time unit 40 (beginning of the self-similarity and time of activation of the filter in the second approach) is approximatively that length (Figure 6.1). Since the thickness of the turbulent sublayer is of the order of the Taylor micro-scale [1], this length of Δ has been used.

In order to study the influence of the choice of the filter length on the results, a second experiment has been carried out with $\Delta_x \approx 0.93$ and $\Delta_z \approx 0.88$. This filter length has been chosen also based on the velocity spectra (computed at the mean scalar interface position) reported in Figure 5.14 and 5.15, and has been chosen such that the corresponding wavenumber falls in the inertial subrange.

A visual example of how the two filter lengths work is reported in Figure 6.2 (the two filtered velocities have been filtered also in z direction and this

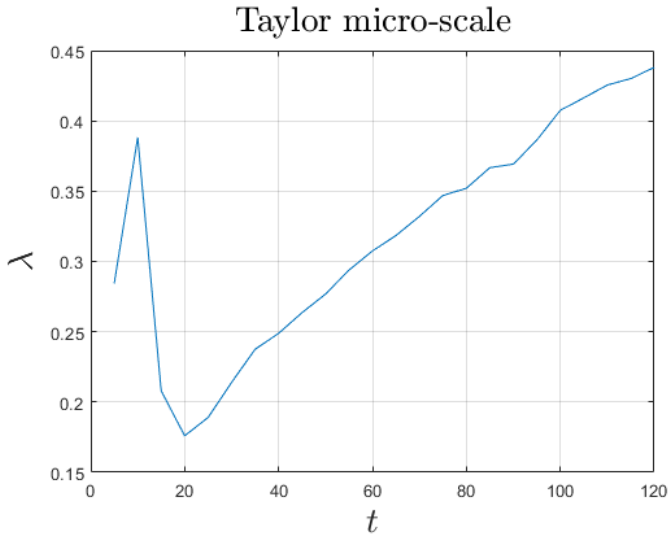

Figure 6.1: Taylor micro-scale

is the reason why they do not seem to exactly follow the mean value of the neighbourhood in x direction).

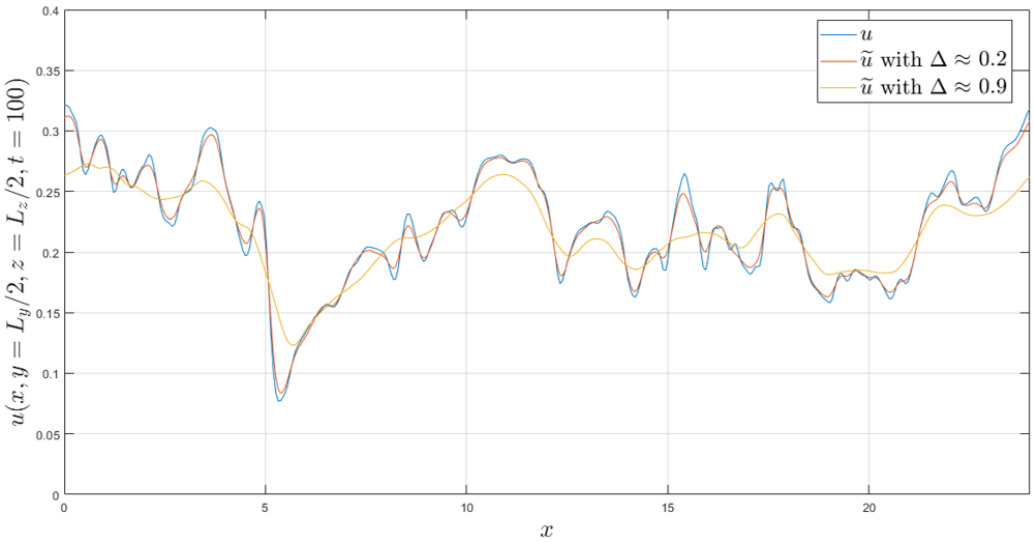

Figure 6.2: Example of the effects of the filtering operation

The Taylor and the Kolmogorov scales change in time, so, two further experiments have been performed with the filter length varying in time. Since,

in the self-similar interval, the Taylor and the Kolmogorov scales scale in the same way in the core and on the interface of the jet, the filter length has been chosen on the basis of the trend of the Taylor micro-scale computed in the centreline. The two values chosen for the experiments are $\Delta = 1.5\lambda_{cl}$ and $\Delta = 3\lambda_{cl}$. Since the Taylor micro-scale is meaningful only after turbulence is developed, the simulations with this time varying filter length have been performed only by activating the filter from time unit 40 on. The trends of the two filter lengths are shown in Figure 6.3 and 6.4.

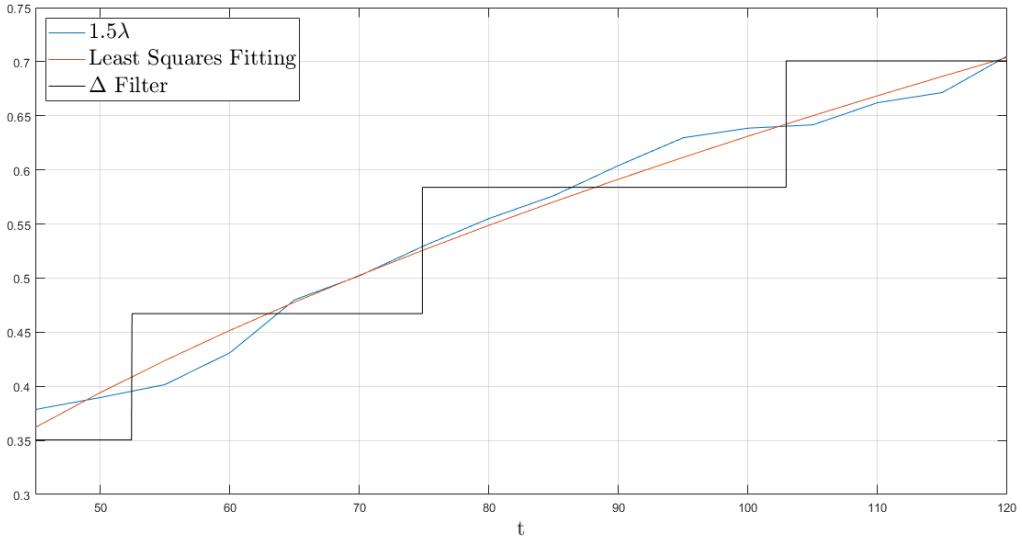

Figure 6.3: Filter length chosen for the first experiment

A least square fitting approach of the Taylor micro-scale has been used. The filter lengths have been chosen based on these fittings. Since the box filter used has been implemented on a discrete grid, also the values that can be chosen as Δ are discrete. This is the reason for the discontinuous trend shown in the Figures 6.3 and 6.4.

The numerical experiments in which the filter has been activated from time unit 0 did not gave interesting results because of the reasons explained above. The experiments with the constant filter lengths (with filter activation at time unit 40) gave more interesting results, but they are not reported in this chapter for the sake of clarity and brevity (they are reported in the

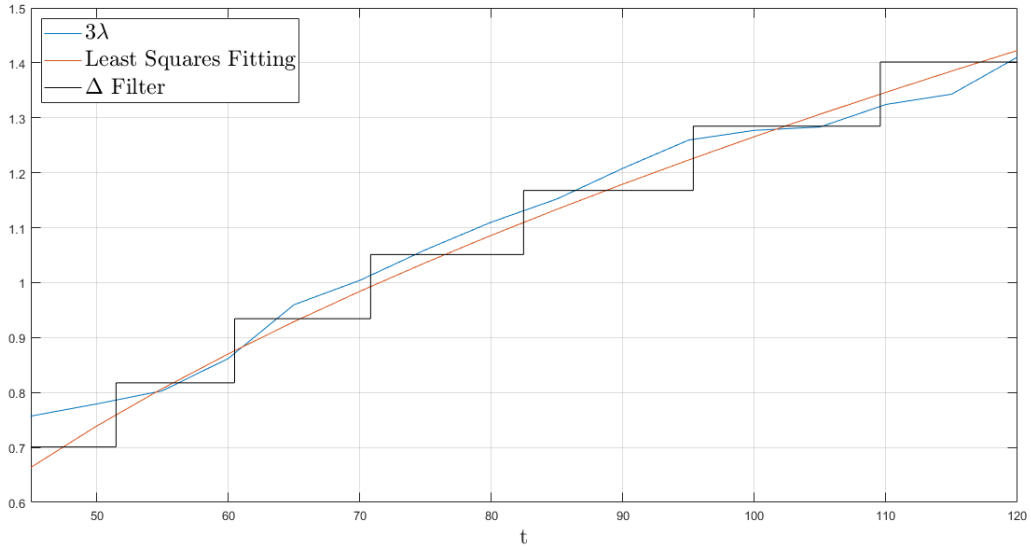

Figure 6.4: Filter length chosen for the second experiment

Appendix).

In the following sections, only the results obtained from the time varying filter length simulations are reported. Furthermore, only the statistics regarding the passive scalar are presented since the other statistics are not influenced by the procedure described above, and therefore do not add any useful information.

6.1 Flow Topology

The initial condition of the scalar field used for the experiments is reported in Figure 6.5 and is referred to time unit 40.

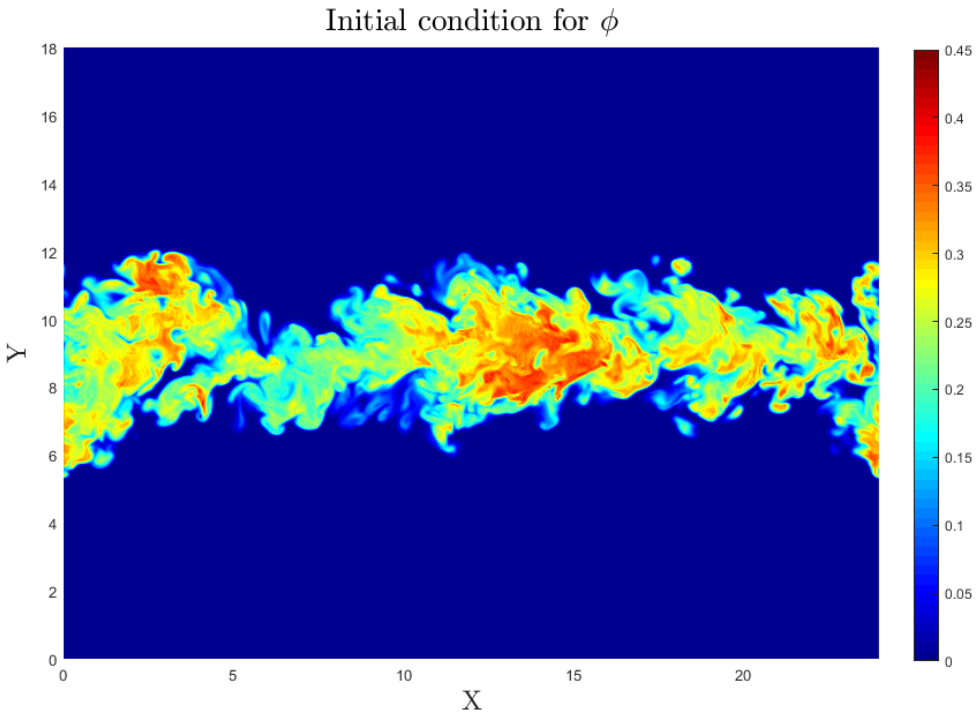

Figure 6.5: Scalar contours: Initial condition used for the experiments (x-y midplane), time unit 40

Starting from this condition (corresponding to time unit 40), the simulations have been run until time unit 120.

As a first step, the evolution of the passive scalar in the different simulations has been analysed. In Figure 6.6 and 6.7 the contours of the scalar in the x-y midplane are reported.

It can be immediately noticed that, the scalar spreads slower under the effect of the small scales with respect to the large scales cases, both with $\Delta = 1.5\lambda_{cl}$ and $\Delta = 3\lambda_{cl}$. To better visualize this difference in growth rate, the mean position of the scalar interface is plotted in Figure 6.8.

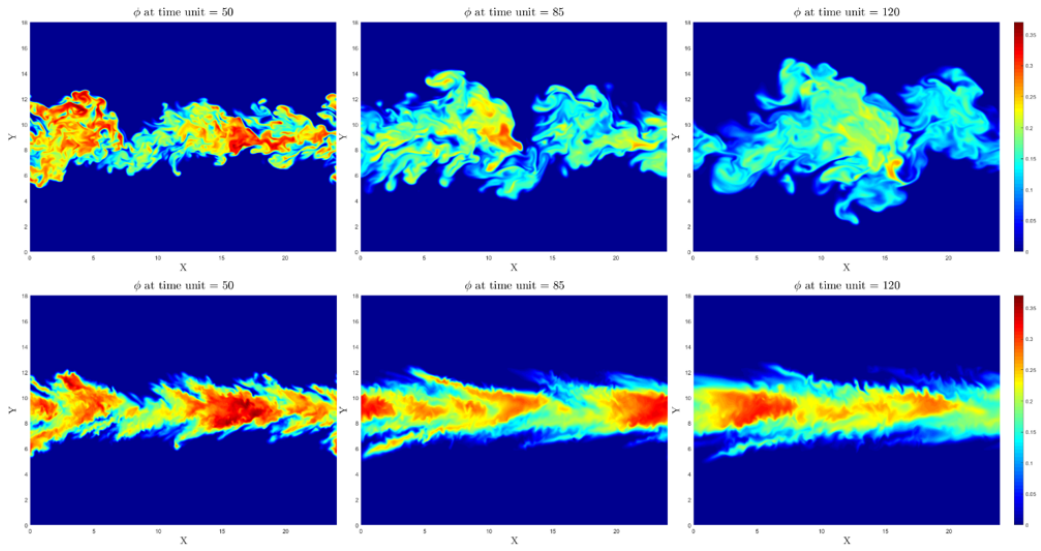

Figure 6.6: Scalar field evolution: $\Delta = 1.5\lambda_{cl}$, ϕ_l (top); ϕ_s (bottom)

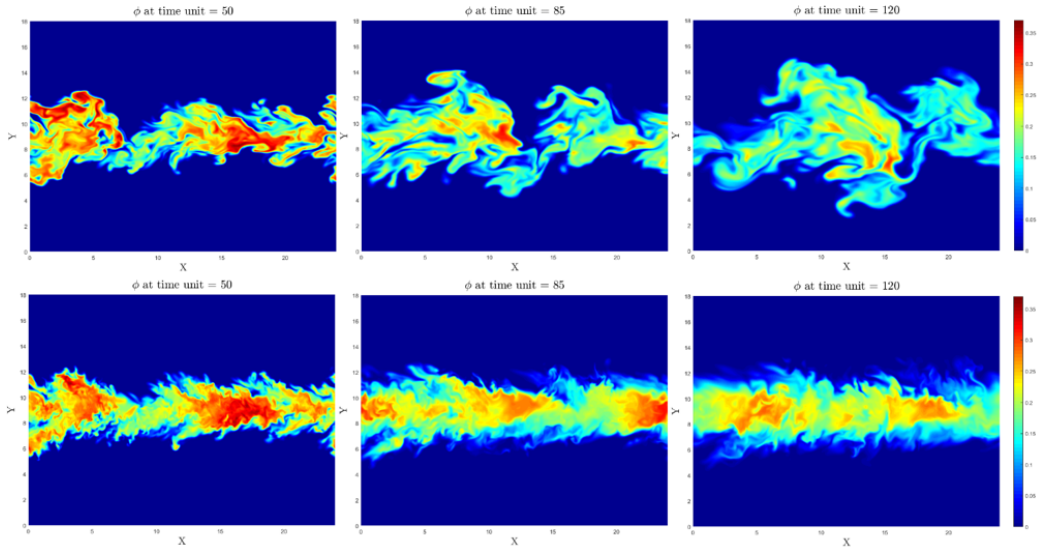

Figure 6.7: Scalar field evolution: $\Delta = 3\lambda_{cl}$, ϕ_l (top); ϕ_s (bottom)

In the small-scales simulations, the scalar field is stretched by the mean velocity field, leading to an arrow-shaped look. This happens because, in the initial condition, some regions of engulfing fluid are present. These regions continue developing in the large-scales simulations, while, in the small-scales ones, they gradually diffuse under the small scales action and get stretched

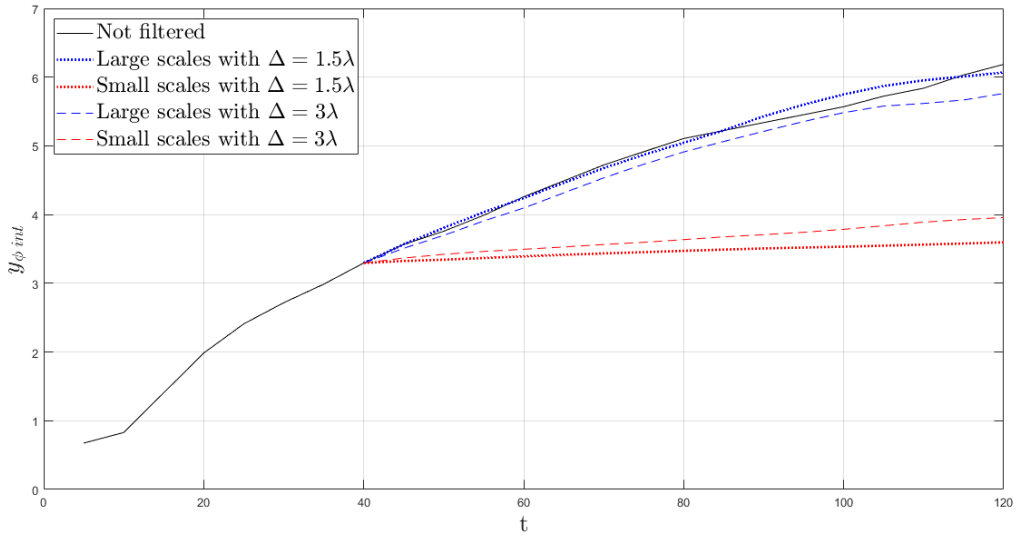

Figure 6.8: Mean scalar interface evolution comparison

by the mean flow. These stretched structures seem to be gradually cancelled out by the small-scale fluctuations. Anyway, because of the short time of development (due to the necessity to use a relatively small cross flow dimension for computational cost reasons), these structures are still visible in the last time instant of the simulations. So, the small scales seem to even out the large anisotropic structures related to engulfment. This effect can be better visualized in Figure 6.9 (referred to time unit 100).

The scalar interfaces in the small-scales simulations appear more flat and corrugated with respect to the large-scales ones.

Another observation is that, in the core of the jet (in both the simulations with $\Delta = 1.5\lambda_{cl}$ and $\Delta = 3\lambda_{cl}$), in the small-scales simulations, the scalar is much more evenly distributed than in the large-scales ones. In fact, in the large-scales simulations there are regions in the core of the jet with a value of the scalar near to zero, as shown in Figure 6.10 (time unit 100 and located at x-z midplane). From this, it could be deduced that, while the large scales largely contribute to the spreading of the jet, the small scales predominate the mixing process inside the core of the jet, tending to uniform the scalar field and evening out the large inhomogeneities.

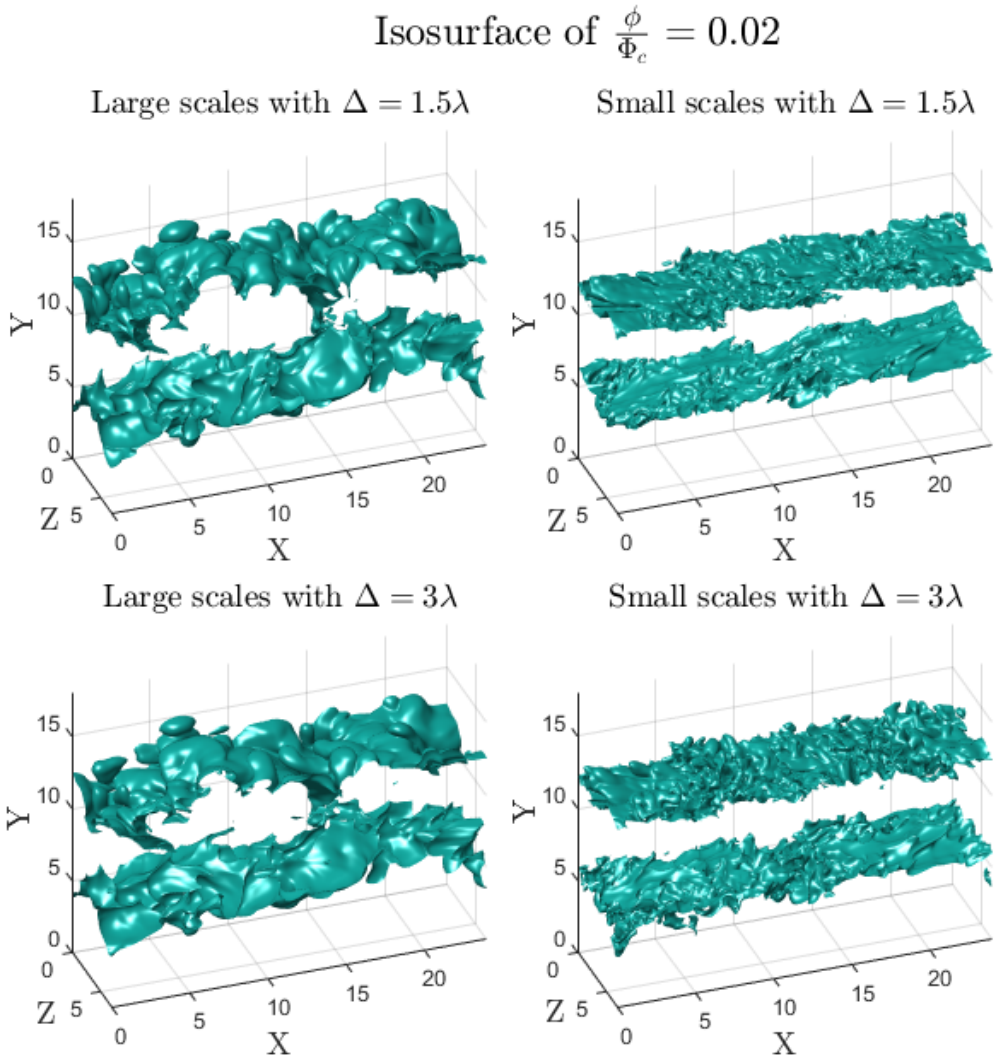

Figure 6.9: Instantaneous scalar interfaces comparison, time unit 100

A higher Schmidt number would have reduced the diffusive process of the scalar leading to more clear results. Anyway, a higher Schmidt number would have required a higher grid resolution (not feasible with the available resources).

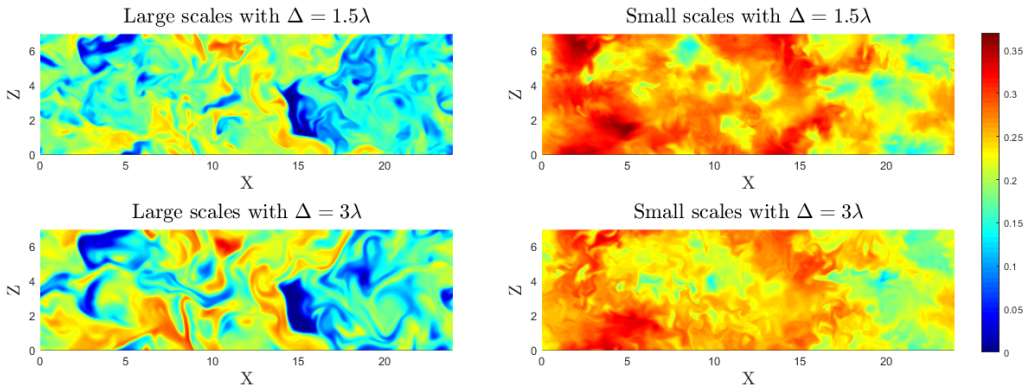

Figure 6.10: Instantaneous scalar contours comparison, x-z midplane, time unit 100

6.2 Self-Similarity

As a first step, the scaling in time of some quantities has been analysed. The trend of the quantities $y^2_{\phi\,1/2}$, $y^2_{\phi\,int}$ and $\frac{1}{\Phi_c^2}$ (known to be linear in the not filtered simulation) in the case of small scales, large scales and not filtered simulations. Since the plots related to the small scales increase much slower if compared with the other cases, two different scales have been used. In Figure 6.11 and 6.12, the trends of $y^2_{\phi\,1/2}$ for both filter lengths are reported.

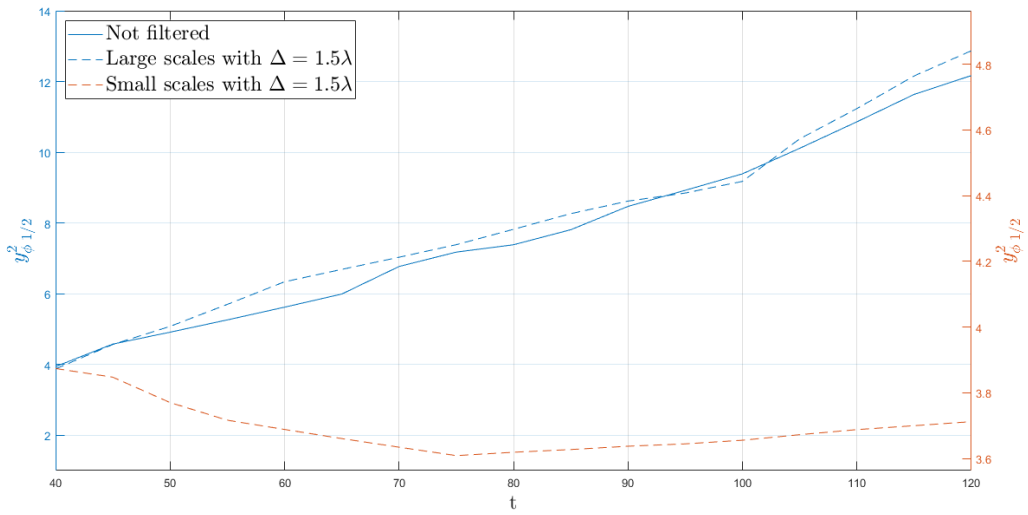

Figure 6.11: Jet scalar half-width comparison, $\Delta = 1.5\lambda_{cl}$

With both the filter lengths, the $y^2_{\phi\,1/2}$ related to the small scales show much smaller variations with respect to the large scales and not filtered cases. The large-scales simulations exhibit a linear behaviour and a growth rate very similar to the one of the not filtered simulation. In the first graph, $y^2_{\phi\,1/2}$ related to the small scales slightly decreases in the first part and start increasing in the last part of the graph. This could simply be interpreted as a "fluctuation", since the statistical convergence is not completely achieved (due to the small domain). Analogously, in the second graph, the growth rate of $y^2_{\phi\,1/2}$ related to the small scales seem to initially grow faster than in the rest of the graph. Again, it is difficult to interpret this fact because it

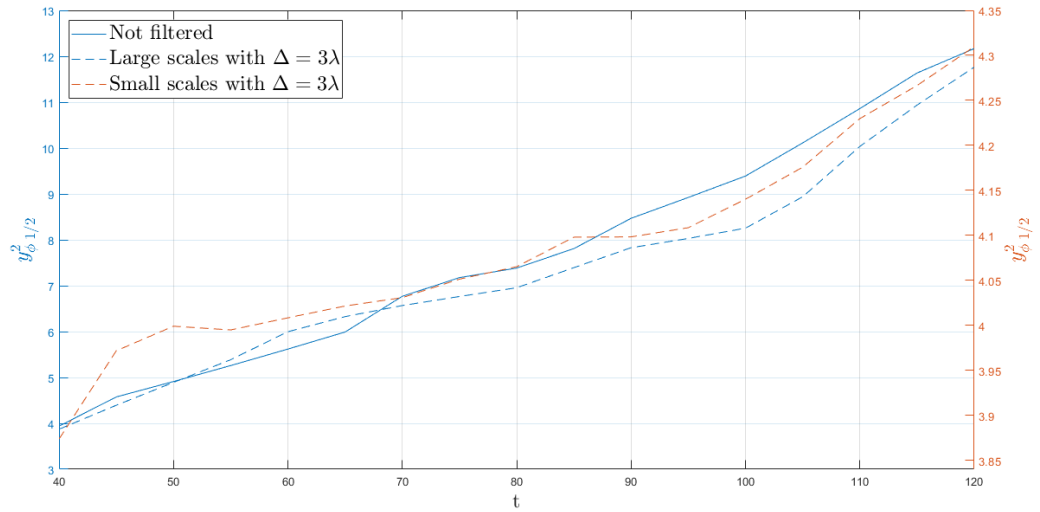

Figure 6.12: Jet scalar half-width comparison, $\Delta = 3\lambda_{cl}$

could be a simple "fluctuation".

In Figure 6.13 and 6.14, the trends of $y^2_{\phi\,int}$ are reported.

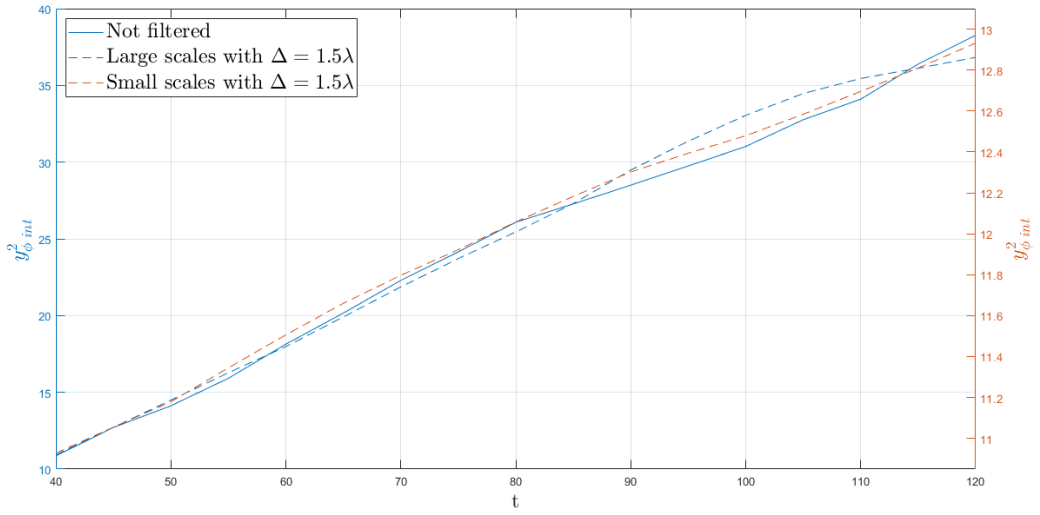

Figure 6.13: Mean scalar interface comparison, $\Delta = 1.5\lambda_{cl}$

In both graphs, the $y^2_{\phi\,int}$ related to small scales grow much slower with respect to the large scales and the not filtered cases. This time, the linear trend is more marked with respect to the $y^2_{\phi\,1/2}$ graphs.

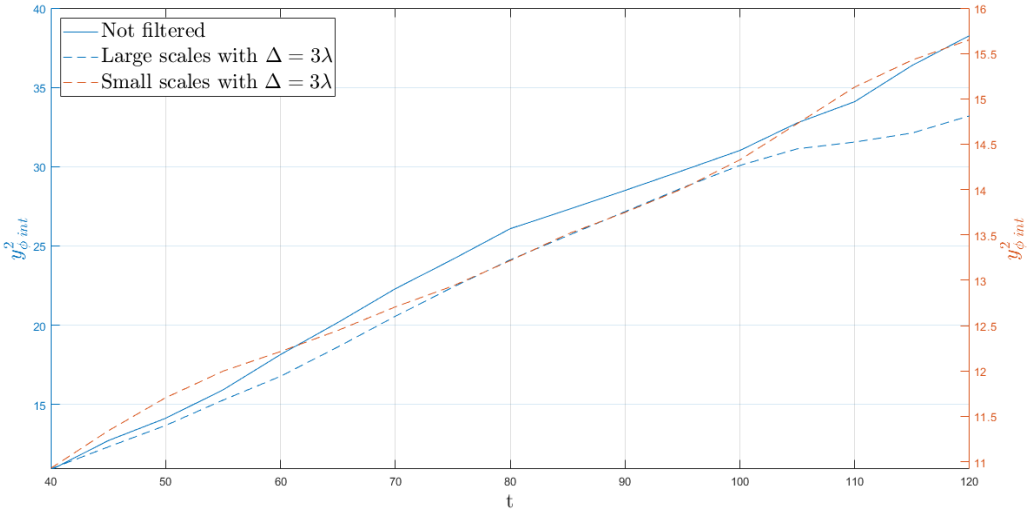

Figure 6.14: Mean scalar interface comparison, $\Delta = 3\lambda_{cl}$

Another parameter that scales linearly with time in a not filtered simulation is $\frac{1}{\Phi_c^2}$ (Figure 6.15 and 6.16). In the case with $\Delta = 1.5\lambda_{cl}$, an initial decrease (and so, an initial increase of Φ_c) can be observed. Again, this behaviour could be simply due to the missed achievement of the statistical convergence. This "fluctuation" could have caused also the initial decrease in $y^2_{\phi\ 1/2}$ (Figure 6.11). In the second part of the graph, $\frac{1}{\Phi_c^2}$ related to the small scales shows a trend that grows slower than a linear one. Probably this is due to the fact that, without the presence of engulfment, the transport of "uncontaminated" fluid toward the core of the jet is not efficient as in the large-scales case (Section 6.3). This last observation, together with the behaviour of $y^2_{\phi\ 1/2}$ in the small-scales case with $\Delta = 1.5\lambda_{cl}$ might indicate that the small scales do not contribute to the self-similarity.

At the same time, the marked linearity in the graphs of $y^2_{\phi\ int}$ in the small-scales case could indicate that the diffusion related to the small scales is more efficient on the interface than in the core of the jet. These aspects will be investigated in more details in Section 6.3.

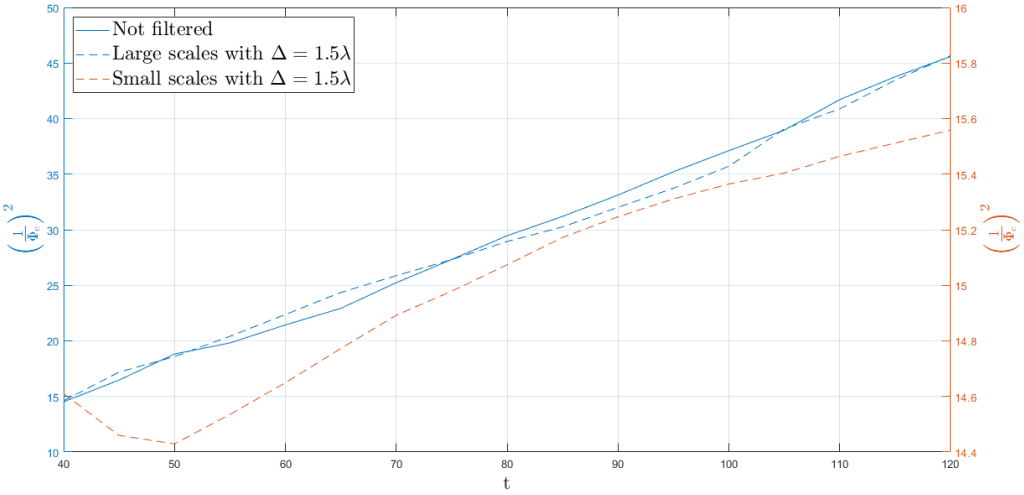

Figure 6.15: Mean scalar value at the centreline comparison, $\Delta = 1.5\lambda_{cl}$

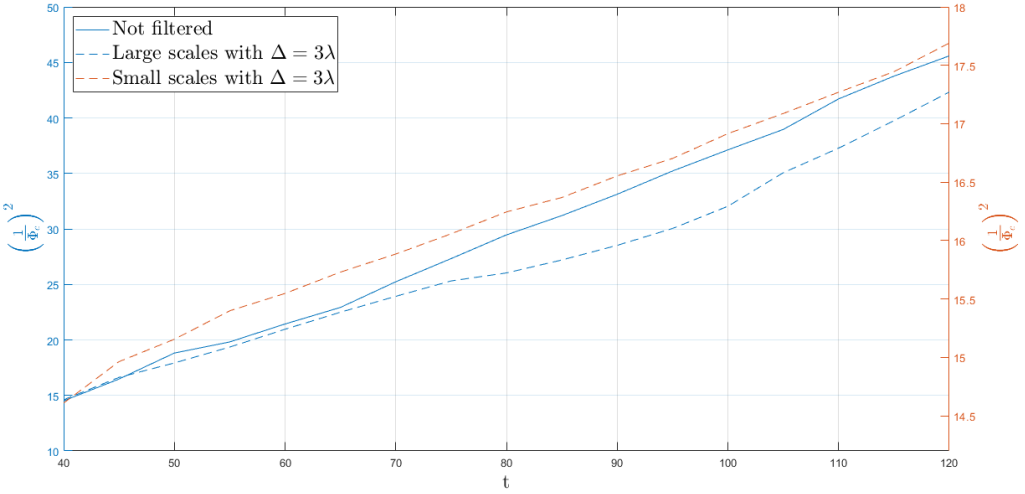

Figure 6.16: Mean scalar value at the centreline comparison, $\Delta = 3\lambda_{cl}$

Finally, the scaled profiles of $\Phi(y)$ and of $\langle\phi'\phi'\rangle(y)$ are reported in Figure 6.17 and 6.18.

All the profiles are smoother in the small-scales cases with respect to the large scales cases because small scales are less correlated with respect to the large ones and the number of samples on which the averaging has been performed is the same ($N_x \times N_z = 412 \times 128 = 52736$).

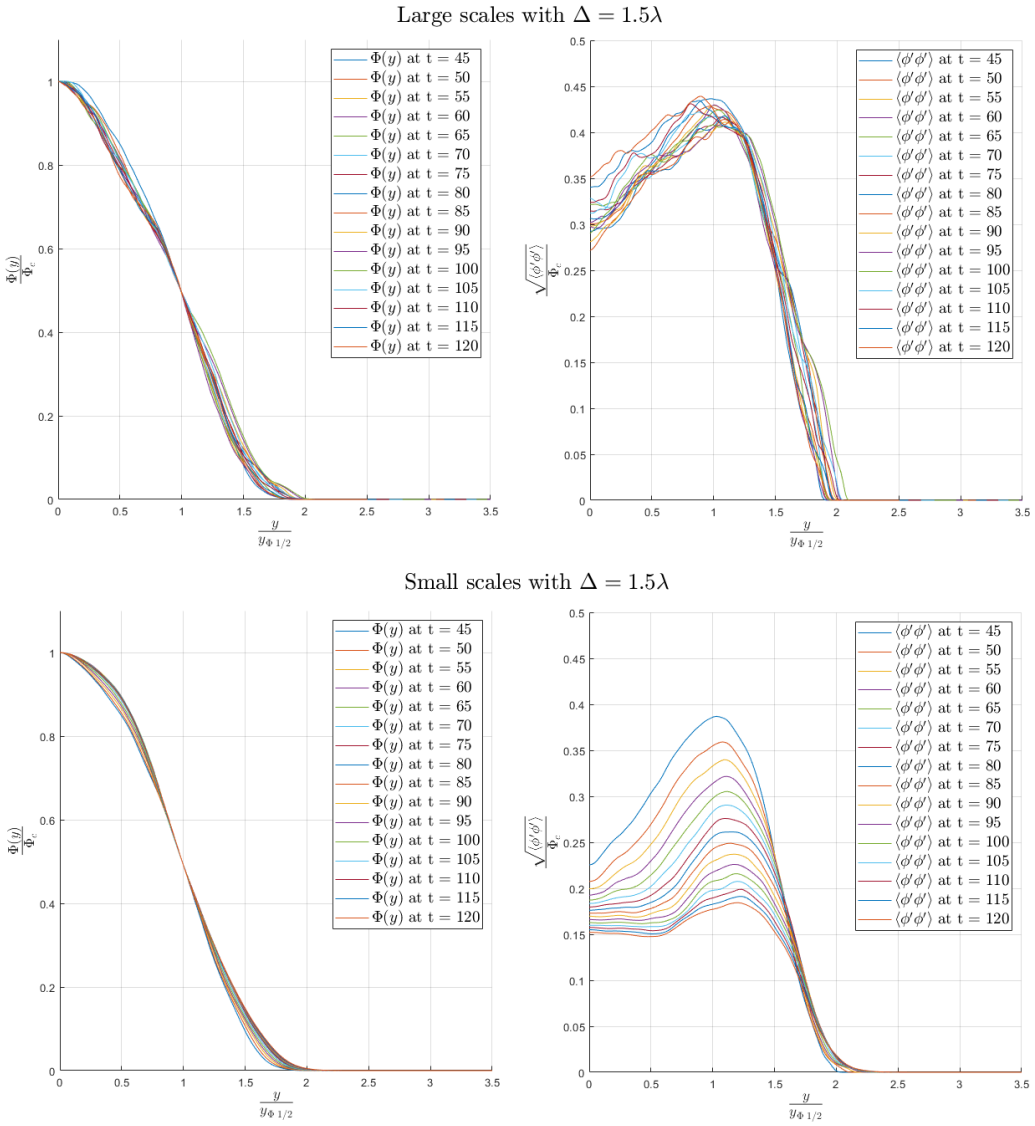

Figure 6.17: Self-similar profiles with $\Delta = 1.5\lambda_{cl}$: large scales (top); small scales (bottom)

Despite this, it can be immediately noticed that the self-similarity scaling in the large-scales case is very similar to the one of the not filtered simulations (Section 5.3).

Looking to the profiles of $\Phi(y)$ in the small-scales graphs, it can be noticed that the inner part of the profiles collapse better in the case with $\Delta = 3\lambda_{cl}$

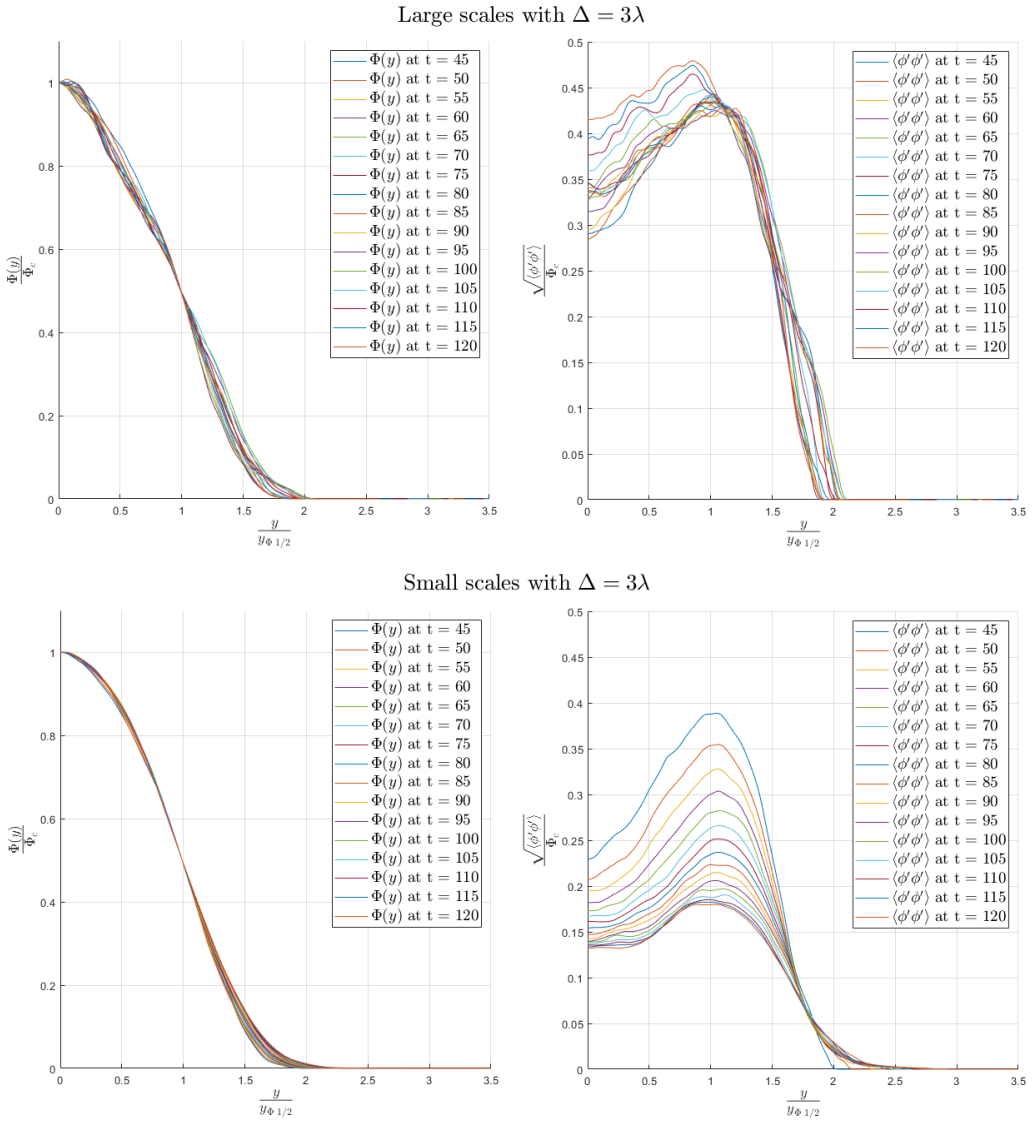

Figure 6.18: Self-similar profiles with $\Delta = 3\lambda_{cl}$: large scales (top); small scales (bottom)

with respect to the case with $\Delta = 1.5\lambda_{cl}$. This could indicate that the scales between these two lengths have an important role in the internal mixing of the passive scalar. On the other hand, the zone in the proximity of the interface is very similar with the two filter lengths (and does not respect the self-similarity). This similarity could be due to the fact that the scales at

which nibbling happens are smaller than both the two filter lengths chosen (as desired). The profiles of $\Phi(y)$ of the small scales presents an interfacial zone that gets less and less sharp as time goes on. This curvature softening in the interfacial zone could be interpreted as an analogous local increase in viscosity due to the effect of the small scales.

In the graphs concerning $\langle \phi' \phi' \rangle (y)$, it can be noticed that in the small-scales cases, the profiles definitely do not collapse on a single curve. Other scalings have been tried to better understand the physics behind this behaviour (using Φ_c and $y_{\phi\,1/2}$ of the not filtered simulations or also normalizing the profile with respect to the centre value), but none of them showed a self-similar behaviour. Moving on to the large-scales cases, a difference in the $\langle \phi' \phi' \rangle (y)$ profiles can be noticed. While in the case $\Delta = 1.5\lambda_{cl}$ the graphs approximatively collapse on the same curve, in the case $\Delta = 3\lambda_{cl}$ it can be noticed that the curves corresponding to $t \geq 105$ do not collapse well in the central part. This fact confirms the important role played in the internal mixing by the scales comprehended between the two filter lengths.

The dynamics of $\langle \phi' \phi' \rangle (y)$ will be further investigated in Section 6.3.

Concluding, the large scales cause an increment in $y^2_{\phi\,1/2}$, $y^2_{\phi\,int}$ and $\frac{1}{\Phi_c^2}$ very similar to the one observed in the not filtered simulation, while the small scales do not cause a significant growth in those parameters. Nevertheless, small scales play an important role in internal mixing. In the large-scales cases, the scalar profiles exhibit a self-similar behaviour almost equal to the one observed in the not filtered simulation (contrary to the small-scales cases).

6.3 Budgets

In order to further investigate the different roles played by large and small scales, the budgets of the variance of the scalar $\langle \phi' \phi' \rangle (y)$ have been studied.

The scalar variance budget equation is presented below (Equation 6.7):

$$\frac{\bar{D}\langle \phi'^2 \rangle}{\bar{D}t} + \nabla \cdot T_\phi = P_\phi - \varepsilon_\phi \tag{6.7}$$

Where P_ϕ is the scalar variance production defined as:

$$P_\phi = -2\langle \mathbf{u}' \phi' \cdot \nabla \langle \phi \rangle \rangle \tag{6.8}$$

ε_ϕ is the scalar dissipation defined as:

$$\varepsilon_\phi = \frac{2}{ReSc} \langle \nabla \phi' \cdot \nabla \phi' \rangle \tag{6.9}$$

and T_ϕ is the flux:

$$T_\phi = \langle \mathbf{u}' \phi'^2 \rangle - \frac{1}{ReSc} \nabla \langle \phi'^2 \rangle \tag{6.10}$$

Where the first term is the turbulent flux and the second term is the diffusive flux.

All the budgets analysed in the present chapter are referred to time unit 100. By choosing this time unit, the scalar had enough time to develop (from time unit 40) but it is still quite far from the time unit at which confinement effects are felt (time unit 120). As a first step the budgets of each simulation are presented separately, reporting the scalar variance production, the scalar variance dissipation and the scalar variance diffusive and turbulent fluxes. The fluxes are reported instead of the transport terms because they present a smoother trend (since the transport terms are obtained through derivative operations performed on the fluxes). Since the flow studied is not homogeneous in time, the sum of the listed contributes (with the corresponding sign) is not necessarily null, but is equal to the derivative of $\langle \phi' \phi' \rangle (y)$ in time.

By plotting the complete budgets, it is clear where the scalar variance is produced, transported and dissipated, but it is difficult to appreciate the

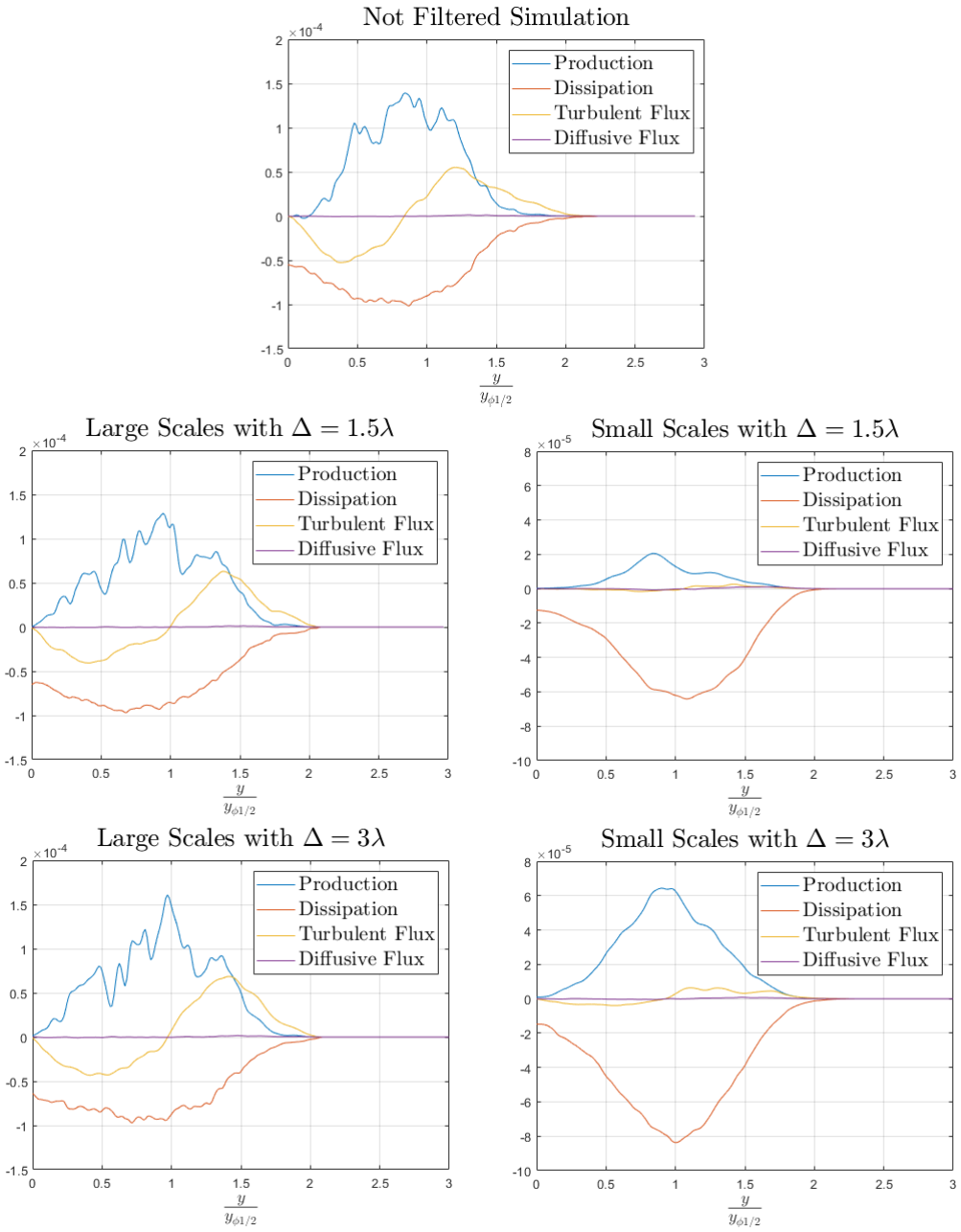

Figure 6.19: Scalar variance budgets, time unit 100

difference between the simulations. For this reason, each term has been subsequently plotted separately and compared through different simulations.

The complete budgets are reported in Figure 6.19.

It can be immediately noticed that the budgets of the large-scales simulations are very similar to the not filtered one. The budgets of small-scales simulations appear qualitatively different from the not filtered one.

In the large-scales simulations and in the not filtered one, it can be noticed that the scalar variance is mostly produced around the scalar half-width of the jet and then transported toward the interface and toward the centreline. A significant amount of scalar variance is dissipated around the centreline. The only appreciable difference between large scales and not filtered simulations is the shape of the turbulent flux near the interface that appear more gradual in the not filtered simulation (probably due to the missed statistical convergence, because in another not filtered simulation performed, this behaviour is not present).

The small-scales simulations present a negligible flux with respect to the other contributes (and with respect to large-scales ones). For this reason, scalar variance is produced and dissipated approximatively in the same regions, mostly near the scalar half-width of the jet. In the small-scales case with $\Delta = 1.5\lambda_{cl}$, the balance between production and dissipation is not satisfied. This is probably due to the fact than the small scales are still acting to even out the initial scalar variance present in the initial condition. So, even if a small amount of production is present, the total scalar variance is decaying in time under the evening out effect of the small scales. The magnitude of the dissipation in the small-scales case is very similar to the one in the large-scales and not filtered cases. Dissipation in the small-scales simulations is very similar between the cases with $\Delta = 1.5\lambda_{cl}$ and $\Delta = 3\lambda_{cl}$, this means that dissipation happens at scales smaller than both the two filter lengths (as expected). On the other hand, the amount of production is very different between the two small-scales cases, meaning that some scalar variance is produced by the scales comprehended between the two filter lengths. Anyway, in both cases the production magnitude is significantly smaller than in the large-scales and not filtered cases.

Hereafter, the term by term comparisons between the different simula-

tions are analysed.

The first term studied is the scalar variance production (Figure 6.20).

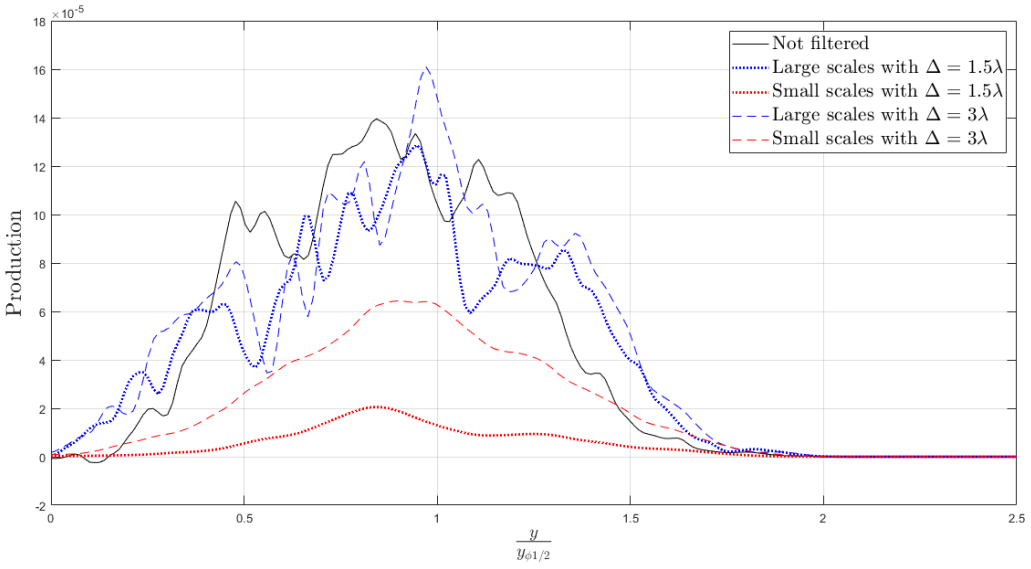

Figure 6.20: Scalar variance production comparison, time unit 100

As in all the previous results, the curves referred to the large scales appear less smooth than the small scales ones. The reason for this is explained in the previous section (Section 6.2).

The amount of scalar variance production generated by the small scales is lower if compared with all the other simulations. Large-scales simulations are again very similar to the not filtered one.

In Figure 6.21, the scalar variance dissipation of the different simulations is shown.

Again, the large-scales simulations are very similar to the not filtered one. The dissipation curves collapse on a single curve when the normalized y coordinate takes values higher than 1.5. The not filtered simulation does not collapse as well as the others because the initial condition of the filtered simulations has been obtained from another not filtered simulation stopped at time unit 40. The main differences can be noticed in the internal part, mainly due to the fact that, in the small-scales simulations, the flux is negligible,

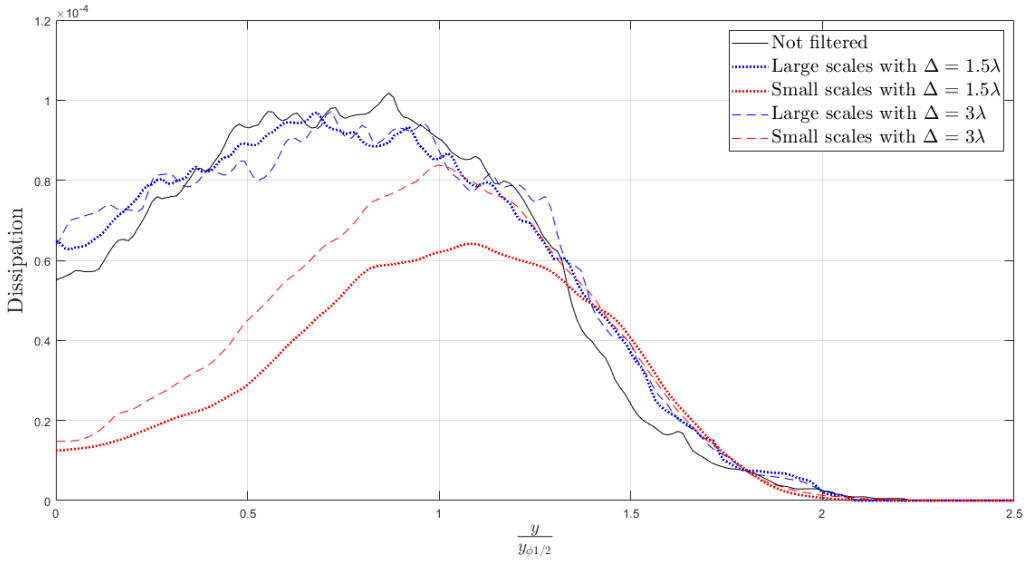

Figure 6.21: Scalar variance dissipation comparison, time unit 100

and dissipation happens in the same regions where production happens.

Flux terms are reported below, starting with the scalar variance diffusive flux (Figure 6.22).

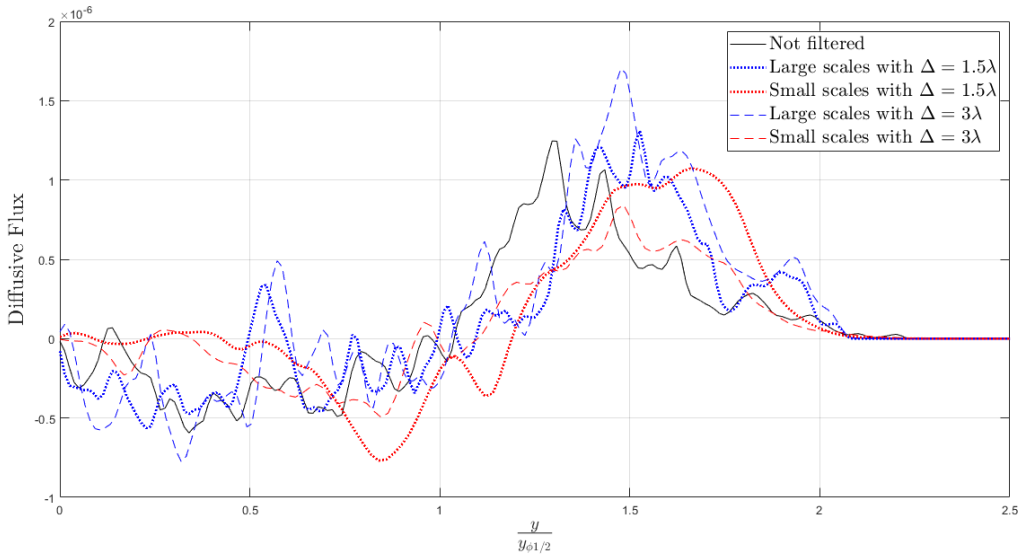

Figure 6.22: Scalar variance diffusive flux comparison, time unit 100

This first graph (Figure 6.22) is difficult to interpret because of its rough

trend. Anyway, two considerations could be made. The first consideration regards the central part. In this region, the small scales seem to present a lower diffusive flux with respect to the other simulations. This may be due to the more uniform look of the scalar in the small-scales cases with respect to the other cases, in this region (this can be observed in the scalar contours in Section 6.1). This uniformity obviously makes the diffusive process less effective. The second observation regards the interface region. The diffusive flux appears to be sharper in the large-scales case in this region (with respect to the small-scales cases). This could be due to the fact that the large scales move the local scalar interface toward regions with a null scalar value, keeping a sharp profile. In the small scales this contribute is not present and the diffusive process have time to smoothens the profile in the interface region.

Similarly, in the profiles of $\langle \phi' \phi' \rangle (y)$ in Figure 6.17 and 6.18, it can be noticed that the large-scales simulations present a much sharper interface with respect to the small-scales ones.

In Figure 6.23 the interface region is shown in more details.

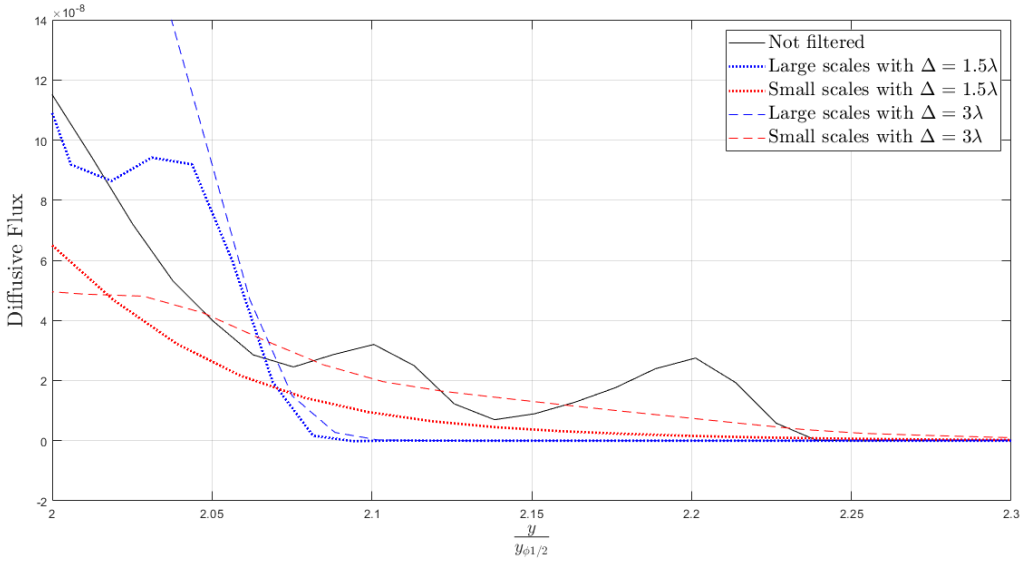

Figure 6.23: Scalar variance diffusive flux comparison, interface region, time unit 100

In Figure 6.24, the scalar variance turbulent flux is reported. The turbulent transport associated to the small scales is negligible with respect to the one associated to the large scales. The difference between large-scales and not filtered simulation is small and is probably due to the missed statistical convergence, as mentioned above (since, in the other not filtered simulation performed, this behaviour is not present). In order to better visualize the interfacial zone, a zoomed version of this graph is shown in Figure 6.25.

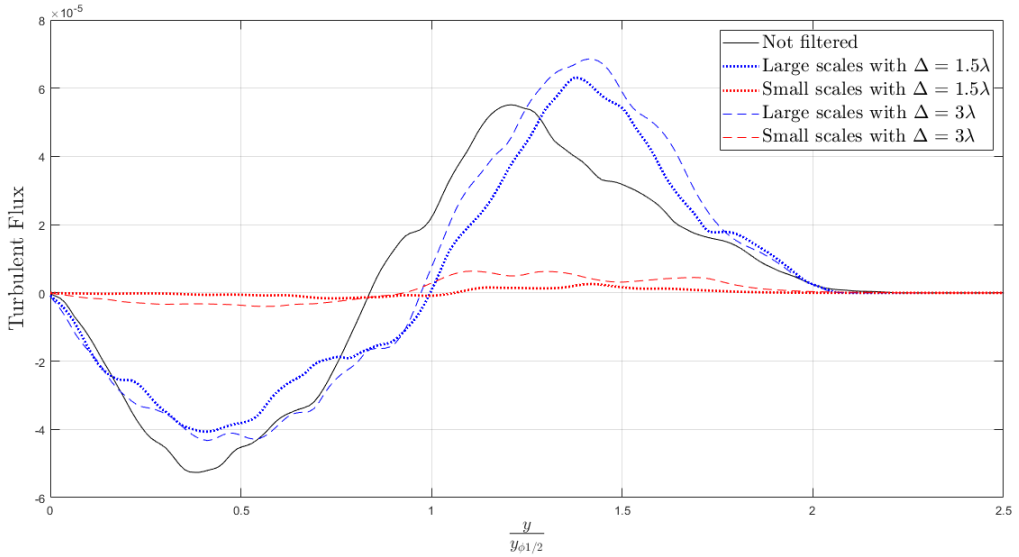

Figure 6.24: Scalar variance turbulent flux comparison, time unit 100

Again, the large-scales simulations present a much sharper behaviour with respect to the small-scales ones.

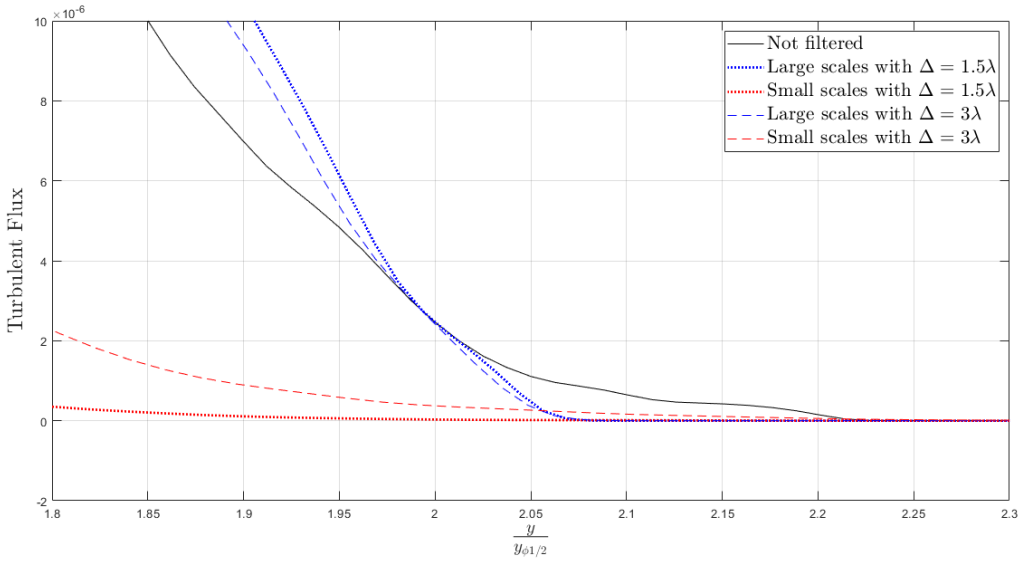

Figure 6.25: Scalar variance turbulent flux comparison, interface region, time unit 100

6.4 Probability Density Function

In this section, the Probability Density Function (PDF) of ϕ' is studied. Two different locations have been investigated: the jet centreline and the mean scalar interface position. Since the mean scalar fields are different in each simulation, all the profiles have been normalized. The PDFs of ϕ'/Φ_c have been plotted in the centreline's graphs while $\phi'/\Phi\left(y_{\phi\, int}\right)$ has been used in those regarding the scalar interface.

In Figure 6.26, the PDF curves computed at the centreline of the different simulations are compared.

It can be immediately noticed that the small-scales simulations present a narrower PDF curve with respect to the other simulations. This result was expected, since the scalar field in these simulations is quite uniform.

Another observation that can be made is that the small-scales PDFs are more symmetric with respect to the other cases. This symmetry could be due to the lack of engulfment. The absence of the latter implies that the convection of "uncontaminated" fluid zones (with low values of ϕ) toward

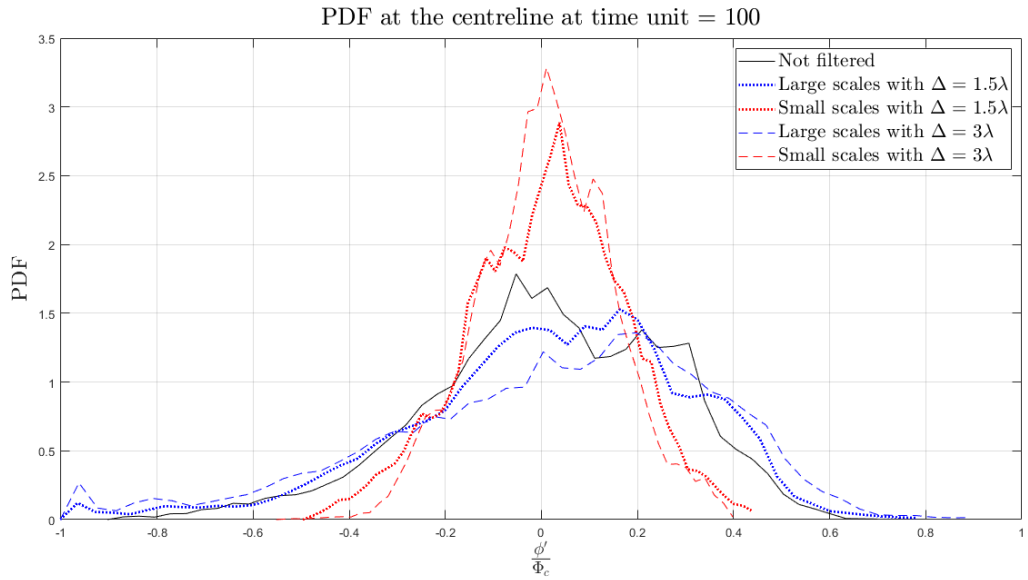

Figure 6.26: PDF curves of the scalar fluctuations computed at the jet centreline, time unit 100

the centreline is absent. This contribute would have increased the extension of the left "tail" of the PDF curve. In fact, it can be noticed that in the large-scales simulations and the not filtered one, the PDFs extend more on the left part of the graph than on the right part. In this respect, it can be noticed that the large-scales simulations' PDF extend up to $\phi'/\Phi_c = -1$ (corresponding to $\phi = 0$), that indicates the presence of unmixed zones, visible also in Figure 6.10.

Finally, the PDF curves have been compared in the mean scalar interface position (Figure 6.27).

All the curves have been normalized with the local mean scalar value and have been reported in a semilogarithmic plot in order to facilitate the visualization. Due to the presence of many zones with a scalar value near zero, the PDF present a maximum around $\phi' = -\Phi\left(y_{\phi\ int}\right)$. The large-scales simulations present a trend very similar to the not filtered one.

Again, the PDFs of the small-scales simulations extend over a relatively narrow range of values because of the evening out function of the small scales.

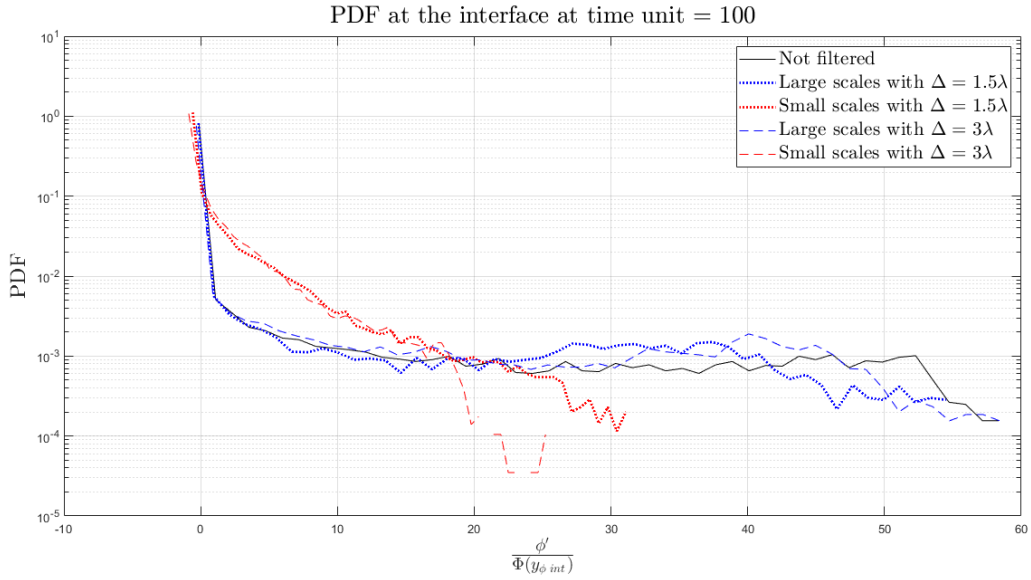

Figure 6.27: PDF curves of the scalar fluctuations computed on the mean scalar interface, time unit 100

At the same time, the right part of the graphs in the small-scales cases present a steeper descent with respect to the other cases, where the PDFs settle to an almost constant value. This plateau could be caused by the large engulfing structures that intersect the mean scalar interface plane. These structures contain a wide range of scalar values.

6.5 Two-Point Statistics

In the following section, the two-point correlation functions of the scalar $R_{\phi'\phi'}$ and the spectra $E_{\phi'\phi'}$ are presented. All the statistics are referred to time unit 100 and are computed on the mean scalar interface location.

The two-point correlation functions $R_{\phi'\phi'}(r_x)$ and $R_{\phi'\phi'}(r_z)$ are reported in Figure 6.28 and 6.29.

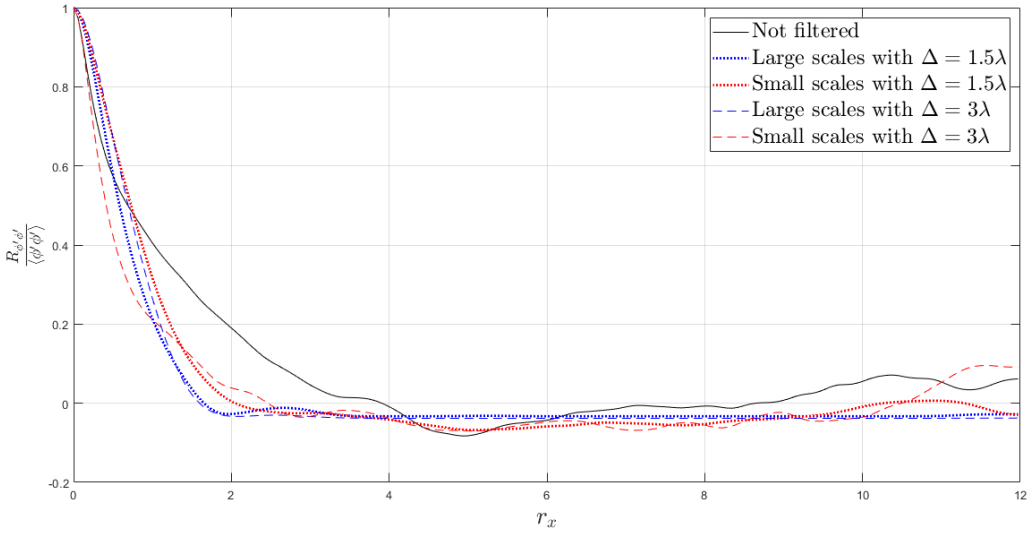

Figure 6.28: Two-point correlations of the scalar fluctuations in the streamwise direction, mean scalar interface region, time unit 100

The first graph (6.28) is difficult to interpret because of its uneven behaviour. All the curves tend to become uncorrelated after a certain r_x distance. Unfortunately, no more information can be extrapolated from this graph. On the other hand, the graph of $R_{\phi'\phi'}(r_z)$ present a clearer scenario. In fact, it can be noticed that, while the two curves relative to $\Delta = 1.5\lambda_{cl}$ are quite similar, the two regarding $\Delta = 3\lambda_{cl}$ are more separated. In particular, the small-scales curve reaches the value of zero and is steeper in the first part of the graph. The large-scales one does not reach a full decorrelation and decrease more gradually in the first part of the graph. This incomplete decorrelation is probably due to the fact that the spanwise structures present

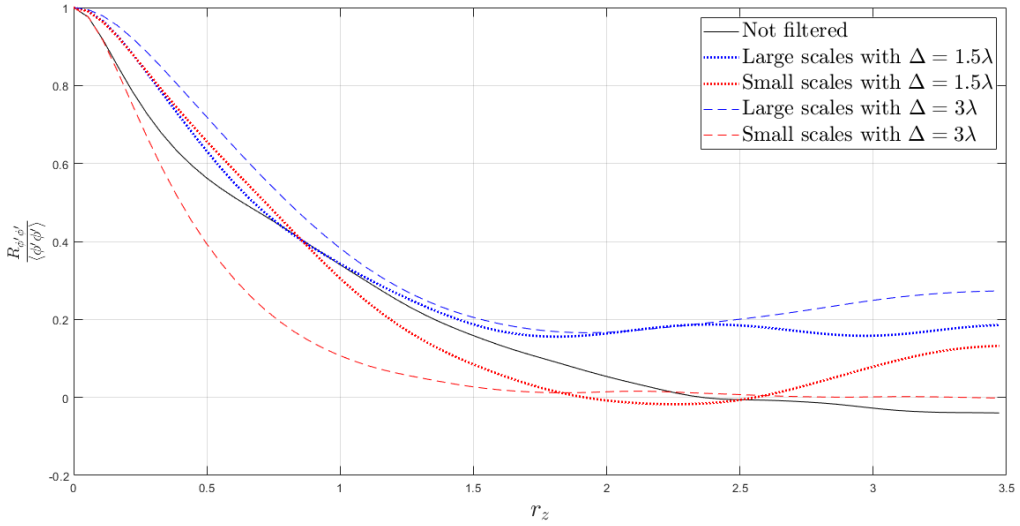

Figure 6.29: Two-point correlations of the scalar fluctuations in the spanwise direction, mean scalar interface region, time unit 100

at the interface are almost as large as the z dimension of the domain.

In Figure 6.30 and 6.31, the spectra of the scalar fluctuations are reported (computed at time unit 100 and in the mean scalar interface position).

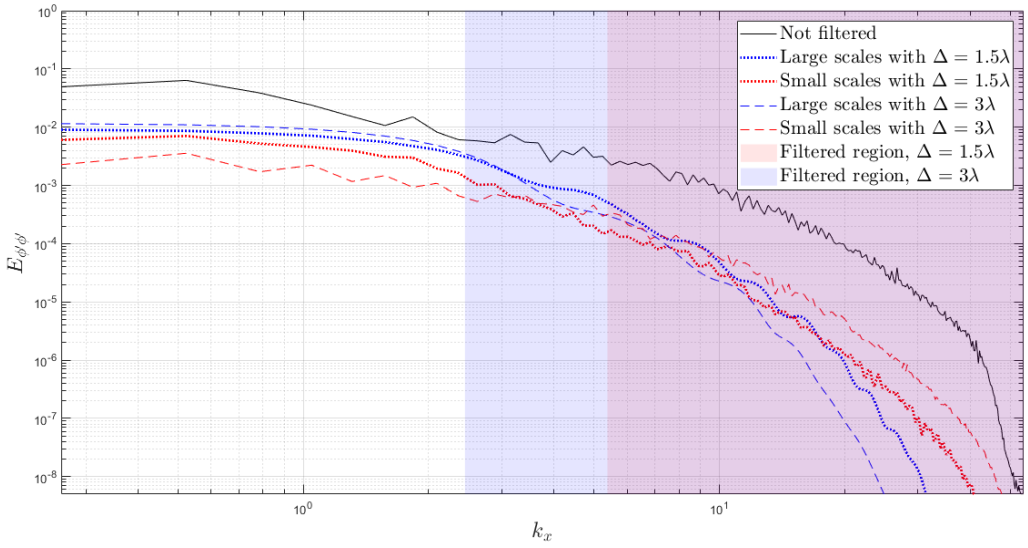

Figure 6.30: Scalar fluctuations spectra in k_x, mean scalar interface region, time unit 100

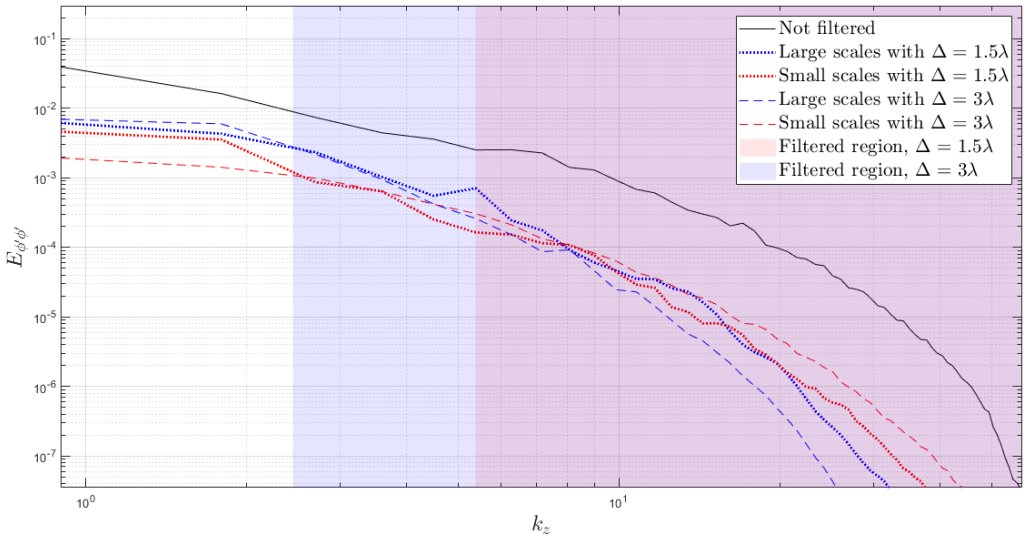

Figure 6.31: Scalar fluctuations spectra in k_z, mean scalar interface region, time unit 100

The filtering lengths corresponding to the considered time unit are reported as a reference. These graphs present a clearer scenario with respect to the graphs of the two-points correlations. Qualitatively speaking, the trends of $E_{\phi'\phi'}(k_x)$ and $E_{\phi'\phi'}(k_z)$ are similar. In both graphs, it can be noticed that the curves regarding $\Delta = 1.5\lambda_{cl}$ present a similar behaviour between small and large scales. In the $\Delta = 3\lambda_{cl}$ case, the difference is more marked. In particular, it can be noticed that, in the initial part of the graph (corresponding to large scales), the large-scales curve presents a higher "energy" content with respect to the small-scales one (as expected). Vice versa, in the right part of the graphs, the curve of the large-scales is below the small-scales one.

Chapter 7

Conclusions

The present thesis work has focused on the study of the entrainment through numerical experiments. In particular, the role of engulfment (caused by large scale motions) and of nibbling (caused by small scales fluctuations in the turbulent sublayer just below the interface) have been studied.

In the first part, the post processing of a DNS of a spatially developing planar jet (previously performed by Doctor Andrea Fregni in collaboration with Professor Andrea Cimarelli) has been carried out. This first step made it possible to study the differences between the spatially evolving jets and the temporal ones.

Subsequently, the study focused on temporal planar jets. This kind of flow has been chosen as subject of the experiments for computational cost reasons. A benchmark DNS has been carried out to validate the settings for the following experiments. After the settings validation, the experiments have been performed. These experiments consisted in the study of the spreading of a passive scalar under the effect of large and small scales separately. These two velocity fields have been obtained implementing a box filter. Different approaches have been tested. The most promising approaches were those with the time activation of the filter at the time unit corresponding to the beginning of the self-similarity regime and the filter lengths varying in time. The two experiments reported in Chapter 6 present respectively filter lengths

of $\Delta = 1.5\lambda_{cl}$ and $\Delta = 3\lambda_{cl}$.

As a first step, the spreading of the jets in the different experiments has been studied through quantities such as $y_{\phi\,1/2}$ and $y_{\phi\,int}$. With both filter lengths, the scalar field spread much more under the action of the large-scale velocity field than under the effect of the small-scale one. A summary table reporting the increase in $y_{\phi\,1/2}$ and in $y_{\phi\,int}$ between time unit 40 and time unit 120 is presented in Table 7.1 (the % values are computed with respect to the not filtered simulation):

Table 7.1: Summary of the results

Simulations	**Increase in $y_{\phi\,1/2}$**	**Increase in $y_{\phi\,int}$**	**% Increase in $y_{\phi\,1/2}$**	**% Increase in $y_{\phi\,int}$**
Not filtered Simulation	1.50 h	2.89 h	-	-
Large Scales with $\Delta = 1.5\lambda_{cl}$	1.62 h	2.76 h	108%	95.5%
Small Scales with $\Delta = 1.5\lambda_{cl}$	-0.04 h	0.29 h	-2.7%	10.0%
Large Scales with $\Delta = 3\lambda_{cl}$	1.46 h	2.46 h	97.3%	85.1%
Small Scales with $\Delta = 3\lambda_{cl}$	0.11 h	0.65 h	7.3%	22.5%

The passive scalar presented a more pronounced self-similar behaviour under the action of large scales than under the action of the small scales.

Subsequently, the scalar variance production, dissipation and turbulent and diffusive fluxes have been studied. The most interesting result obtained in this paragraph is that the turbulent flux associated to the small scales is negligible with respect to the one associated to the large scales.

The PDF profiles associated to the different experiments have been analysed in the centreline and on the mean scalar interface. From these profiles, the importance of the small scales' role in the mixing process emerged.

In conclusion, these experiments support the idea that the engulfment process dominate the entrainment phenomenon. It must be pointed out that small scales largely contribute to the mixing process, evening out the inhomogeneities caused by engulfment. The comprehension of the role of the different scales has repercussions for a lot of applications, first among all, for turbulence modelling.

Clearly, since an initially irrotational fluid particle can acquire vorticity only through a viscous process [4], every particle belonging to the core of the jet (initially outside of it) would have passed through a viscous layer, but mainly after being convected toward the core of the jet by large scale engulfing structures.

These experiments can be improved in different ways:

- The implementation of a Gaussian filter that would allow a "continuous" variation of the filter length in time.
- The increase of the domain size in the homogeneous directions (L_x and L_z) in order to reach the statistical convergence of the results, or alternatively the carrying out of multiple experiments for each filter setting in order to average them together (as different realizations of the same experiment).
- The increase of the crossflow domain size L_y that would allow a longer time for the passive scalar to evolve before the beginning of significant confinement effects.
- The increase in grid resolution to obtain more accurate results.
- The increase of the Schmidt number that would make the passive scalar more similar to an ideal tracer (the resolution should be further increased as a consequence of this point).

Appendix A

Filtering Operation

In this appendix, the experiments that led to the choice of the filter lengths and of the filter starting time are briefly presented. In all the simulations presented, the filter used is a box filter.

In the first filtered simulation performed, the filter lengths have been set to $\Delta_x \approx 0.23$ and $\Delta_z \approx 0.22$. These values have been chosen because (as explained in Chapter 6) the Taylor micro-scale at time unit 40 (when self-similarity begins) is approximatively that length. The activation time of the filter used is time unit 40.

Initially, for the small-scales simulation, the following formula has been considered:

$$\frac{\partial \phi_s}{\partial t} + (u_i - \tilde{u}_i) \frac{\partial \phi_s}{\partial x_i} = D \frac{\partial^2 \phi_s}{\partial x_i \partial x_i} \tag{A.1}$$

As it can be noticed, the mean value of the velocity is not present in the convection term. On the basis of the results of this simulation, it has been decided to add the contribution of U_j in the convection term. In fact, in this simulation, the passive scalar almost remained in its initial position and just diffused under the effect of the small scales passing through and under the effect of the diffusivity D as shown in Figure A.1.

After this first attempt, other four simulations have been run. The same filter lengths have been used, but the mean value of the velocity have been added in the small-scales case (Formula A.2) and two activation times unit

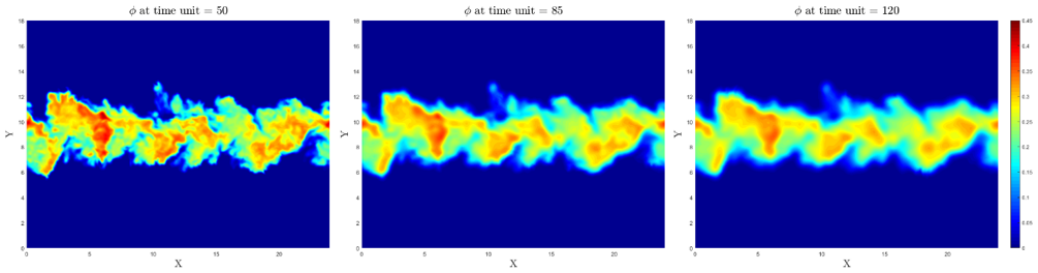

Figure A.1: Scalar contours: small scales without the mean velocity field, filter activated from time unit 40 and $\Delta = 0.23$

have been tested (0 and 40).

$$\frac{\partial \phi_s}{\partial t} + (u_i - \tilde{u}_i + U_i)\frac{\partial \phi_s}{\partial x_i} = D\frac{\partial^2 \phi_s}{\partial x_i \partial x_i} \tag{A.2}$$

The results are shown in Figure A.2 and A.3.

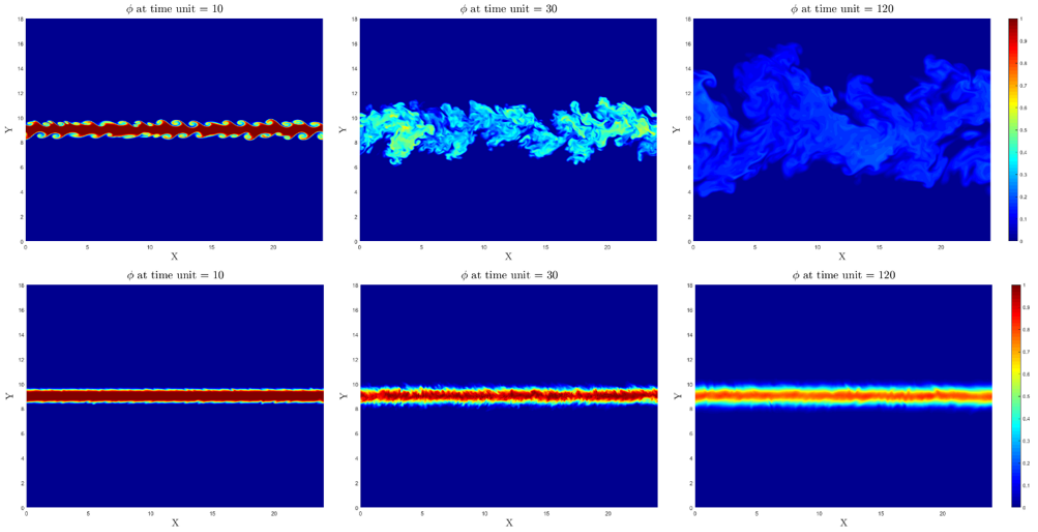

Figure A.2: Scalar contours, filter activated from time unit 0 and $\Delta = 0.23$*,* ϕ_l *(top);* ϕ_s *(bottom)*

In the small-scales case, for $\Delta = 0.23$ and filter activation at time unit 0, the scalar is almost in its initial position. Since the initial Kelvin Helmholtz structures are cancelled out in the small-scales simulation, the scalar remains at the centre of the jet, and, once turbulence has developed, the scalar is not

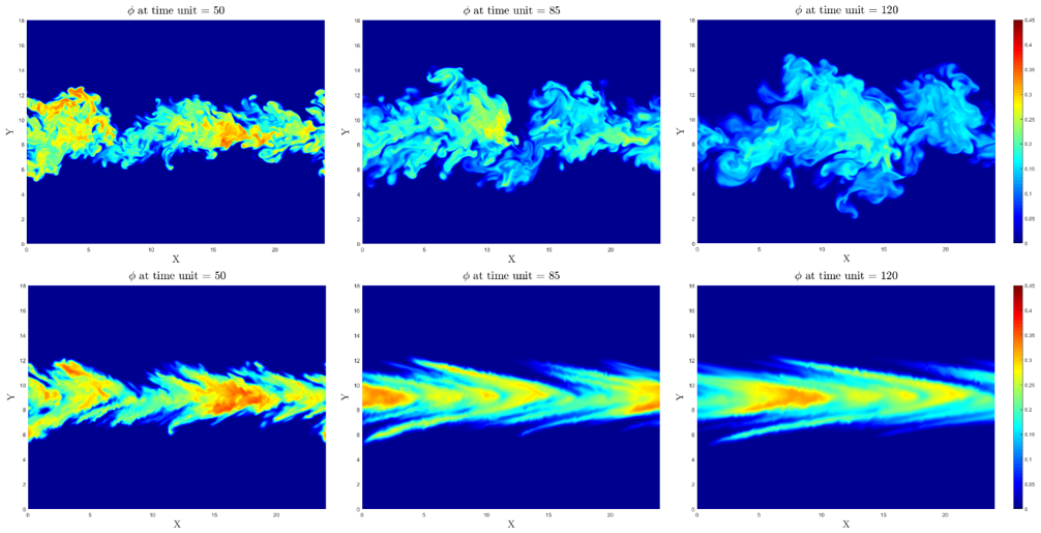

Figure A.3: Scalar contours, filter activated from time unit 40 and $\Delta = 0.23$*,* ϕ_l *(top);* ϕ_s *(bottom)*

matching the vorticity interface, where nibbling happens. This problem has been overcome by activating the filter from time unit 40. In both cases the scalar spread less in the small-scales cases with respect to the large-scales cases. In the small-scales simulation with filter activation at time unit 40, the scalar contours presents an arrow-shaped look. This is due to the presence of some regions of engulfing fluid in the initial condition. These regions continue developing in the large-scales simulations, while, in the small-scales ones initially remain in their positions and gradually diffuse under the small scales action and are stretched by the mean flow.

In order to study the influence of the choice of the filter length on the results, a second experiment has been carried out with $\Delta_x \approx 0.93$ and $\Delta_z \approx 0.88$. This filter length has been chosen also based on the velocity spectra (computed at the mean scalar interface position) reported in Figure 5.14 and 5.15, and has been chosen such that the corresponding wavenumber falls in the inertial subrange. Other two experiments have been carried out with this filter lengths choice (with filter activation at time unit 0 and 40 respectively). The results are shown in Figure A.4 and A.5.

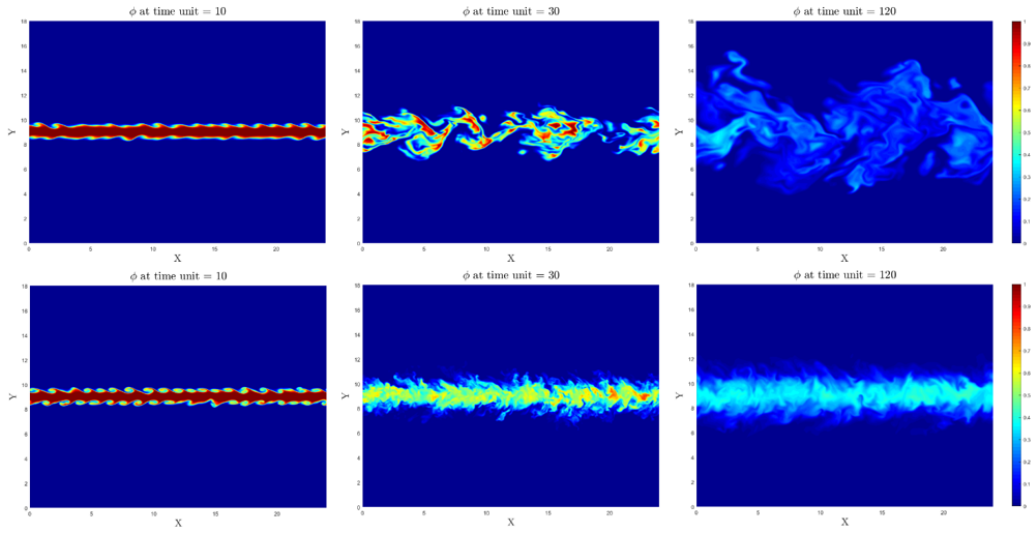

Figure A.4: Scalar contours, filter activated from time unit 0 and $\Delta = 0.93$*,* ϕ_l *(top);* ϕ_s *(bottom)*

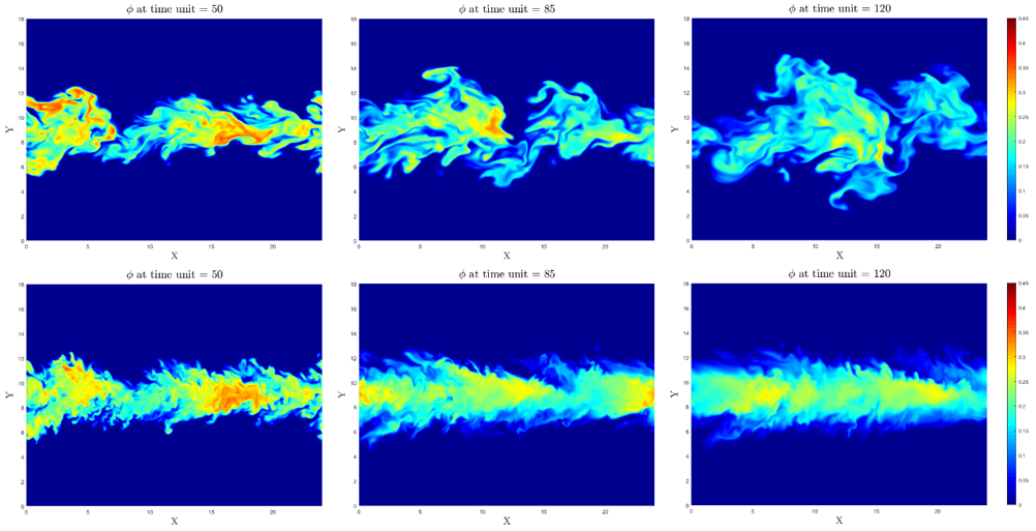

Figure A.5: Scalar contours, filter activated from time unit 40 and $\Delta = 0.93$*,* ϕ_l *(top);* ϕ_s *(bottom)*

In the small-scales case, the scalar is spread in a wider region in the simulation with $\Delta = 0.93$ with respect to the one with $\Delta = 0.23$. However, it must be pointed out that a good portion of this spreading is given by the initial Kelvin-Helmholtz structures that appear to be present in the small-

scales simulation with $\Delta = 0.93$. Obviously, these initial structures are not part of the nibbling mechanism, but they appear in the small-scales simulation only because the filter length (that is reasonable once turbulence is developed) is of the order of the characteristic length scale of the problem in the initial instants. In fact, in this simulation, the jet spreads faster in the first part of the simulation than in the last part. Again, this issue is solved by activating the filter from time unit 40 (once turbulence is developed and there is a marked separation between the lengthscale of the problem and the small scales). Finally, comparisons of the scalar fields of the different experiments corresponding to time unit 100 are presented. In Figure A.6, A.7, A.8 and A.9, the x-y and x-z midplanes relative to filter activation time 0 and 40 are presented respectively.

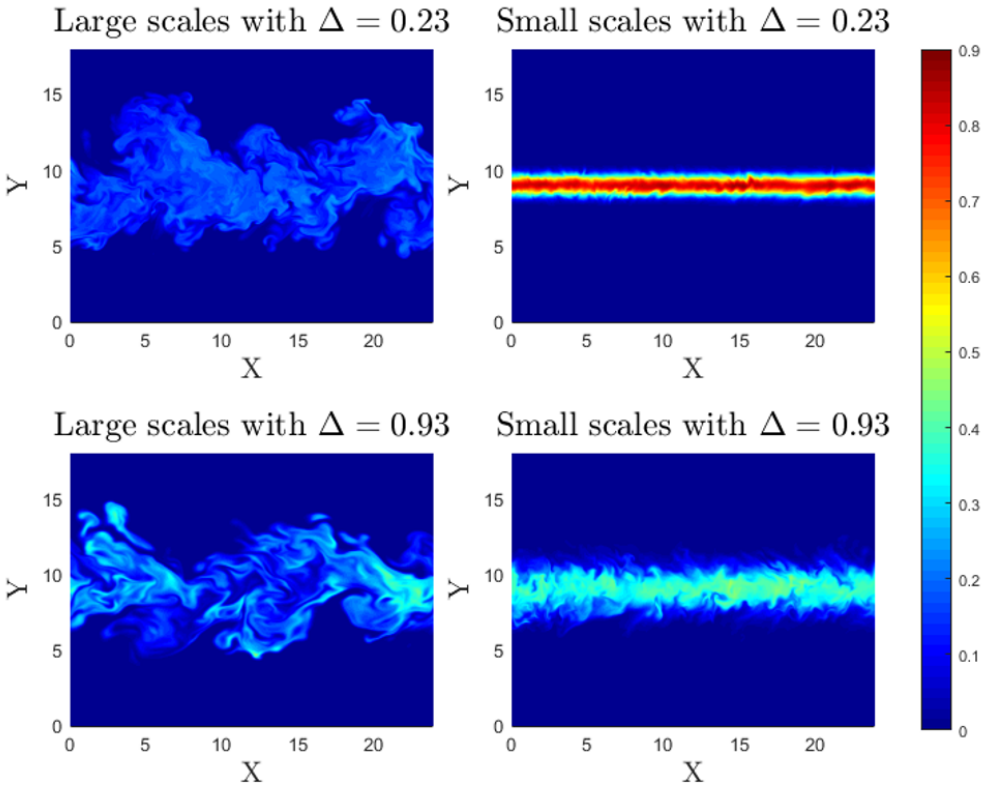

Figure A.6: Scalar contours, filter activated from time unit 0, x-y midplane comparison, time unit 100

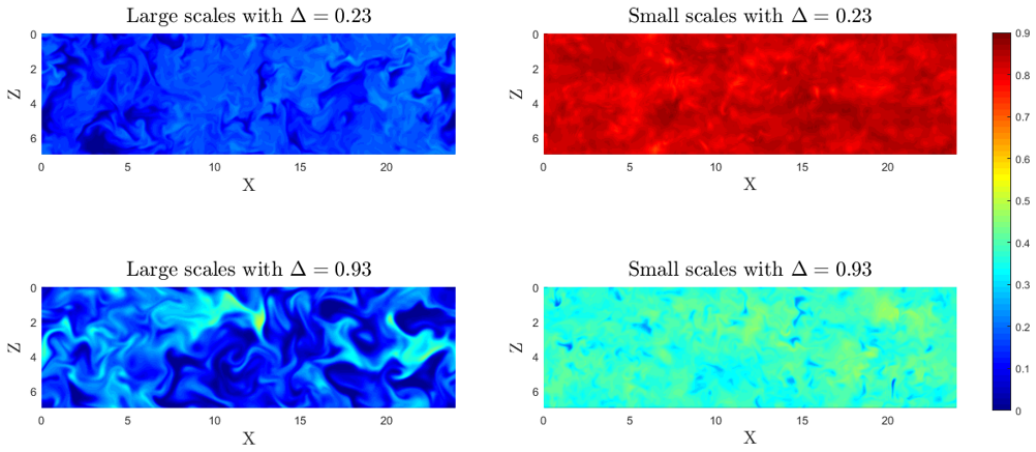

Figure A.7: Scalar contours, filter activated from time unit 0, x-z midplane comparison, time unit 100

Another consideration is that, in both the simulations with $\Delta = 0.23$ and $\Delta = 0.93$, in the small-scales simulations, the scalar is much more evenly distributed than in the large-scales ones. In fact, in the large-scales simulations the scalar field presents some "holes", as shown in Figure A.9. From this, it could be deduced that, while the large scales largely contribute to the spreading of the jet, the small scales predominate the mixing inside the core of the jet, tending to uniform the scalar field and evening out the large inhomogeneity.

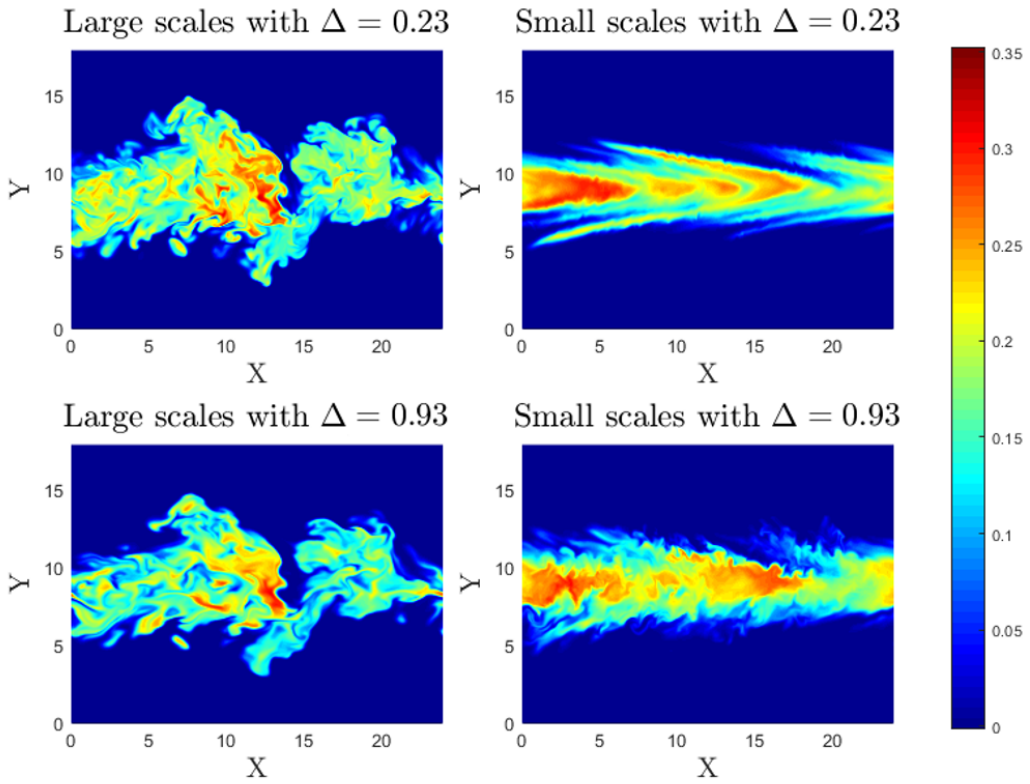

Figure A.8: Scalar contours, filter activated from time unit 40, x-y midplane comparison, time unit 100

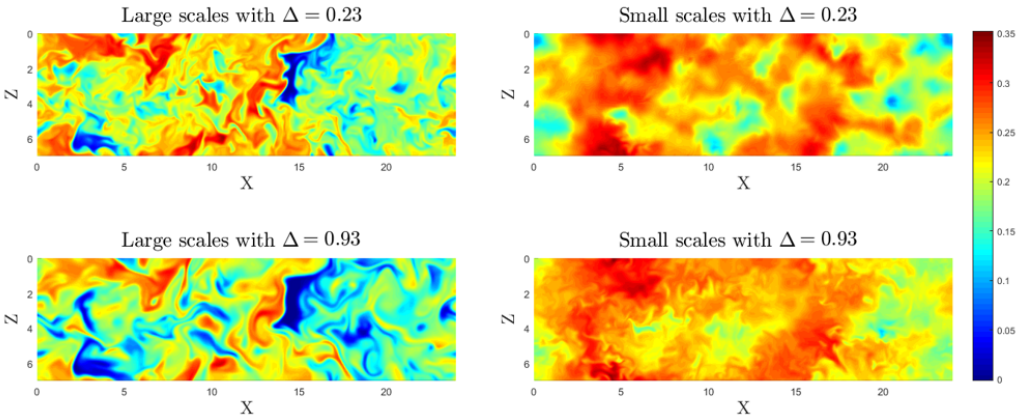

Figure A.9: Scalar contours, filter activated from time unit 40, x-z midplane comparison, time unit 100

Bibliography

[1] da Silva, Carlos B. and Hunt, Julian C.R. and Eames, Ian and Westerweel, Jerry. 2014. *Interfacial Layers Between Regions of Different Turbulence Intensity*. Annual Review of Fluid Mechanics, 46:567-590.

[2] Pope, S. 2000. *Turbulent Flows*. Cambridge: Cambridge University Press. doi:10.1017/CBO9780511840531.

[3] da Silva, Carlos B. and José C. F. Pereira. 2008. *Invariants of the velocity-gradient, rate-of-strain, and rate-of-rotation tensors across the turbulent/nonturbulent interface in jets*. IDMEC/IST Technical University of Lisbon, Pav. Mecânica I, 1° andar/esq./LASEF, Av. Rovisco Pais, 1049-001 Lisboa, Portugal

[4] Batchelor, GK. 1967. *An Introduction to Fluid Mechanics*. Cambridge, UK: Cambridge Univ. Press.

[5] Davidson, PA. 2000. *Turbulence: An Introduction for Scientists and Engineers*. New York: Oxford Univ. Press.

[6] Holzner M, Liberzon A, L¨ uthi B, Nikitin N, Kinzelbach W, Tsinober A. 2008. *A Lagrangian investigation of the small-scale features of turbulent entrainment through particle tracking and direct numerical simulation*. J. Fluid Mech. 598:465-475.

[7] Holzner M, Liberzon A, NikitinN, Kinzelbach W, Tsinober A. 2007. *Small-scale aspects of flows in proximity of the turbulent/nonturbulent interface*. Phys. Fluids 19:071702.

[8] Wolf M, L¨ uthi B, Holzner M, Krug D, Kinzelbach W, Tsinober A. 2012. *Investigations on the local entrainment velocity in a turbulent jet.* Phys. Fluids 24:105110.

[9] Taveira RMR, da Silva CB. 2013a. *Dynamics of scalar variance and dissipation at the TNT interface.* Presented at Eur. Turbul. Conf., 14th, Lyon, France.

[10] Sylvain Laizet. *Incompact3d user guide version 2.0.* Imperial College London). https://www.incompact3d.com/uploads/5/8/7/2/58724623/__user_guide_incompact3d_v2.pdf

[11] Sanjiva K. Lele, 1992. *Compact finite difference schemes with spectral-like resolution.* Journal of Computational Physics, 103, 1, 16-42.

[12] Ning, Li and Sylvain, Layzet, 2010. *2DECOMP&FFT - A Highly Scalable 2D Decomposition Library and FFT Interface* the Numerical Algorithms Group (NAG) and Imperial College London

Acknowledgements

Vorrei dedicare un breve spazio a tutte le persone senza le quali questo lavoro di tesi non sarebbe stato possibile. Primo fra tutti, vorrei ringraziare il Professor Andrea Cimarelli per avermi guidato in questo percorso con immancabile disponibilità e fiducia nei miei confronti. La sua cordialità ha reso questo lavoro, già molto stimolante ed interessante, anche piacevole.

Vorrei ringraziare la Professoressa Elisabetta De Angelis per la disponibilità dimostratami accettando il ruolo di Relatrice di questa tesi e per aver reso possibile questo traguardo.

Un ringraziamento speciale va alla mia famiglia per avermi sempre sostenuto e per avermi garantito la serenità necessaria al completamento di questo percorso universitario.

Infine desidero ringraziare i miei amici che sono stati presenti e che hanno reso l'università, in un certo senso, la mia seconda casa.